Time-Domain Lifetime Measurements

Time-resolved measurements are widely used in fluorescence spectroscopy, particularly for studies of biological macromolecules and increasingly for cellular imaging. Time-resolved measurements contain more information than is available from the steady-state data. For instance, consider a protein that contains two tryptophan residues, each with a distinct lifetime. Because of spectral overlap of the absorption and emission, it is not usually possible to resolve the emission from the two residues from the steady-state data.

However, the time-resolved data may reveal two decay times, which can be used to resolve the emission spectra and relative intensities of the two tryptophan residues. The time-resolved measurements can reveal how each of the tryptophan residues in the protein is affected by the interactions with its substrate or other macromolecules. Is one of the tryptophan residues close to the binding site? Is a tryptophan residue in a distal domain affected by substrate binding to another domain? Such questions can be answered if one measures the decay times associated with each of the tryptophan residues.

There are many other examples where the time-resolved data provide information not available from the steady-state data. One can distinguish static and dynamic quenching using lifetime measurements. Formation of static ground-state complexes do not decrease the decay time of the uncomplexed fluorophores because only the unquenched fluorophores are observed. Dynamic quenching is a rate process acting on the entire excited-state population, and thus decreases the mean decay time of the entire excited-state population. Resonance energy transfer is also best studied using time-resolved measurements. Suppose a protein contains a donor and acceptor, and the steady-state measurements indicate the donor is 50% quenched by the acceptor. The result of 50% donor quenching can be due to 100% quenching for half of the donors, or 50% quenching of all the donors, or some combination of these two limiting possibilities. The steady-state data cannot distinguish between these extreme cases. In contrast, very different donor intensity decays would be observed for each case. If all the donors are 50% quenched by the acceptors, and the acceptors are at a single distance, then the donor decay will be a single exponential with a lifetime of half the unquenched lifetime. If 50% of the donors are completely quenched and 50% are not quenched, then the donor lifetime will be the same as the unquenched lifetime. A multiexponential decay would be observed if the donor is partially quenched by the acceptor and some of the donors do not have a nearby acceptor. The time-resolved donor decays are highly informative about the purity of the sample as well as the donor-to-acceptor distance.

There are many other instances where lifetime measurements are advantageous over steady-state measurements. One important application is cellular imaging using fluorescence microscopy. When labeled cells are observed in a fluorescence microscope, the local concentration of the probe in each part of the cell is not known. Additionally, the probe concentration can change during the measurement due to washout or photobleaching. As a result it is difficult to make quantitative use of the local intensities. In contrast, if the probe emission is well above the background signal, fluorescence lifetimes are typically independent of the probe concentration. Many fluorescence sensors such as the calcium probes display changes in lifetime in response to analytes. Also, resonance energy transfer (RET) reveals the proximity of donors and acceptors by changes in the donor lifetime. Because of advances in technology for time-resolved measurements, it is now possible to create lifetime images, where the image contrast is based on the lifetime in each region of the sample. Fluorescence lifetime imaging microscopy, or FLIM, has now become an accessible and increasingly used tool in cell biology (Chapter 22). An

understanding of FLIM must be based on an understanding of the technology used for time-resolved fluorescence measurements.

Prior to describing the technology for time-resolved measurements we present an overview of the two dominant methods for time-resolved measurements: the time-domain (TD) and frequency-domain (FD) methods. There are also several variations to each approach. Since the previous edition of this book there have been advances in both methods. The time-domain technology has become smaller, less expensive, and more reliable. We will also describe some of the earlier approaches, which clarify why specific procedures have been selected. We also discuss the important topic of data analysis, which is essential for using the extensive data from modern instruments, and avoiding misuse of the results by over-interpretation of the data.

4.1. OVERVIEW OF TIME-DOMAIN AND FREQUENCY-DOMAIN MEASUREMENTS

Two methods of measuring time-resolved fluorescence are in widespread use: the time-domain and frequency-domain methods. In time-domain or pulse fluorometry, the sample is excited with a pulse of light (Figure 4.1). The width of the pulse is made as short as possible, and is preferably much shorter than the decay time τ of the sample. The time-dependent intensity is measured following the excitation pulse, and the decay time τ is calculated from the slope of a plot of log $I(t)$ versus t, or from the time at which the intensity decreases to $1/e$ of the intensity at $t = 0$. The intensity decays are often measured through a polarizer oriented at 54.7° from the vertical z-axis. This condition is used to avoid the effects of rotational diffusion and/or anisotropy on the intensity decay (Chapter 11).

The alternative method of measuring the decay time is the frequency-domain or phase-modulation method. In this case the sample is excited with intensity-modulated light, typically sine-wave modulation (Figure 4.2). The amplitude-modulated excitation should not be confused with the electrical component of an electromagnetic wave. The intensity of the incident light is varied at a high frequency typically near 100 MHz, so its reciprocal frequency is comparable to the reciprocal of decay time τ. When a fluorescent sample is excited in this manner the emission is forced to respond at the same modulation frequency. The lifetime of the fluorophore causes the emission to be delayed in time relative to the excitation, shown as the shift to the right in Figure 4.2. This delay is measured as a phase shift (ϕ), which can be used to calculate the decay time. Magic-angle polarizer conditions are also used in frequency-domain measurements.

The lifetime of the fluorophore also causes a decrease in the peak-to-peak height of the emission relative to that of the modulated excitation. The modulation decreases because some of the fluorophores excited at the peak of the excitation continue to emit when the excitation is at a minimum. The extent to which this occurs depends on the decay time and light modulation frequency. This effect is called demodulation, and can also be used to calculate the decay time. FD measurements typically use both the phase and modulation information. At present, both

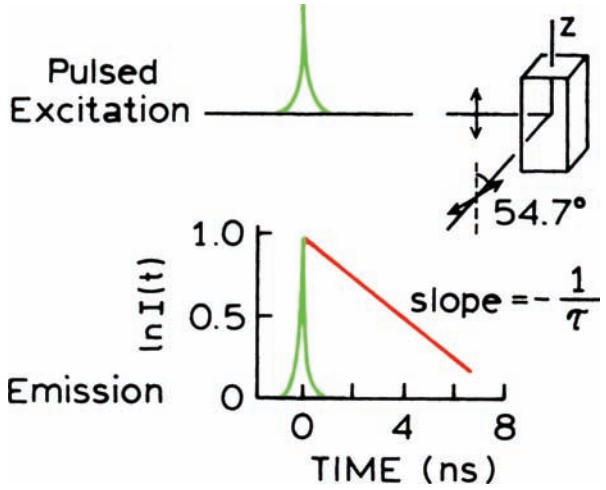

Figure 4.1. Pulse or time-domain lifetime measurements.

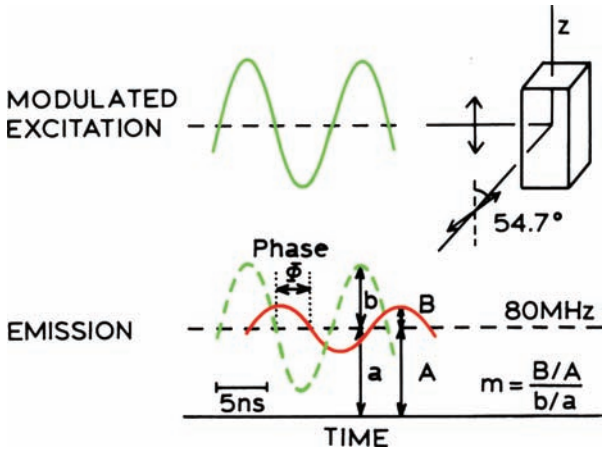

Figure 4.2. Phase-modulation or frequency-domain lifetime measurements. The ratios B/A and b/a represent the modulation of the emission and excitation, respectively.

time-domain and frequency-domain measurements are in widespread use.

4.1.1. Meaning of the Lifetime or Decay Time

Prior to further discussion of lifetime measurements, it is important to have an understanding of the meaning of the lifetime τ. Suppose a sample containing the fluorophore is excited with an infinitely sharp (δ-function) pulse of light. This results in an initial population (n_0) of fluorophores in the excited state. The excited-state population decays with a rate $\Gamma + k_{nr}$ according to

$$\frac{dn(t)}{dt} = (\Gamma + k_{nr})\, n(t) \tag{4.1}$$

where $n(t)$ is the number of excited molecules at time t following excitation, Γ is the emissive rate, and k_{nr} is the nonradiative decay rate. Emission is a random event, and each excited fluorophore has the same probability of emitting in a given period of time. This results in an exponential decay of the excited state population, $n(t) = n_0 \exp(-t/\tau)$.

In a fluorescence experiment we do not observe the number of excited molecules, but rather fluorescence intensity, which is proportional to $n(t)$. Hence, eq. 4.1 can also be written in terms of the time-dependent intensity $I(t)$. Integration of eq. 4.1 with the intensity substituted for the number of molecules yields the usual expression for a single exponential decay:

$$I(t) = I_0 \exp(-t/\tau) \tag{4.2}$$

where I_0 is the intensity at time 0. The lifetime τ is the inverse of the total decay rate, $\tau = (\Gamma + k_{nr})^{-1}$. In general, the inverse of the lifetime is the sum of the rates which depopulate the excited state. The fluorescence lifetime can be determined from the slope of a plot of log $I(t)$ versus t (Figure 4.1), but more commonly by fitting the data to assumed decay models.

The lifetime is the average amount of time a fluorophore remains in the excited state following excitation. This can be seen by calculating the average time in the excited state <t>. This value is obtained by averaging t over the intensity decay of the fluorophore:

$$\langle t \rangle = \frac{\int_0^\infty tI(t)\,dt}{\int_0^\infty I(t)\,dt} = \frac{\int_0^\infty t \exp(-t/\tau)\,dt}{\int_0^\infty \exp(-t/\tau)\,dt} \tag{4.3}$$

The denominator is equal to τ. Following integration by parts, one finds the numerator is equal to τ^2. Hence for a single exponential decay the average time a fluorophore remains in the excited state is equal to the lifetime:

$$\langle t \rangle = \tau \tag{4.4}$$

It is important to note that eq. 4.4 is not true for more complex decay laws, such as multi- or non-exponential decays. Using an assumed decay law, an average lifetime can always be calculated using eq. 4.3. However, this average lifetime can be a complex function of the parameters describing the actual intensity decay (Section 17.2.1). For this reason, caution is necessary in interpreting the average lifetime.

Another important concept is that the lifetime is a statistical average, and fluorophores emit randomly throughout the decay. The fluorophores do not all emit at a time delay equal to the lifetime. For a large number of fluorophores some will emit quickly following the excitation, and some will emit at times longer than the lifetime. This time distribution of emitted photons is the intensity decay.

4.1.2. Phase and Modulation Lifetimes

The frequency-domain method will be described in more detail in Chapter 5, but it is valuable to understand the basic equations relating lifetimes to phase and modulation. The modulation of the excitation is given by b/a, where a is the average intensity and b is the peak-to-peak height of the incident light (Figure 4.2). The modulation of the emission is defined similarly, B/A, except using the intensities of the emission (Figure 4.2). The modulation of the emission is measured relative to the excitation, $m = (B/A)/(b/a)$. While m is actually a demodulation factor, it is usually called the modulation. The other experimental observable is the phase delay, called the phase angle (ϕ), which is usually measured from the zero-crossing times of the modulated components. The phase angle (ϕ) and the modulation (m) can be employed to calculate the lifetime using

$$\tan\phi = \omega\tau_\phi, \quad \tau_\phi = \omega^{-1}\tan\phi \tag{4.5}$$

$$m = \frac{1}{\sqrt{1 + \omega^2\tau_m^2}}, \quad \tau_m = \frac{1}{\omega}\left[\frac{1}{m^2} - 1\right]^{1/2} \tag{4.6}$$

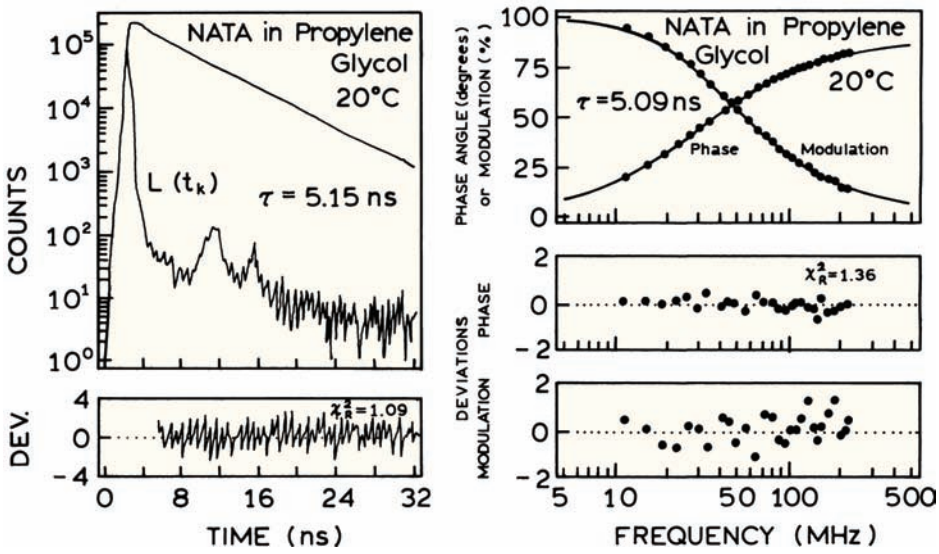

Figure 4.3. Comparison of time-domain (left) and frequency-domain (right) decay time measurements of N-acetyl-L-tryptophanamide (NATA). $L(t_k)$ is the instrument response function.

These expressions can be used to calculate the phase (τ_ϕ) and modulation (τ_m) lifetimes for the curves shown in Figure 4.2 (Problem 4.1). If the intensity decay is a single exponential, then eqs. 4.5 and 4.6 yield the correct lifetime. If the intensity decay is multi- or non-exponential, then eqs. 4.5 and 4.6 yield apparent lifetimes that represent a complex weighted average of the decay components.

4.1.3. Examples of Time-Domain and Frequency-Domain Lifetimes

It is useful to understand the appearance of the time-domain (TD) and the frequency-domain (FD) data. TD and FD data are shown for the tryptophan derivative N-acetyl-L-tryptophanamide (Figure 4.3). This tryptophan derivative (NATA) is known to display a single exponential decay (Chapter 17). In the time domain (left) the data are presented as log counts versus time. The data are presented as photon counts because most such measurements are performed by single-photon counting. The plot of the log intensity versus time for NATA is linear, which indicates the decay is a single exponential. The noisy curve marked $L(t_k)$ is the instrument response function (IRF), which depends on the shape of the excitation pulse and how this pulse is detected by the instrument. This IRF is clearly not a δ-function, and much of the art of lifetime measurements is accounting for this nonideal response in analyzing the data.

Analysis of the time domain is accomplished mostly by nonlinear least squares.[1–2] In this method one finds the lifetime that results in the best fit between the measured data and the data calculated for the assumed lifetime. Although not separately visible in Figure 4.3 (left), the calculated intensity decay for τ = 5.15 ns overlaps precisely with the number of photons counted in each channel. The lower panel of Figure 4.3 (left) shows the deviations between the measured and calculated data, weighted by the standard deviations of each measurement. For a good fit the deviations are random, indicating the only source of difference is the random error in the data.

Frequency-domain data for the same NATA sample are shown in Figure 4.3 (right). The phase and modulation are measured over a range of light modulation frequencies. As the modulation frequency is increased the phase angle increases from 0 to 90°, and the modulation decreases from 1 (100%) to 0 (0%). As for the time-domain data, the frequency-domain data are also analyzed by nonlinear least squares. The dots represent the data, and the solid line represents the best fit with a single lifetime of 5.09 ns. As for the TD data, the goodness-of-fit is judged by the differences (deviations) between the data and the calculated curves. For the FD data there are two observables—phase and modulation—so there are two sets of deviations (lower panel). The randomness of the deviations indicates that a single lifetime is adequate to explain the data.

4.2. BIOPOLYMERS DISPLAY MULTI-EXPONENTIAL OR HETEROGENEOUS DECAYS

At first glance the measurement of decay times seems straightforward (Figure 4.3), so why do these measurements receive so much attention? Interpretation of the data in Figure 4.3 was relatively simple because the decays were single exponentials. However, most samples display more than one decay time. This situation is illustrated by a protein with two tryptophan residues (Figure 4.4). Suppose that both residues display lifetimes of 5 ns. Then the decay would be a simple single exponential decay. The decay would be simple to analyze, but one could not distinguish between the two tryptophan residues. Now suppose a collisional quencher is added and that only the residue on the surface of the protein is accessible to quenching. Assume that the added quencher reduces the lifetime of the exposed residue to 1 ns. The intensity decay is now a double exponential:

$$I(t) = \alpha_1 e^{-t/5.0} + \alpha_2 e^{-t/1.0} \tag{4.7}$$

In this expression the α_i values are called the pre-exponential factors. For the same fluorophore in different environments, which usually display the same radiative decay rates, the values of α_i represent the fractional amount of fluorophore in each environment. Hence, for the protein shown in Figure 4.4 one expects $\alpha_1 = \alpha_2 = 0.5$. The presence of two decay times results in curvature in the plot of log $I(t)$ versus time (dashed). The goal of the intensity decay measurements is to recover the decay times (τ_i) and amplitudes (α_i) from the $I(t)$ measurements.

The presence of two decay times can also be detected using the frequency-domain method. In this case one examines the frequency response of the sample, which consists of a plot of phase and modulation on a logarithmic frequency axis. The longer lifetime tryptophan ($\tau_1 = 5$ ns, solid) and the shorter lifetime tryptophan ($\tau_2 = 1$ ns, dotted) each display the curves characteristic of a single decay time. In the presence of both decay times ($\tau_1 = 5$ ns and $\tau_2 = 1$ ns, dashed), the frequency response displays a more complex shape that is characteristic of the heterogeneous or multi-exponential intensity decay. The FD data are used to recover the individual decay times (τ_i) and amplitudes (α_i) asso-

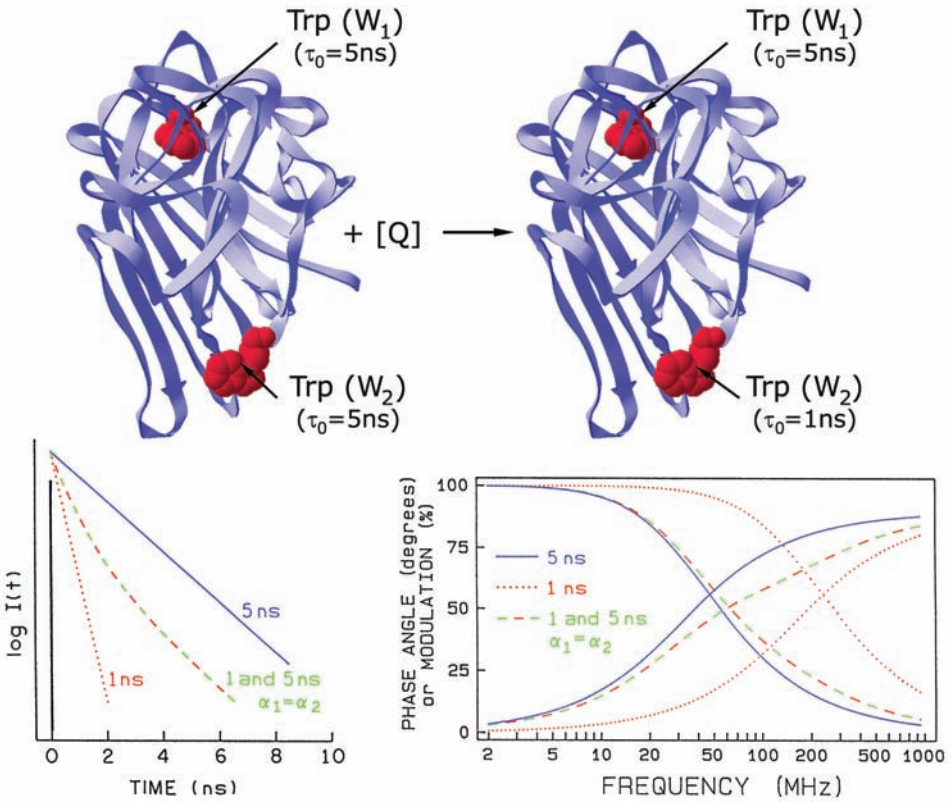

Figure 4.4. Simulated intensity decays of buried (W_1) and exposed (W_2) tryptophan residues in the absence and presence of a collisional quencher.

ciated with each decay time, typically using fitting by nonlinear least squares.

Examination of Figure 4.4 shows that the $I(t)$ values start at the same initial value. At first this is confusing because the intensity of one of the residues was decreased 80% by quenching. The intercept remains the same because the α_i values are proportional to the fractional population. For the protein model shown the time-zero intensities of each component are shown to be the same. In general the time-zero intensities of the components in a multi-exponential decay are not equal because the absorption spectra of the residues may not be the same, or some residues may be completely unobservable. An important point about lifetime measurements is that the intensity decay, or phase and modulation values, are typically measured without concern about the actual intensity. Intensity decays are typically fit to the multi-exponential model:

$$I(t) = \sum_i \alpha_i \exp(-t/\tau_i) \tag{4.8}$$

where $\Sigma\alpha_i$ is normalized to unity.

Time-resolved measurements are also used to measure rotational diffusion and association reactions. This information is available from the time-resolved anisotropy decays. Consider a protein that self-associates into a tetramer (Figure 4.5). For a spherical molecule one expects a single decay time for the anisotropy, which is called the rotational correlation time (θ):

$$r(t) = r_0 \exp(-t/\theta) \tag{4.9}$$

In this expression r_0 is the anisotropy at $t = 0$, which is a characteristic spectral property of the fluorophore. The rotational correlation time θ is the time at which the initial anisotropy has decayed to $1/e$ of its original value. The correlation time is longer for larger proteins. If the protein monomers associate to a larger tetramer, the rotational correlation time will become longer and the anisotropy will decay more slowly. The situation for biomolecules is usually more complex, and the protein can be present in both the monomeric and tetrameric states. In this case the anisotropy decay will be a double exponential:

$$r(t) = r_0 f_M \exp(-t/\theta_M) + r_0 f_T \exp(-t/\theta_T) \tag{4.10}$$

where f_i represents the fraction of the fluorescence from the monomeric and tetrameric proteins, $f_M + f_T = 1.0$. The

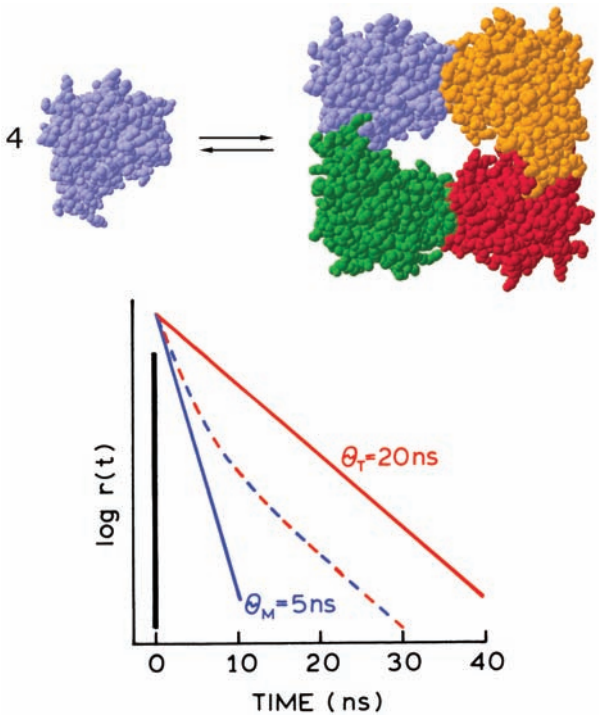

Figure 4.5. Anisotropy decay of a protein monomer (M) that self-associates into a tetramer (T). The dashed line shows the anisotropy decay expected for partially associated monomers.

anisotropy decay will be a double exponential because both monomers and tetramers are present, each with different correlation times. The fractional fluorescence from the monomers and tetramers can be used to calculate the concentrations of each species if their quantum yields are known.

Anisotropy decays can be more complex than eqs. 4.9–4.10. The decays are typically presented as a sum of exponentials:

$$r(t) = \sum_j r_{0j} \exp(-t/\theta_j) \tag{4.11}$$

The meaning of the amplitudes (r_{0j}) and correlation times (θ_j) can depend on the chosen molecular model. The goal of many time-resolved measurements is to determine the form of complex anisotropy decay. In general, it is more difficult to resolve a multi-exponential anisotropy decay (eq. 4.11) than a multi-exponential intensity decay (eq. 4.8).

The intensity decay and anisotropy decay have similar mathematical forms, but there is no direct linkage between the decay times and rotational correlation times. The decay times are determined by the spectral properties of the fluo-

rophore. The rotational correlation times are determined by the size, shape, and flexibility of the macromolecules. Both the decay times and the rotational correlation times are often on the nanosecond timescale. These conditions result in anisotropies that are sensitive to the size of the protein and its interactions with other macromolecules.

4.2.1. Resolution of Multi-Exponential Decays Is Difficult

Why is so much attention given to data analysis and obtaining high signal-to-noise in the time-resolved data? The need for high signal-to-noise is due to the inherent difficulty in recovering the amplitudes and lifetimes for a multi-exponential process. This difficulty was well known to mathematicians, and was pointed out to fluorescence spectroscopists when time-resolved measurements were first being applied to biochemical systems.[3] This paper defined a method for analyzing time-resolved fluorescence data that is still in use today. This paper illustrated how apparently different multi-exponential decays can yield similar $I(t)$ values. Consider the following two double exponential decays:

$$I_1(t) = 7500\ \exp(-t/5.5) + 2500\ \exp(-t/8.0) \qquad (4.12)$$

$$I_2(t) = 2500\ \exp(-t/4.5) + 7500\ \exp(-t/6.7) \qquad (4.13)$$

The pre-exponential factor sum of 10,000 corresponds to 10,000 photons in the highest intensity channel, which is typical of data for time-correlated single-photon counting (TCSPC). From examination of these equations one would think that the intensity decays would be distinct. However, a plot of the intensity decays on a linear scale shows that they are indistinguishable at all times (Figure 4.6). On a logarithmic scale one notices some minor differences at 30–50 ns. However, at 50 ns there are only about 3 photons per channel with a 1-ns width. The difference between the two decays at long times is just 1–2 photons. If one adds the Poisson noise, which is unavoidable in photon-counting data, the differences between the curves is seven-fold less than the uncertainties due to the Poisson noise.[4] This illustrates that it is difficult to distinguish between some multi-exponential functions, and that it is difficult to recover the actual values of α_i and τ_i for a multi-exponential decay. A similar result can be obtained from simulations of the frequency-domain data. The simulated frequency responses are visually indistinguishable for these two decay laws.

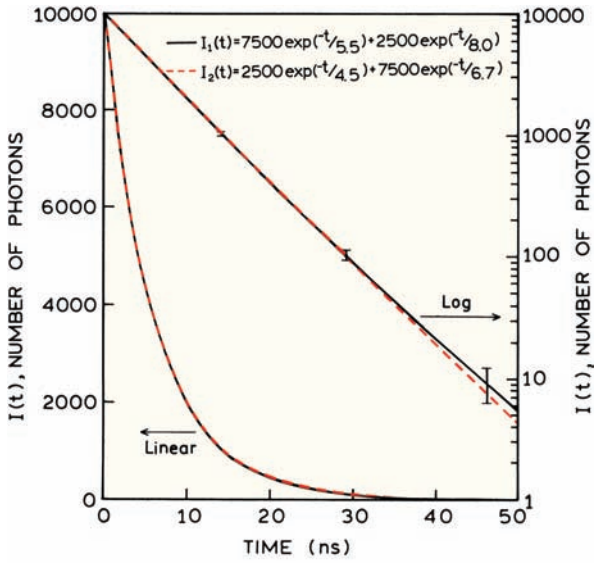

Figure 4.6. Comparison of two intensity decays: on a linear (left) and logarithmic scale (right). The error bars represent Poisson noise on the photon counts. The decay functions were described in [3].

Why is it difficult to resolve multi-exponential decays? In $I_1(t)$ and $I_2(t)$ the lifetimes and amplitudes are different for each decay law. In fact, this is the problem. For a multi-exponential decay one can vary the lifetime to compensate for the amplitude, or vice versa, and obtain similar intensity decays with different values of α_i and τ_i. In mathematical terms the values of α_i and τ_i are said to be correlated. The problem of correlated parameters is well known within the framework of general least-squares fitting.[5–7] The unfortunate result is that the ability to determine the precise values of α_i and τ_i is greatly hindered by parameter correlation. There is no way to avoid this problem, except by careful experimentation and conservative interpretation of data.

4.3. TIME-CORRELATED SINGLE-PHOTON COUNTING

At present most of the time-domain measurements are performed using time-correlated single-photon counting, but other methods can be used when rapid measurements are needed. Many publications on TCSPC have appeared.[4,8–13] One book is completely devoted to TCSPC and provides numerous valuable details.[8] Rather than present a history of the method, we will start by describing current state-of-the-art instrumentation. These instruments use high repetition rate mode-locked picosecond (ps) or femtosecond (fs) laser light sources, and high-speed microchannel plate (MCP)

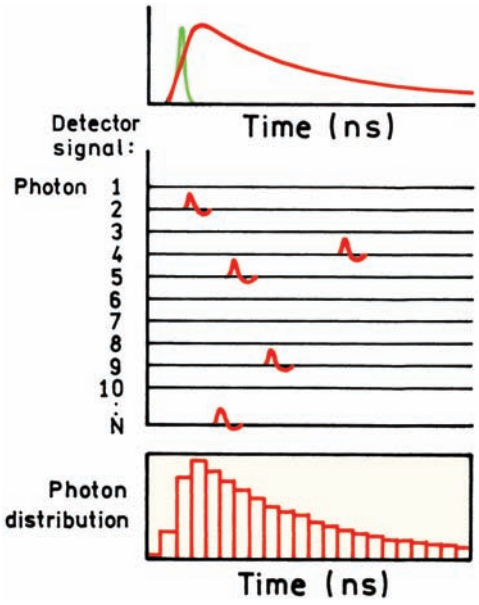

Figure 4.7. Principle of TCSPC. The pulses in the middle panel represent the output from a constant fraction discriminator (see Figure 4.22). Revised from [11].

photomultiplier tubes (PMTs). For many applications, these expensive systems are being rapidly replaced by systems using pulsed-laser diodes (LDs), light-emitting diodes (LEDs), and small, fast PMTs.

4.3.1. Principles of TCSPC

The principle of TCSPC is somewhat unique (Figure 4.7). The sample is excited with a pulse of light, resulting in the waveform shown at the top of the figure. This is the waveform that would be observed when many fluorophores are excited and numerous photons are observed. However, for TCSPC the conditions are adjusted so that less than one photon is detected per laser pulse. In fact, the detection rate is typically 1 photon per 100 excitation pulses. The time is measured between the excitation pulse and the observed photon and stored in a histogram. The *x*-axis is the time difference and the *y*-axis the number of photons detected for this time difference. When much less than 1 photon is detected per excitation pulse, the histogram represents the waveform of the decay. If the count rate is higher the histogram is biased to shorter times. This is because with TCSPC only the first photon can be observed. At present the electronics are not fast enough to measure multiple photons per pulse when the lifetimes are in the nanosecond range. Multiple photons per pulse can be measured for decay times near a microsecond or longer. Specialized electronics are used for measuring the time delay between the excitation and emission (Figure 4.8). The experiment starts with the excitation pulse that excites the samples and sends a signal to the electronics. This signal is passed through a constant function discriminator (CFD), which accurately measures the arrival time of the pulse. This signal is passed to a time-to-amplitude converter (TAC), which generates a voltage ramp that is a voltage that increases linearly with time on the nanosecond timescale. A second channel detects the pulse from the single detected photon. The arrival time of the signal is accurately determined using a CFD, which sends a signal to stop the voltage ramp. The TAC now contains a voltage proportional to the time delay (Δt) between the excitation and emission signals. As needed the voltage is amplified by a programmable gain ampli-

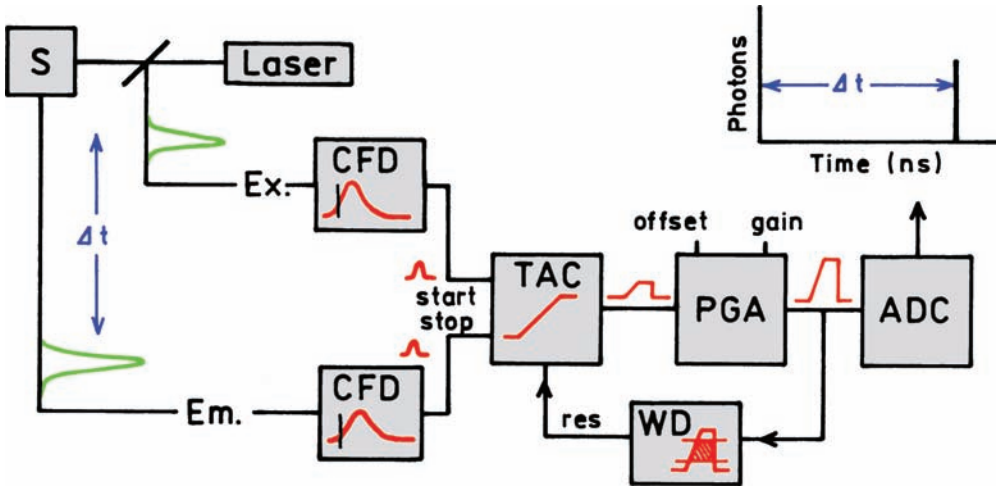

Figure 4.8. Electronic schematic for TCSPC. Revised from [14].

fier (PGA) and converted to a numerical value by the analog-to-digital converter (ADC). To minimize false readings the signal is restricted to given range of voltages. If the signal is not within this range the event is suppressed by a window discriminator (WD). The voltage is converted to a digital value that is stored as a single event with the measured time delay. A histogram of the decay is measured by repeating this process numerous times with a pulsed-light source.

The principle of TCSPC can be understood from the preceding description. However, at present almost all TCSPC measurements are performed in the "reverse mode." The process is the same as described above except that the emission pulse is used to start the TAC and the excitation pulse is used to stop the TAC. This procedure is used because of the high repetition rate of modern pulsed-light sources. The TAC has to be reset and set to zero before each start pulse, which takes a finite amount of time. The TAC can be constantly in reset mode if the start signals arrive too rapidly. The emission signals occur about 1 per 100 excitation pulses, and thus much less frequently than the excitation pulses. These emission pulses are used to start the TAC, and the next laser pulse is used to stop the TAC.

There are many subtleties in TCSPC that are not obvious at first examination. Why is the photon counting rate limited to 1 photon per 100 laser pulses? Present electronics for TCSPC only allow detection of the first arriving photon. The dead times range from 10 microseconds in older systems to about 120 ns with modern TCSPC electronics. These times are much longer than the fluorescence decay. The dead time in the electronics prevents detection of another photon resulting from the same excitation pulse. Recall that emission is a random event. Following the excitation pulse, more photons are emitted at early times than at late times. If all these photons could be measured, then the histogram of arrival times would represent the intensity decay. However, if many arrive, and only the first is counted, then the intensity decay is distorted to shorter times. This effect is described in more detail in Section 4.5.6.

Another important feature of TCSPC is the use of the rising edge of the photoelectron pulse for timing. This allows phototubes with ns pulse widths to provide subnanosecond resolution. This is possible because the rising edge of the single-photon pulses is usually steeper than one would expect from the time response of the PMT. Also, the use of a constant fraction discriminator provides improved time resolution by removing the variability due to the amplitude of each pulse.

4.3.2. Example of TCSPC Data

Prior to examining these electronic components in more detail it is valuable to examine the actual data. Intensity decay for the scintillator 2,5-diphenyl-1,3,4-oxadiazole (PPD) is shown in Figure 4.9. These data were obtained with a cavity-dumped R6G dye laser that was cavity-dumped at 1 MHz and frequency-doubled to 300 nm. The detector was an MCP PMT. There are typically three curves associated with an intensity decay. These are the measured data $N(t_k)$, the instrument response function $L(t_k)$, and the calculated decay $N_c(t_k)$. These functions are in terms of discrete times (t_k) because the counted photons are collected into channels each with a known time (t_k) and width (Δt). The instrument response function (IRF) is the response of the instrument to a zero lifetime sample. This curve is typically collected using a dilute scattering solution such as colloidal silica (Ludox) and no emission filter. This decay represents the shortest time profile that can be measured by

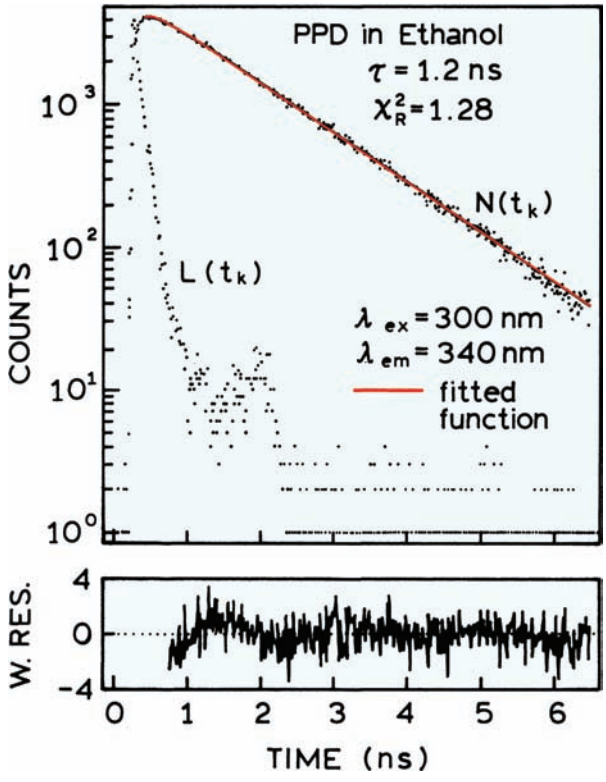

Figure 4.9. TCSPC data for 2,5-diphenyl-1,3,4-oxadiazole (PPD) in ethanol. The light source was an R6G dye laser, cavity dumped at 1 MHz. The detector was an R2809 MCP PMT (Hamamatsu). The left side of the residuals (lower panel) show some minor systematic error. From [15].

the instrument. The width of the IRF is due to both the characteristics of the detector and the timing electronics. The IRF in Figure 4.9 is quite narrow, about 60 ps wide, measured as the full width of the half maximum intensity (FWHM). The use of a logarithmic intensity scale exaggerates the low-intensity regions of the profile. There is an afterpulse about 2 ns after the main peak. Afterpulses are observed with many PMTs. The instrument response function shown in Figure 4.9 is rather good, and some PMTs give far less ideal profiles. For instance, the profile in Figure 4.3 was measured with an end-on linear-focused PMT, for which the afterpulses and long time tail are more significant. However, even in this case (Figure 4.3) the number of photons in the peak of the afterpulse is only about 0.05% of the counts in the peak channel.

The measured intensity decay $N(t_k)$ is shown as a histogram of dots. The height of the dots on the y-axis represents the number of photons that were detected within the timing interval t_k to $t_k + \Delta t$, where Δt is the width of the timing channel. In this case the peak channel, with the largest number of counts, has recorded approximately 3000 photons. On the log scale the decay is seen to be a straight line suggesting a single decay time.

The last curve is the calculated data $N_c(t_k)$, which is usually called the fitted function. This curve (solid) represents a convolution of the IRF with the impulse response function, which is the intensity decay law. The fitted function is the time profile expected for a given intensity decay when one considers the form of the IRF. The details of calculating the convolution are described in the next section. For a single exponential decay the lifetime is the value of τ that provides the best match between the measured data $N(t_k)$ and the calculated time-dependent intensities $N_c(t_k)$. For a multi-exponential decay (eq. 4.2) the analysis yields the values of α_i and τ_i that are most consistent with the data.

4.3.3. Convolution Integral

It is important to understand why the measured intensity decay is a convolution with the lamp function. The intensity decay law or impulse response function $I(t)$ is what would be observed with δ-function excitation and a δ-function for the instrument response. Equations 4.2, 4.12, and 4.13 are examples of impulse-response functions. Unfortunately, it is not possible to directly measure the impulse response function. Most instrument response functions are 0.5 to 2 ns wide. However, we can imagine the excitation pulse to be a series of δ-functions with different amplitudes.

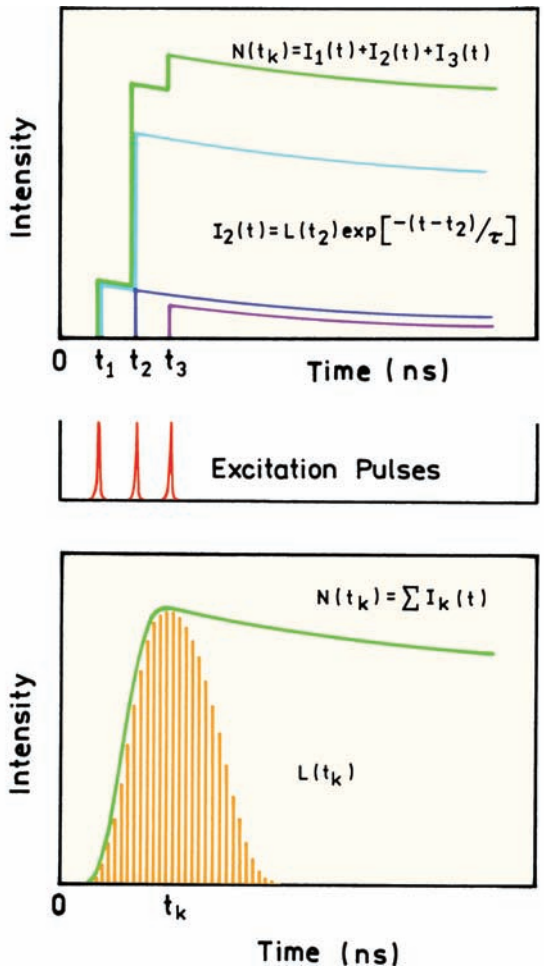

Figure 4.10. Convolution of an impulse response function $I(t)$ with three excitation pulses (top) or with a lamp profile $L(t_k)$ to yield the measured data $N(t_k)$.

Each of these δ-functions excites an impulse response from the sample, with an intensity proportional to the height of the δ-function (Figure 4.10, top). The measured function $N(t_k)$ is the sum of all these exponential decays, starting with different amplitudes and different times.

Mathematically, the concept of convolution can be expressed as follows.[16] Each δ-function excitation is assumed to excite an impulse response at time t_k:

$$I_k(t) = L(t_k)\, I(t - t_k)\Delta t(t > t_k) \qquad (4.14)$$

The amplitude of the impulse response function excited at time t_k is proportional to the excitation intensity $L(t_k)$ occurring at the same time. The term $(t - t_k)$ appears because the impulse response is started at $t = t_k$, and it is understood that

there is no emission from $I(t_k)$ before excitation ($t < t_k$). The measured decay $N(t_k)$ is the sum of the impulse responses created by all the individual δ-function excitation pulses occurring until t_k:

$$N(t_k) = \sum_{t=0}^{t=t_k} L(t_k)I(t - t_k)\Delta t \qquad (4.15)$$

For small values of Δt this equation can be expressed as an integral:

$$N(t) = \int_0^t L(t')I(t - t')dt' \qquad (4.16)$$

This expression says that the experimentally measured intensity at time t is given by the sum of the intensities expected for all the δ-function excitation pulses that occur until time t. It is important to notice that new intensity decays are created in the sample as long as there is nonzero intensity in $L(t_k)$. This is why the intensity decay takes on the shape of the IRF. For convenience the dummy variable of integration is changed using $t' = t - \mu$, so that the convolution integral is expressed as

$$N(t) = \int_0^t L(t - \mu)I(\mu)\,d\mu \qquad (4.17)$$

The task is to determine the impulse response function $I(\mu)$ that best matches the experimental data. Since the data are digital (counts per channel), eq. 4.15 is perhaps the more convenient form. It is important to notice that *time* = 0 is not defined in a TCSPC experiment. There is no zero time because there is no single δ-function initiating the decay. For convenience the excitation pulse is positioned close to zero on the time axis so that one can consider the values of $N(t_k)$ relative to the decay time of the sample. The impulse response function recovered from the analysis does have a defined $t = 0$.

4.4. LIGHT SOURCES FOR TCSPC

4.4.1. Laser Diodes and Light-Emitting Diodes

The instrumentation for TCSPC is moderately complex, and effective use of this method requires understanding of the various components. Measurement of intensity decays requires a pulsed-light source. Prior to 2000 the dominant light sources for TCSPC were picosecond dye lasers or flashlamps. At present the ps dye lasers are being replaced by Ti:sapphire lasers that are still expensive but can be simpler to operate. Perhaps the most important development for TCSPC since 2000 is the introduction of pulsed-laser diodes (LDs) and pulsed light-emitting diodes (LEDs) as simple solid-state sources. These devices consume little power, are easy to operate, and require almost no maintenance. LDs and LEDs make TCSPC measurements more readily available to a wide range of researchers. LDs and LEDs will soon become the dominant light sources for TCSPC of extrinsic fluorophores absorbing above 350 nm. While this chapter was being written, the first report appeared on excitation of intrinsic protein fluorescence using a pulsed LED.[17] It appears likely that the pulsed 280 nm LEDs will soon be generally available and the larger lasers will be less needed for most biochemical applications of fluorescence.

The simplicity of a pulsed LD is shown in Figure 4.11. The output at 405 nm can be used to excite a variety of fluorophores. The pulse width near 70 ps is more than adequate for measuring ns decay times. The repetition rate up to 40 MHz allows rapid data acquisition. If 1% of the puls-

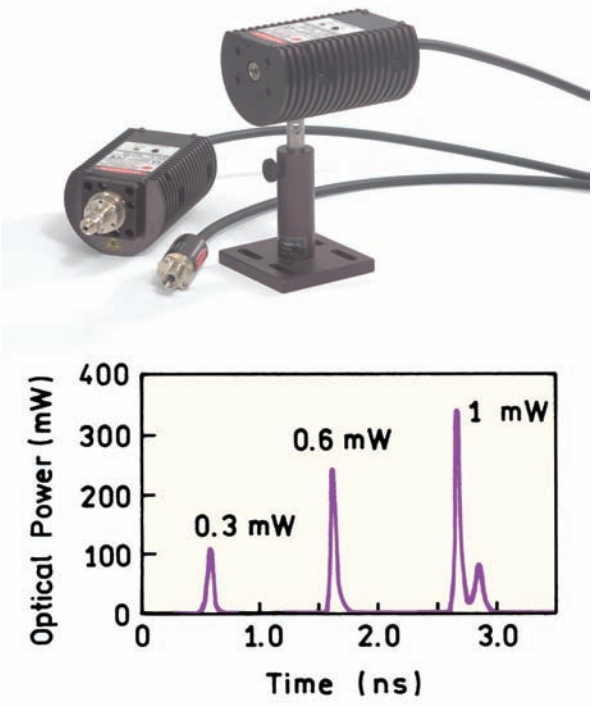

Figure 4.11. Pulsed picosecond laser diode emitting at 370 nm. The FWHM is less than 70 ps with a maximum repetition rate of 40 MHz. From [18].

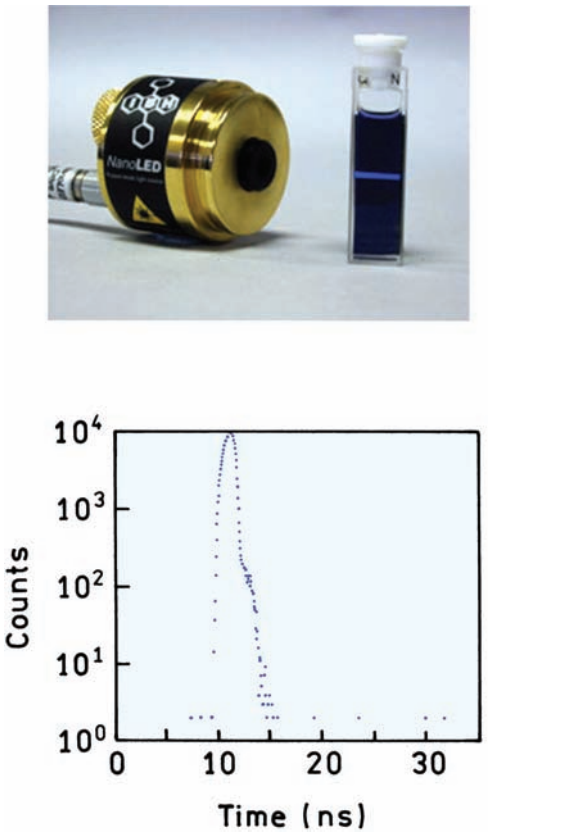

Figure 4.12. Pulsed light-emitting diode at 405 nm. FWHM = 1.4 ns. From [19].

es result in a detectable photon, then up to 400,000 photons per second can be measured. Single exponential decays can be determined with less than 4000 photons, so data acquisition times can be as short as a microsecond. The output is driven directly by the electrical input, so that the repetition rate can be easily varied. This is in contrast to argon, Nd:YAG, or Ti:sapphire lasers, where the repetition rate is determined by the length of the cavity.

An even simpler pulsed-light source is shown in Figure 4.12, in this case a light-emitting diode at 370 nm.[19] In this case the pulse width is about 1.4 ns with an upper repetition rate of 1 MHz. Pulsed LEDs are available with repetition rates up to 40 MHz. A wide range of wavelengths is available for both LEDs and LDs (Figure 4.13).[17–23] Laser diodes have a single-wavelength output and LEDs typically have a wider spectral output. In the near future we can expect LEDs and LDs emitting near 340 and 285 nm.

In addition to simple pulsed-light sources there have also been advances in the electronics for TCSPC (Section 4.5). All the components can be placed on a single computer board,[20] and compact PMT modules are available for photon counting[21] (Section 4.6). As a result it is now possible to obtain compact and reliable instruments for TCSPC (Figure 4.14). Such simple instruments can provide excellent data with short data acquisition times. Figure 4.15 (top) shows the intensity decay of Coumarin 152 obtained with a pulsed LD. The IRF had an FWHM of 50 ps. The absence of systematic errors is seen from the value of $\chi_R^2 = 1.03$ for the single-decay-time fit. Another example is seen in Figure 4.16 (bottom), in this case for fluorescein with pulsed LED excitation at 450 nm. The IRF is about 1 ns due to the wider pulses obtained with LEDs as compared to LDs. These results show that high-quality TCSPC data can now be obtained for many fluorophores without the need for more complex laser systems.

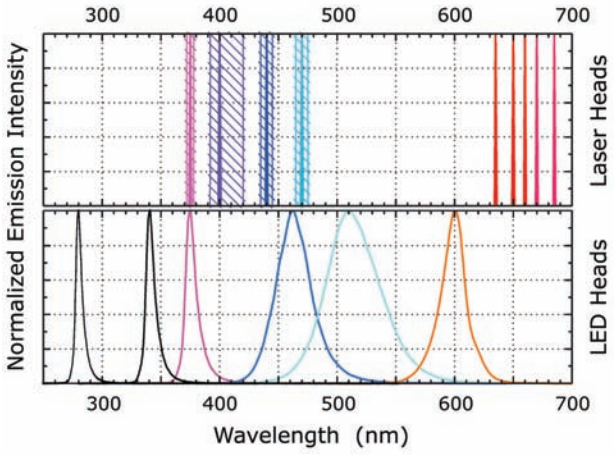

Figure 4.13. Wavelengths available from pulsed LEDs and LDs. Courtesy of Dr. Rainer Erdmann, PicoQuant GmbH.

4.4.2. Femtosecond Titanium Sapphire Lasers

Titanium sapphire lasers are now in widespread use for TCSPC. Ti:sapphire lasers are simpler to operate than

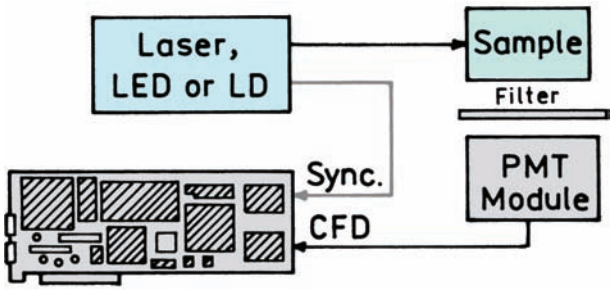

Figure 4.14. Schematic for TCSPC with a pulsed LED or LD.

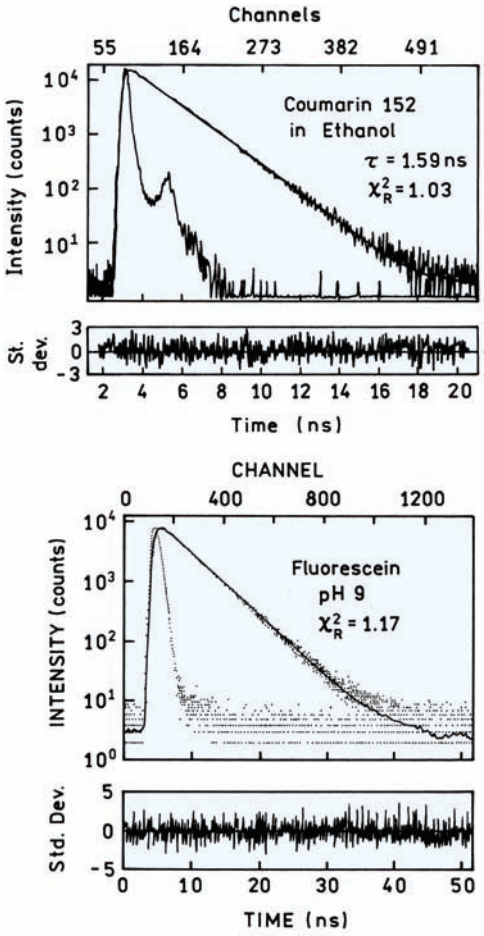

Figure 4.15. **Top**: Intensity decay of Coumarin 152 in ethanol. The light source was a 400-nm laser diode with a 50-ps FWHM and a 20-MHz repetition rate [23]. **Bottom**: Intensity decay of fluorescein in water at pH 9. Excitation at 450 nm with a pulsed LED with a 20-MHz repetition rate and a 1-ns FWHM [22].

mode-locked cavity-dumped dye lasers (Section 4.4.3) but are considerably more complex than LD and LED light sources. These lasers provide pulse widths near 100 fs with high output power; they are widely used for multi-photon excitation and for laser scanning microscopy.

The pump source for a Ti:sapphire laser is a continuous, not mode-locked, argon ion laser (Figure 4.16). Mode-locked lasers are sensitive and somewhat difficult to maintain. In addition to being simpler, the continuous output of an argon ion laser is typically 10–15-fold larger than the mode-locked output. Typically, 15 watts or more are available from an argon ion laser. Ti:sapphire lasers are pumped with up to 7 watts at 514 nm. This allows a Ti:sapphire laser to be pumped with a small frame argon ion laser. At present Ti:sapphire lasers are routinely pumped with solid-state diode-pumped lasers, which are similar to Nd:YAG lasers.

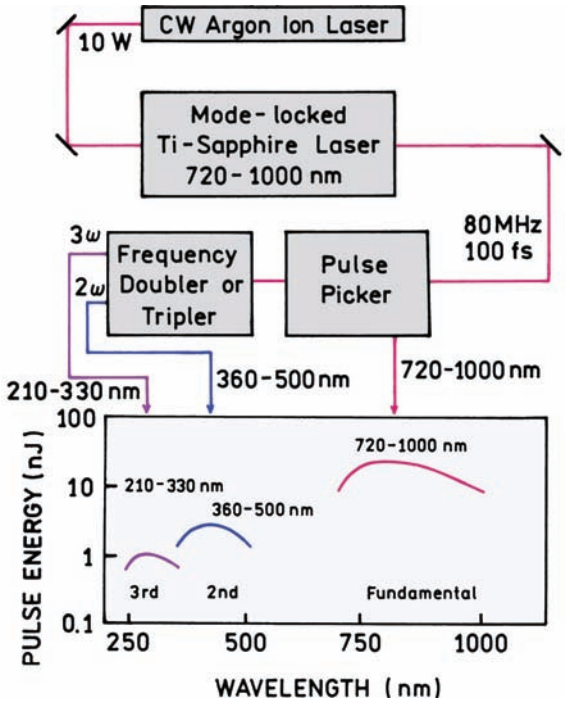

Figure 4.16. Mode-locked femtosecond Ti:sapphire laser.

A favorable feature of the Ti:sapphire lasers are that they are self-mode locking. If one taps a Ti:sapphire when operating in continuous mode, it can switch to mode-locked operation with 100-fs pulses. This phenomenon is due to a Kerr lens effect within the Ti:sapphire crystal. The high-intensity pulses create a transient refractive index gradient in the Ti:sapphire crystal that acts like an acoustooptic mode locker. In fact, the phenomenon is referred to as Kerr lens mode locking. While the laser can operate in this free running mode-locked state, an active mode locker can be placed in the cavity to stabilize the mode-locked frequency and provide synchronization for other parts of the apparatus. However, since it is not necessary to actively maintain the mode-locked condition, the fs Ti:sapphire lasers are stable and reasonably simple to operate.

An advantage of the Ti:sapphire laser is that it is a solid-state device. There are no flowing dyes to be replaced, and the Ti:sapphire crystal seems to have an indefinitely long operational life. Self-mode locking circumvents the need for matching cavity lengths with the pump laser, as must be done with a synchronously pumped dye laser. A disadvantage of the Ti:sapphire laser is that the output is at long wavelengths from 720 to 1000 nm. After frequency doubling the wavelengths from 350 to 1000 nm are ideal for exciting a wide range of extrinsic fluorophores. However, after frequency doubling the wavelengths are too long for

excitation of intrinsic protein fluorescence. This problem can be solved by frequency tripling or third harmonic generation. This is somewhat more complex because one has to double the fundamental output in one crystal and then overlap the second harmonic and fundamental beams in a second crystal. The beams need to be overlapped in time and space, which is difficult with fs pulses. A minor disadvantage of the Ti:sapphire lasers for TCSPC is the use of a pulse picker, instead of a cavity dumper, to decrease the repetition rate. Since mode locking occurs with the laser cavity, rather than being accomplished by synchronous pumping of an external dye laser (Section 4.4.3), a cavity dumper cannot be used with a Ti:sapphire laser. After the 80-MHz pulses exit the laser, the desired pulses are selected with an AO deflector, called a pulse picker. The energy in the other pulses is discarded, and there is no increase in peak power as occurs with cavity dumping. In fact, there is a significant decrease in average power when using a pulse picker. For example, a 100-mW output with an FWMH repetition rate will be decreased to 10 mW if the repetition rate is decreased to 8 MHz with a pulse picker. However, since many fluorophores have lifetimes near a nanosecond, and since TCSPC electronics now allow high repetition rates, nearly the full 80-MHz output can be used in many experiments.

Because of the fs pulse widths and high peak intensities, Ti:sapphire lasers are widely used for two- and multiphoton excitation, particularly in laser scanning microscopy. With this laser one can use the intense fundamental output to excite fluorophores by simultaneous absorption of two or more photons. The use of multiphoton excitation is particularly valuable in microscopy because localized excitation occurs only at the focal point of the excitation beam.

4.4.3. Picosecond Dye Lasers

Before the introduction of pulsed LEDs and LDs the synchronously pumped cavity-dumped dye lasers were the dominant light source for TCSPC. Such lasers provide pulses about 5 ps wide, and the repetition rate is easily chosen from kHz rates up to 80 MHz.

A dye laser is a passive device that requires an optical pump source. The primary light source is usually a mode-locked argon ion laser. Mode-locked neodymium:YAG (Nd:YAG) lasers are also used as the primary source, but they are generally less stable than a mode-locked argon ion laser. Nd:YAG lasers have their fundamental output of 1064 nm. This fundamental output is frequency doubled to 532 nm or frequency tripled to 355 nm in order to pump the dye lasers. The need for frequency doubling is one reason for the lower stability of the Nd:YAG lasers, but heating effects in the Nd:YAG laser rod also contribute to the instability. The argon ion laser has a fundamental output at 514 nm, which is used directly for pumping most laser dyes.

It is not practical to provide a complete description of laser physics, and the reader is referred to the many books on this topic,[24–26] or to a description of laser principles written for chemists.[27] The argon ion mode-locked laser provides pulses at 514 nm, about 70 ps wide, with a repetition rate near 80 MHz. The precise repetition rate is determined by the round-trip time for light pulses within the laser cavity (Figure 4.17). Without active mode locking the argon ion laser would provide a continuous output. This output is changed to an 80-MHz pulse train by a mode-locking crystal within the laser cavity. This crystal is an acoustooptic device that deflects light out of the cavity based on light diffraction by sound waves in the crystal.[28–29]

In order to obtain mode locking there is a delicate balance between the length of the argon ion laser cavity, the resonance frequency at the acoustooptic (AO) crystal, and the driving frequency to the AO crystal. The resonance frequency of the AO crystal and the driving frequency must be matched in order to obtain stable operation. This can be difficult because the resonances of the AO crystal are temperature dependent. For this reason the mode locking crystal is usually thermostatted above room temperature. Once the AO crystal is at a stable temperature and resonance, the cavity length of the argon ion laser must be adjusted so that the round-trip time for photons (near 12 ns for a typical large-frame laser) coincides with the nulls in the AO crystal deflection. Since there are two nulls per cycle, the AO crystal operates near 40 MHz. The laser pulses at 80 MHz exit one end of the laser through a partially transmitting mirror. The presence of the AO modulator within the laser cavity causes the loss of energy at times other than the round-trip time for the photons and the nulls in the AO crystal. If the cavity length matches the AO crystal frequency, then the photons accumulate in a single bunch and bounce back and forth together within laser cavity. This is the mode-locked condition.

One may wonder why the argon lasers are usually mode locked at 514 nm, and not at 488 nm which is the most intense output. Several reasons have been given for the absence of mode locking at 488 nm. It has been stated that the 488-nm line has more gain, so that one obtains modulated but not mode-locked output. Also, there appear

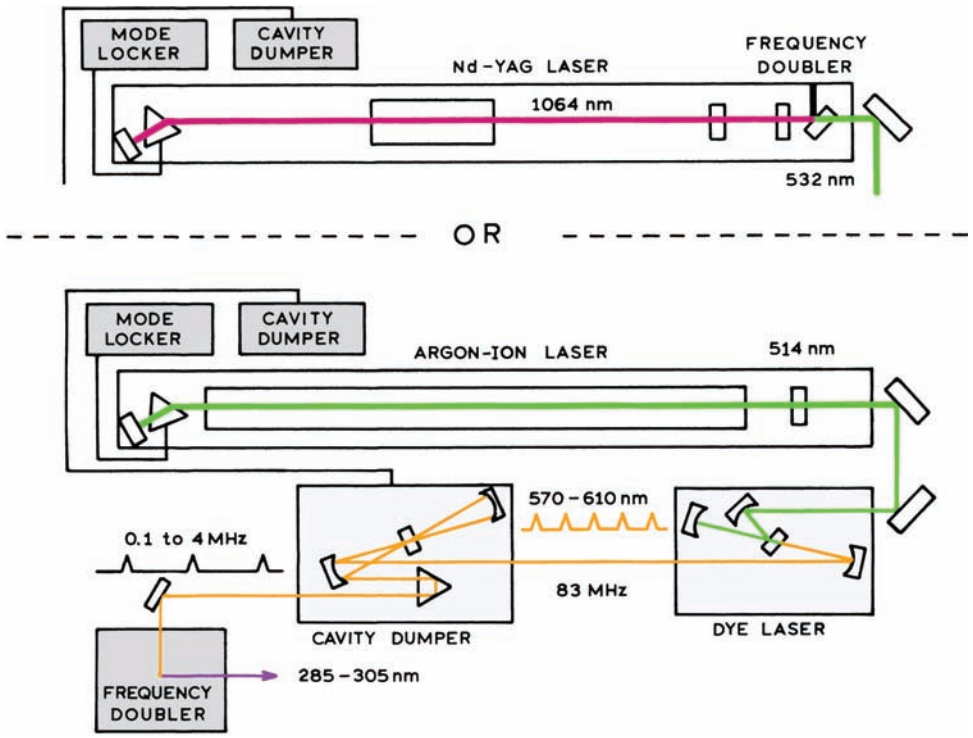

Figure 4.17. Picosecond light sources for TCSPC. The primary pump can be an argon ion or a Nd:YAG laser.

to be two closely spaced lines at 488 nm, which cannot be simultaneously mode locked. In any event, the 514-nm output is convenient for pumping a rhodamine 6G dye laser (R6G), which is perhaps the most stable dye and easiest-to-adjust dye laser for day-to-day use.

Mode-locked argon ion lasers found use in TCSPC starting in the late 1970s and early 1980s.[30–35] However, this light source was not particularly useful for biochemistry unless one had a fluorophore that could be excited at 514 nm. This problem was solved by the introduction of picosecond dye lasers for TCSPC.[36–41] The mode-locked argon (or Nd:YAG) laser is used as the pumping source for a dye laser, typically R6G. The cavity length of the dye laser is adjusted to be exactly the same as that of the argon laser, so that the round-trip time for the photon bunch in the dye laser is the same as in the argon laser. When the cavity lengths are matched, the incoming 514-nm pulses reinforce a single bunch of photons that oscillates at 80 MHz within the dye laser cavity. When this occurs the dye laser is said to be synchronously pumped. To conserve space and to have a stable cavity length, the dye laser cavity is often folded. However, this makes these dye lasers difficult to align because a number of mirrors have to be perfectly aligned, not just two as with a linear cavity. Because of the wide emission curve of R6G, this dye laser has intrinsically narrow pulses, so that a typical pulse width is near 5 ps. This pulse width is narrower than any available detector response, so that for all practical purposes the dye lasers provide δ-function excitation. When using a ps dye laser source the width of the instrument response function is due primarily to the detection electronics and photomultiplier tube.

There are two difficulties with the output of the R6G dye laser. Its wavelength is too long for excitation of most fluorophores, and the repetition rate of 80 MHz is too high for measurement of fluorophores with decay times over 3 ns. At 80 MHz the pulses occur every 12.5 ns, which is too soon for many intensity decays. One typically measures the intensity decay to about four times the mean decay time, so that decay times longer than 3 ns are too long for an 80-MHz pulse rate. This problem is solved using a cavity dumper, which is an acoustooptic device placed within the dye laser cavity. The cavity dumper is synchronized with the argon ion laser and hence also the dye laser. At the desired time when an optical pulse is about to enter the AO crystal, a burst of radio frequency (RF) signal (typically near 400 MHz) is put on the AO crystal. This causes the laser beam to be deflected by a small angle, typically 1–3°.

The deflected beam is captured by a prism, which deflects the beam out of the laser cavity (Figure 4.17). This procedure is called cavity dumping.

For cavity dumping, the AO crystal is pulsed at the desired repetition rate. For instance, for a 1-MHz repetition rate, the RF pulses are sent to the cavity dumping crystal at 1 MHz, which selects one pulse in 80 to be dumped from the dye laser cavity. The RF pulse width is narrow enough to extract a single optical pulse from the dye laser. The arrival times of the acoustooptic and laser pulses have to be matched. The timing of a cavity dumper is typically obtained by dividing the frequency of the mode locker by factors of two, to obtain progressively lower repetition rates. A somewhat confusing terminology is the use of "continuous wave" (CW) to describe the 80-MHz output of a dye laser. This term refers to continuous operation of the cavity dumper, resulting in a continuous train of pulses at 80 MHz.

A valuable aspect of cavity dumping is that it does not typically decrease the average power from the dye laser, at least within the 1–4-MHz range typical of TCSPC. To be specific, if the 80-MHz output of the dye laser is 100 mW, the output of 4 MHz will also be close to 100 mW. When optical power is not being dumped from the dye laser, the power builds up within the cavity. The individual cavity-dumped pulses become more intense, which turns out to be valuable for frequency doubling the output of the dye laser.

A final problem with the R6G dye laser output is its long wavelength from 570 to 610 nm. While shorter wavelength dyes are available, these will typically require a shorter wavelength pump laser. Argon ion lasers have been mode locked at shorter wavelengths, but this is generally difficult. For instance, there are only a few reports of using a mode-locked argon ion laser at 351 nm as an excitation source for TCSPC.[41] Even after this is accomplished, the wavelength is too long for excitation of protein fluorescence. Fortunately, there is a relatively easy way to convert the long-wavelength pulses to shorter wavelength pulses, which is frequency doubling or second harmonic generation. The cavity-dumped dye laser pulses are quite intense. When focused into an appropriate crystal one obtains photons of twice the energy, or half the wavelength. This process is inefficient, so only a small fraction of the 600-nm light is converted to 300 nm. Hence careful separation of the long-wavelength fundamental and short-wavelength second harmonic is needed. The important point is that frequency doubling provides ps pulses, at any desired repetition rate, with output from 285 to 305 nm when using an R6G dye laser. These wavelengths are ideal for excitation of intrinsic protein fluorescence.

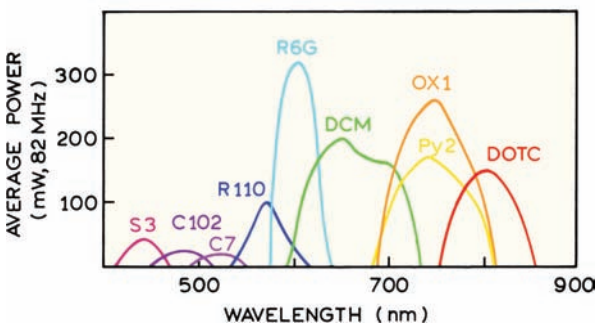

Figure 4.18. Output power of commonly used laser dyes.

A convenient feature of dye lasers is the tunable wavelength. The range of useful wavelengths is typically near the emission maximum of the laser dye. Tuning curves of typical dyes are shown in Figure 4.18. Most of these dye lasers are used after frequency doubling. We use R6G for excitation of intrinsic protein fluorescence, and 4-(dicyanomethylene)-2-methyl-6-(4-dimethylaminostyryl)-4H-pyran (DCM) and Pyridine 2 (Py2) for excitation of extrinsic probes. Excitation of tyrosine requires output of shorter wavelengths than what is available from R6G. Rhodamine 560 and rhodamine 575 were found suitable for tyrosine excitation using an argon ion or Nd:YAG laser pump source, respectively.[42]

4.4.4. Flashlamps

Prior to the introduction of ps lasers, most TCSPC systems used coaxial flashlamps. A wide range of wavelengths is available, depending on the gas within the flashlamp. These devices typically provide excitation pulses near 2 ns wide, with much less power than that available from a laser source. Flashlamp sources became available in the 1960s,[43–45] but their use in TCSPC did not become widespread until the mid-1970s.[46–49] Because of the lower repetition rate and intensity of the flashlamps, long data acquisition times were necessary. This often resulted in difficulties when fitting the data because the time profile of the lamps changed during data acquisition.[50–51] While these problems still occur, the present lamps are more stable, provide higher repetition rates to 50 kHz, and can provide pulse widths near 1 ns.[52-55]

Figure 4.19 shows a typical coaxial flashlamp. Earlier flashlamps were free running, meaning that the spark

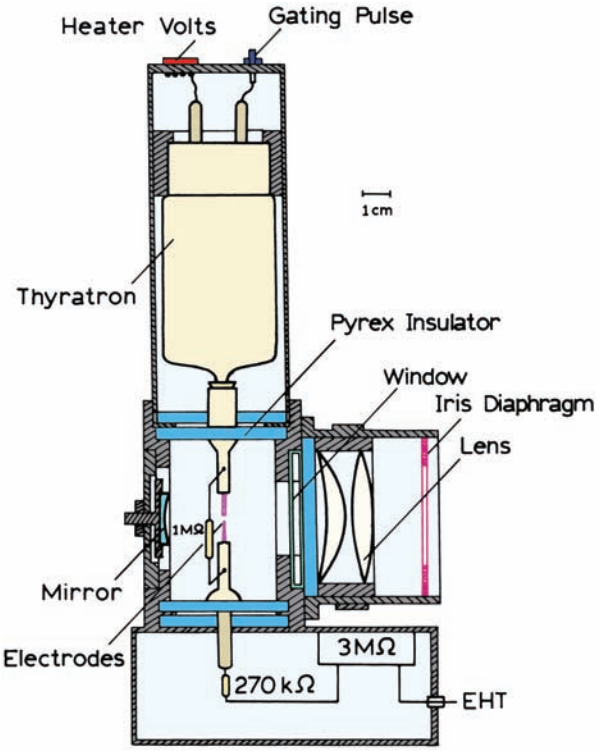

Figure 4.19. Coaxial nanosecond flashlamp. Revised and reprinted with permission from [52]. Copyright © 1981, American Institute of Physics.

occurred whenever the voltage across the electrodes reached the breakdown value. Almost all presently used lamps are gated. The electrodes are charged to high voltage. At the desired time the thyratron is gated on to rapidly discharge the top electrode to ground potential. A spark discharge occurs across the electrodes, which results in a flash of light. These pulses are rather weak, and one frequently has to block the room light to see the flash with the naked eye.

Compared to ion or Ti:sapphire laser sources, flashlamps are simple and inexpensive. Hence, there have been considerable efforts to obtain the shortest pulse widths and highest repetition rates. Despite these efforts, the flashes are much wider than that available with a laser source. One of the shortest time profiles is shown in Figure 4.20 (left), where the full width at half maximum is 730 ps FWHM. More typical is the 1.2-ns FWHM for a flashlamp in which the gas is an argon–hydrogen mixture. Also typical of flashlamps is the long tail that persists after the initial pulse. The spectral output of the pulse lamps depends on the gas, and the pulse width typically depends on both the type of gas and the pressure. Hydrogen or deuterium (Figure 4.21) provides a wide range of wavelengths in the UV, but at low intensity. Nitrogen provides higher intensity at its peak wavelengths, but little output between these wavelengths. In recognition of the growing interest in red and near-infrared (NIR) fluorescence, flashlamps have been developed with red and NIR outputs.[53–54] Given the availability of pulsed LDs and LEDs laser diodes in the red and NIR, there is less motivation to develop red and NIR flashlamps.

The most significant drawback of using a flashlamp is the low repetition rate. The fastest flashlamps have repeti-

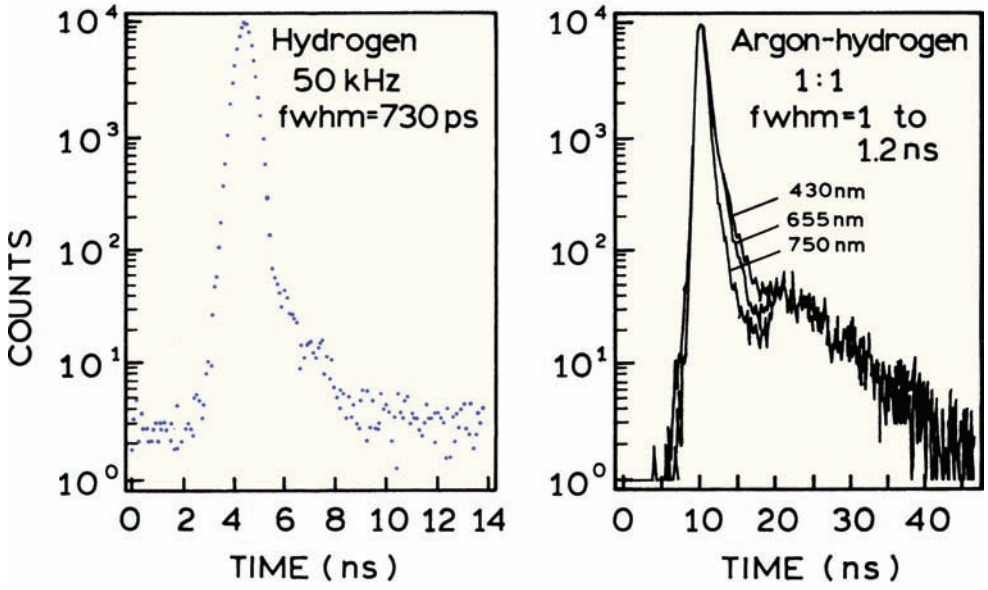

Figure 4.20. Time-profiles of coaxial flashlamps. Revised and reprinted from [9] and [53]. Copyright © 1991, American Institute of Physics.

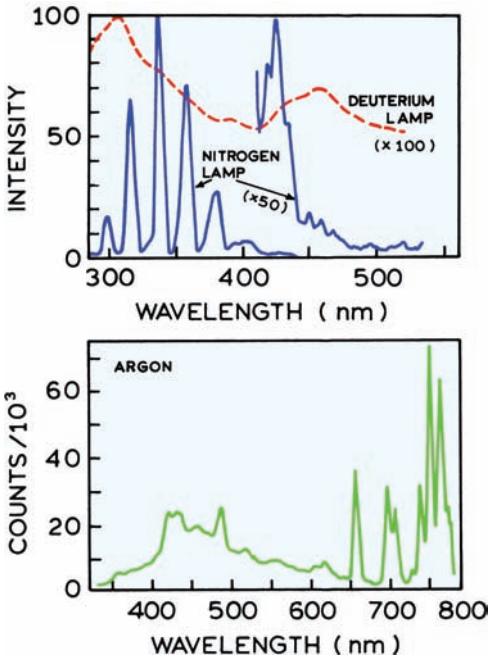

Figure 4.21. Spectral output of flashlamps. The output of the deuterium lamp is 100-fold less than of the nitrogen lamp. It is possible that emission below 600 nm for argon is due to impurities. Revised from [16] and [53].

tion rates up to 100 kHz, with 20 kHz being more common. Recall that one can only collect about one photon per 50 to 100 light pulses, so that the maximum photon count rate is near 200 Hz. Hence, a decay curve with 500,000 counts can take up to 40 minutes to accumulate. The data acquisition time can be decreased using a higher repetition rate and a ratio of stop-to-start pulses above 1%. However, even with the high sensitivity of single-photon counting, the low optical output of the flashlamps can limit sensitivity. For these reasons the higher optical power and faster repetition rates of laser systems makes them the preferred light source for TCSPC.

4.4.5. Synchrotron Radiation

Another light source for TCSPC is synchrotron radiation. If electrons are circulated at relativistic speeds they radiate energy over a wide range of wavelengths. These pulses have clean Gaussian shapes and can be very intense. Instruments for TCSPC have been installed at a number of synchrotron sites.[56–61] Unfortunately, it is rather inconvenient to use these light sources. The experimental apparatus must be located at the synchrotron site, and one has to use the beam when it is available. An advantage of the synchrotron source is that a wide range of wavelengths are available, and all wavelengths appear with the same time distribution.

4.5. ELECTRONICS FOR TCSPC Advanced Material

Prior to 2000, most electronics for TCSPC were based on separate components installed in NIM bins (where NIM stands for Nuclear Instruments Module). At present all the necessary electronic components can be contained on a single or small number of computer boards. Electronics to identify the single photoelectron pulses are often contained within the PMT module. However, it is still valuable to understand the operation of the individual components.

4.5.1. Constant Fraction Discriminators

The first component encountered by the single photoelectron pulses are the constant fraction discriminators (Figure 4.22). The goal is to measure the arrival time of the photoelectron pulse with the highest possible time resolution. This goal is compromised because the pulses due to single photoelectrons have a distribution of pulse lights. If one measures the arrival of the pulses by the time when the signal exceeds a threshold, there is a spread, Δt, in the measured times due to pulse height variations (top panel). While this effect may seem minor, it can be the dominant factor in an instrument response function. Leading-edge discriminators can be used for pulses that all have the same height, which may be true for the trigger (start) channel if the laser system is stable.

The contribution of the pulse height distribution can be minimized by the use of constant fraction discriminators.[62–64] The basic idea of a CFD is to split the signal into two parts, one part of which is delayed by about half the pulse width. The other part of the signal is inverted. When these two parts are recombined, the zero crossing point is mostly independent of the pulse height. The difference between leading-edge and constant-fraction discrimination is remarkable, the timing jitter being 1 ns and 50 ps, respectively.[9] It is important to note that the requirements of a CFD are different for pulses from standard PMTs and MCP PMTs. The shorter pulse width from an MCP PMT means that the time delay in the CFD needs to be smaller in order to properly mix the split signals.[65–67]

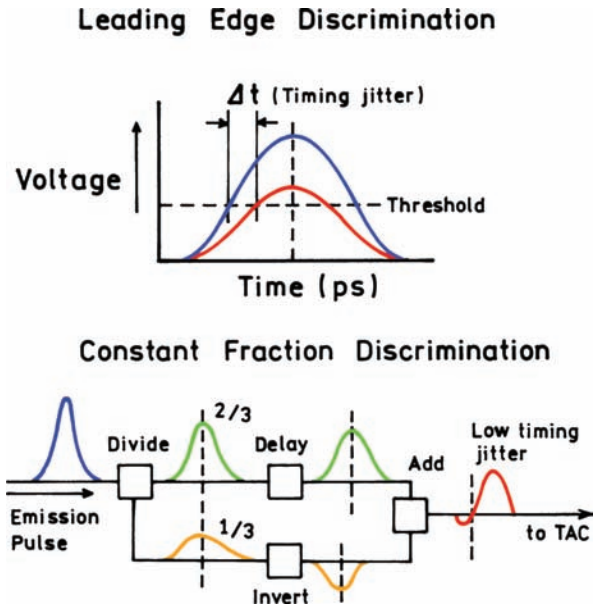

Figure 4.22. Constant fraction discrimination in TCSPC. **Top**: Timing error due to pulse height variations using leading edge discrimination. **Bottom**: Operation of a constant fraction discriminator.

4.5.2. Amplifiers

Amplifiers can be used after the start and stop detectors in order to obtain adequate signal levels for timing. The present trend is to avoid such amplifiers,[65] which can result in additional difficulties. In general, the most noise-free amplification can be obtained within the detector (PMT or photodiode). The cable connecting the detector and amplifier can act as an antenna, resulting in amplification of the RF noise. The use of amplifiers was necessary when MCP PMTs first appeared because the pulses were too short for the CFDs available at that time. Amplifiers were used to broaden the pulses sent to the CFD.[40] This is no longer necessary with newer CFDs. If amplifiers must be used, they should be positioned as close as possible to the detector.

4.5.3. Time-to-Amplitude Converter (TAC) and Analyte-to-Digital Converter (ADC)

The role of the TAC in Figure 4.8 is to generate a voltage proportional to the time between the excitation pulse and the first arriving emitted photon, which are the start and stop pulses, respectively. This is accomplished by charging a capacitor during the time interval between the pulses. Typically the capacitor is charged from 0 to 10 volts over a nanosecond to microsecond time range. For instance, if the chosen range is 50 ns, the capacitor is fully charged at 50 ns. If a stop pulse is received at 25 ns, the charging is stopped at 5 volts. The voltages are calibrated to time delays using delay lines or optical pulses with known time separation. If a stop pulse is not received, the TAC is reset to zero. After the start and stop pulses are received the voltage is connected to a digital value by the ADC. This method of measuring time delays is indirect but provides higher time resolution. At present, inert measurements of time delays cannot be performed accurately enough for nanosecond timescale delays.

In general, the TAC is a rate-limiting component in TCSPC. A certain amount of time is needed to discharge the capacitor and reset the TAC. Prior to about the year 2000, the reset time for most TACs was about 2 ms. This was not a problem with flashlamps where a 50-kHz rate results in start pulses every 20 μs. However, with a high-repetition-rate laser source at 1 MHz, the TAC will be overloaded due to continuous start pulses. The TAC will be instructed to reset before it has completed the previous reset.

The solution to this problem is relatively simple, which is to operate the TAC in reverse mode.[68–70] In this mode of operation the first photon detected from the sample serves as the start pulse, and the signal from the excitation pulse is the stop signal. In this way the TAC is only activated if the emitted photon is detected. The decay curves can appear reversed on the screen of the multichannel analyzer (MCA), but this is corrected by software. The reverse mode of TAC operation is not needed with flashlamps because of their lower repetition rates.

The reset time of a TAC is also called the dead time. A TAC with a 2-μs dead time has a saturated count rate of 0.5 MHz. Photons arriving within the dead time cannot be counted, so the counting efficiency drops. The photon count rate for 50% counting efficiency is sometimes called the maximum useful count rate, which for a 2-μs dead time is 250 kHz. Modern TCSPC electronics have dead times near 125 ns and a saturated count rate of 8 MHz. These electronics can efficiently process and count photons at MHz rates.

An important characteristic of a TAC is its linearity. If the voltage is not linear with time, then the data will contain systematic errors, resulting in difficulties with data analysis. One way to test the linearity of a TAC is by exposure of the detector to a low level of room light, and still use the pulsed-light source to trigger the TAC start signal. Since the photons from the room lights are not correlated with the start pulses, the stop pulses should be randomly distributed across the time range, which is a horizontal line in the mul-

tichannel analyzer (MCA). There were some initial concerns about the linearity of the TAC on the computer boards as compared to the NIM bin systems. However, the problem has been solved and there is no longer a need for NIM bin electronics for TCSPC.

4.5.4. Multichannel Analyzer

In the older systems for TCSPC with separate components there was a multichannel analyzer (MCA). When a separate MCA is present its function is to measure the voltages from the TAC and sort the values according to counts at each particular voltage (time). The MCA first performs an analog-to-digital conversion (ADC), which typically takes about 1–10 μs, during which time the MCA is unable to read another voltage from the TAC. The histogram of the number of counts at each voltage (time) is displayed on a screen. This histogram represents the measured intensity decay. MCAs typically have 2048 to 8192 channels, which can be subdivided into smaller segments. This allows several experiments to be stored in the MCA prior to data transfer and analysis. This ability to store several histograms is particularly important for measurement of anisotropy decays. In this case one needs to measure the two polarized intensity decays, as well as one or two lamp profiles. In the modern systems the MCA is replaced by the ADC with direct transfer of the data into computer memory.

4.5.5. Delay Lines

Delay lines, or a way to introduce time delays, are incorporated into all TCSPC instruments. The need for delay lines is easily understood by recognizing that there are significant time delays in all components of the instrument. A photoelectron pulse may take 20 ns to exit a PMT. Electrical signals in a cable travel a foot in about 1 ns. It would be difficult to match all these delays within a couple of nanoseconds in the start and stop detector channels without a way to adjust the delays. The need for matching delays through the components is avoided by the use of calibrated delay lines. Such delays are part of the NIM bin electronics. However, lengths of coaxial cable are prone to picking up RF interference.

Calibrated delay lines are also useful for calibration of the time axis of the MCA. This is accomplished by providing the same input signal to the start and stop channels of the TAC. The preferred approach is to split an electrical signal, typically from the start detector, and direct this signal to both inputs of the TAC. Since the pulses arrive with a constant time difference, one observes a single peak in the MCA. One then switches the time delay in the start or stop channel by a known amount, and finds the peak shift on the MCA display. By repeating this process for several delay times, the TAC and MCA can be calibrated.

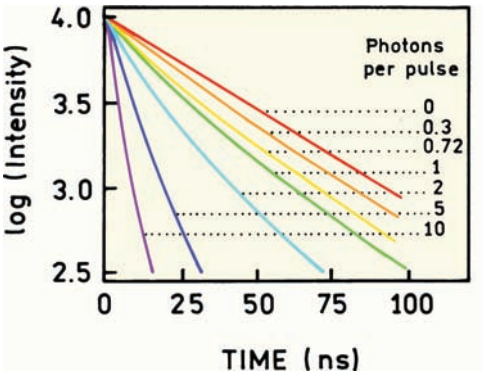

Figure 4.23. Effect of the pulse count rate on a single exponential decay. The numbers are the number of arriving photons per excitation pulse. For a rate of 0.01 or 1% the curve overlaps the actual decay (0). From [4].

4.5.6. Pulse Pile-Up

In TCSPC only one photon from the sample is counted for every 50 to 100 excitation pulses. What errors occur if the average number of detected photons is larger? If more than one photon arrives, how does this affect the measured intensity decay? These questions cannot be answered directly because the electronics limit the experiment to detecting the first arriving photon. Simulations are shown in Figure 4.23 for a single exponential decay with larger numbers of arriving photons. The numbers in the figure refer to the number of observed photons per excitation pulse, not the percentage. The apparent decay time becomes shorter and the decay becomes non-exponential as the number of arriving photons increases. The apparent decay is more rapid because the TAC is stopped by the first arriving photon. Since emission is a random event, the first photon arrives at earlier times for a larger number of arriving photons. Methods to correct for pulse pileup have been proposed,[71–72] but most laboratories avoid pulse pileup by using a low counting rate, typically near 1%. However, this is probably being overcautious,[9] as the measured lifetimes decrease by less than 1% with count rates up to 10%. The intensity decay is only changed by a modest amount for a 30% count rate (Figure 4.23). At present the concerns about pulse pileups

are decreasing because the higher-repetition-rate lasers provide high data rates even with a 1% count rate. Additionally, multichannel systems with multiplexing have become available for TCSPC (Section 4.7).

4.6. DETECTORS FOR TCSPC

4.6.1. Microchannel Plate PMTs

Perhaps the most critical component for timing is the detector. The timing characteristics of various PMTs have been reviewed for their use in TCSPC.[22,27,73–74] At present the detector of choice for TCSPC is the microchannel plate PMT. An MCP PMT provides a tenfold shorter pulse width than any other PMT, and displays lower intensity afterpulses. Also, the effects of wavelength and spatial location of the light seem to be much smaller with MCP PMTs than with linear-focused or side-window tubes. While good time resolution can be obtained with linear-focused and side-window PMTs, the high-speed performance and absence of timing artifacts with an MCP PMT make them the preferred detector for TCSPC.

Development of MCP PMTs began in the late 1970s,[75–78] with the first useful devices appearing in the early to mid-1980s,[79] and their use for TCSPC beginning at the same time.[80–88] The design of an MCP PMT is completely different from that of a dynode chain PMT (Figure 4.24). The factor that limits the time response of a PMT is its transit time spread (TTS), which is the distribution of transit times through the detector. The overall transit time of the electrons through a PMT is not important, as this is just a time delay corrected for in the measurements. However, the distribution of transit times or TTS is important because this spread limits the time resolution of a PMT. One cannot do timing measurements more accurately than the uncertainty in the time it takes a signal to pass through the detector. In a linear-focused PMT the TTS is minimized by designing the dynodes so all the electrons tend to travel along the same path. The TTS of most phototubes is near 2 ns, and it can be less than 1 ns with carefully designed PMTs (Table 4.1).

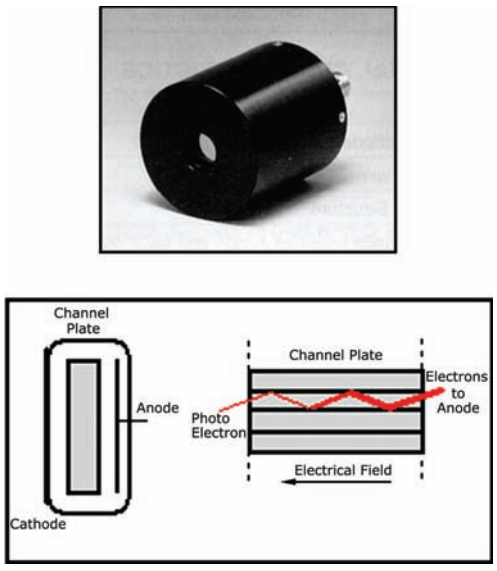

Figure 4.24. Photograph and schematic of an MCP PMT. The diameter of the housing is about 45 mm. Revised from [90–91].

The design of an MCP is completely different because it does not have dynodes. Instead, the photoelectrons are amplified along narrow channels lined with the dynode material (Figure 4.24). Because these channels are very narrow, typically 4 to 12 microns in diameter, the electrons all travel the same path and hence have the same transit time. Smaller channels result in less transit time spread. There are a few additional features in the MCP PMT design that provide improved time response. The channels are angled relative to each other, which prevents feedback between the channels and broadening of the time response.[77–78] Also, the first MCP surface is typically covered with aluminum, which prevents secondary electrons emitted from the top of the MCP from entering adjacent channels.

MCP PMTs provide very low TTS. Figure 4.25 shows the response of an R3809U to femtosecond pulses from a Ti:sapphire laser. The R3809U is now widely used for TCSPC. The FWHM is only 28 ps and the afterpulse a factor of 100 smaller then the primary response. MCP PMTs do have some disadvantages. The photocurrent available from an MCP PMT is typically 100 nA (R2908), as compared to 0.1 mA (R928) for a dynode PMT. This means that the MCP PMT responds linearly to light intensity over a smaller range of incident intensities than does a dynode PMT. The current carrying capacity of an MCP PMT is less because the electrical conductance of the MCPs is low. It is known that the pulse widths from an MCP PMT can depend on the count rate,[88–89] presumably because of voltage changes resulting from the photocurrent. Another disadvantage of the MCP PMTs is their presumed limited useful lifetime which depends on the photocurrent drawn from the tube. In our hands this has not been a problem, and it is difficult to know if an MCP PMT has lost gain due to the total current drawn or due to the inevitable overexposure to light that occurs during the lifetime of a PMT. MCP PMT are

Table 4.1. Transient Time Spreads of Conventional and MCP PMTs[a]

Photomultiplier		Configuration (upper freqeuncy)	TTS (ns)	Dynode
Hamamatsu	R928	Side-on (300 MHz)[b]	0.9	9 stage
	R1450	Side-on	0.76	10 stage
	R1394	Head-on	0.65	10 stage
	R7400	Compact PMT, TO-8 (900 MHz)	300 ps	–
	H5023	Head-on (1 GHz)	0.16	10 stage
RCA	C31000M	Head-on	0.49	12 stage
	8852	Head-on	0.70	12 stage
Philips	XP2020Q	Head-on	0.30	12 stage
Hamamatsu	R1294U	Nonproximity MCP-PMT	0.14	2 MCP
	R1564U	Proximity focused MCP-PMT, 6 micron (1.6–2 GHz)	0.06	2 MCP
	R2809U	Proximity MCP-PMT, 6 micron	0.03[d]	2 MCP
	R3809U	Proximity MCP-PMT Compact size, 6 micron	0.025[d]	2 MCP
	R2566	Proximity MCP-PMT with a grid, 6 micron (5 GHz)[c]	–	2 MCP

[a]Revised from [81].
[b]Numbers in parentheses are the approximate frequencies where the response is 10% of the low-frequency response. The H5023 has already been used to 1 GHz.
[c]From [86].
[d]From [87].

considerably more expensive than dynode PMTs. In general the expense of an MCP PMT is justified only if used with a ps light source.

4.6.2. Dynode Chain PMTs

Dynode PMTs cost less than MCP PMTs and are adequate for many TCSPC experiments, especially if the excitation source is a flashlamp. Two types of dynode PMTs are used for TCSPC: side-window and linear-focused PMTs. Their performance is comparable, but there are minor differences. The side-window tubes are less expensive but can still provide good time resolution. Pulse widths from 112 to 700 ps have been obtained using side-window tubes,[36,92–95] but pulse widths of 1–2 ns are more common. A disadvantage of a side-window PMT is that the time response can depend on the region of the photocathode that is illuminated. Linear-focused PMTs are somewhat more expensive but provide slightly shorter transit time spreads (Table 4.1) and are less sensitive to which region of the photocathode is illuminated. Linear-focused PMTs are probably still the most widely used detectors in TCSPC, but there is a continual shift towards the MCP PMTs and compact PMTs.

4.6.3. Compact PMTs

The expense of TCSPC has been decreased significantly by the introduction of compact PMTs (Figure 4.26). These PMTs are built into standard TO-8 packages.[96–97] Typically these PMTs come in modules that include the dynode chain, a high-voltage power supply, and sometimes the circuits to transform the pulses into TTL level signals. The TTS of these compact PMTs can be short: just 300 ps (Figure 4.25). The compact PMTs appear to be rugged and long-lived and do not have the current limitations of an MCP PMT. These compact PMTs are becoming the detector of choice for most TCSPC instruments.

4.6.4. Photodiodes as Detectors

Photodiodes (PDs) are inexpensive and can respond faster than an MCP PMT. Why are phototubes still the detector of choice? Photodiodes are not usually used for photon counting because of the lack of gain. However, avalanche photodiodes (APDs) have adequate gain and can be as fast as MCP PMTs. The main problem is the small active area. In a PMT or MCP PMT, the area of the photocathode is typically 1 cm x 1 cm, and frequently larger. Photons arriving

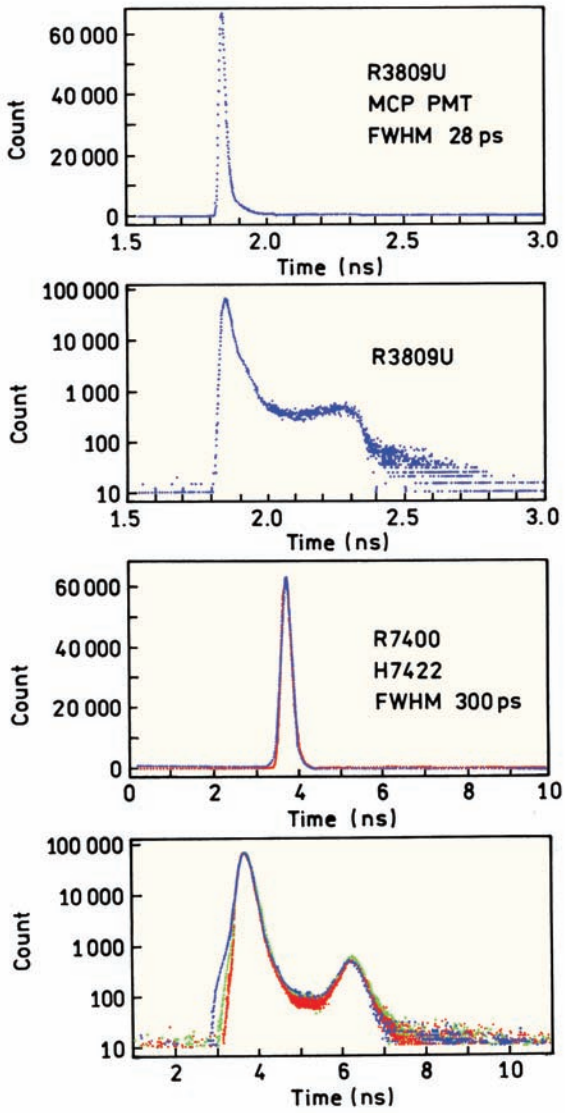

Figure 4.25. Transit time spread for an MCP PMT (R3809U) and a miniature PMT (R7400 series in a H7422 module). Revised from [90].

anywhere on the photocathode are detected. In contrast, the active area of an avalanche photodiode is usually less than 1 mm^2, and less than 10 μm x 10 μm for a high-speed APD. It is therefore difficult to focus the fluorescence onto the APD, so the sensitivity is too low for most measurements. Another disadvantage is the relatively long tail following each pulse, the extent of which depends on wavelength. The presence of a wavelength-dependent tail can create problems in data analysis since the instrument response function will depend on wavelength. Methods have been developed to actively quench the tail. Values of the full width at half

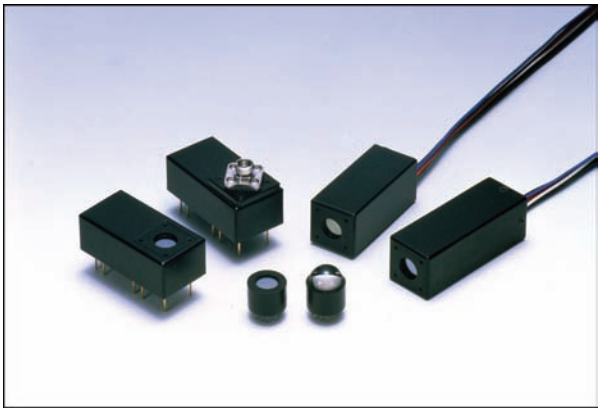

Figure 4.26. Compact PMTs and modules containing the PMTs. The diameter of the PMT is 16 mm. The width of the PMT modules is 25 nm. Courtesy of William Cieslik, Hamamatsu Photonics Systems.

maxima have been reported from 20 to 400 ps, and APDs have been successfully used in TCSPC.[98–105]

APDs are now routinely used for TCSPC, especially in applications where the emission can be tightly focused, such as single-molecule detection (SMD) and fluorescence-correlation spectroscopy (FCS). TCSPC measurements can be performed at the same time as SMD and FCS experiments. APDs have high quantum efficiencies at real wavelengths, and are the detector of choice for these applications.

4.6.5. Color Effects in Detectors

When performing lifetime measurements, one generally compares the response of a fluorescent sample with that of a zero decay time scattering sample. Because of the Stokes shift of the sample, the wavelengths are different when measuring the sample and the impulse response function. The timing characteristics of a PMT can depend on wavelength. Color effects were significant with the older-style tubes, such as the linear-focused 56 DVVP and the side-window tubes.[106–111] The time response of PMTs can also depend on which region of the photocathode is illuminated. Color effects are almost nonexistent in MCP PMTs[80] and do not appear to be a problem with the compact PMTs.

Methods are available to correct for such color effects. There are two general approaches, one of which is to use a standard with a very short lifetime.[112–113] The standard should emit at the wavelength used to measure the sample. Because of the short decay time one assumes that the measured response is the instrument response function. Because

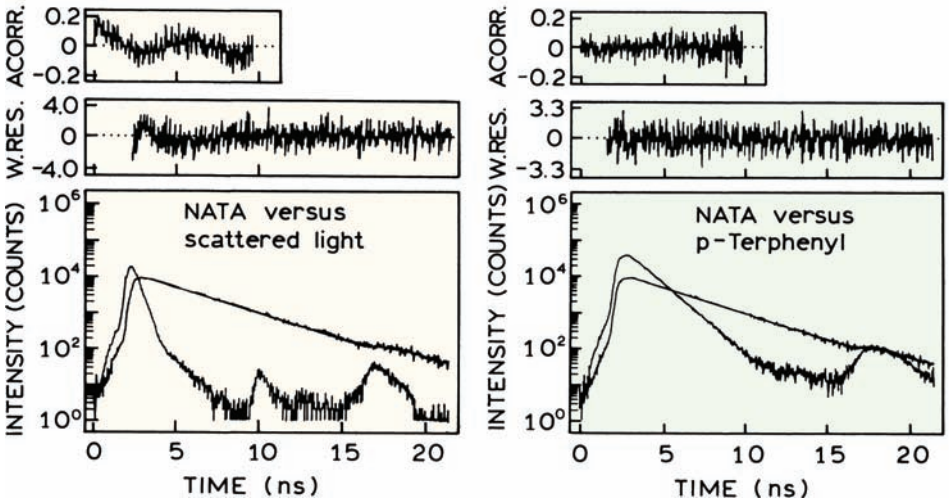

Figure 4.27. Intensity decay of N-acetyl-L-tryptophanamide as measured versus scattered light (left) and using a p-terphenyl lifetime reference (right). Revised from [118].

the wavelengths are matched, one assumes that the color effects are eliminated.

The more common method is to use a standard fluorophore that is known to display a single exponential decay.[114–124] One measures the intensity decay of the sample and the reference fluorophore at the same wavelength. The intensity decays of the reference fluorophore with the known decay time τ_R and of the sample are analyzed simultaneously. In order to correct for the reference lifetime a different functional form is used for $I(t)$:

$$I(t) = \sum_{i=1}^{n} \alpha_i \left[\delta(t) + \left(\frac{1}{\tau_R} - \frac{1}{\tau_i} \right) \exp(-t/\tau_i) \right] \qquad (4.18)$$

where $\delta(t)$ is the Dirac delta-function. In this expression the values of α_i and τ_i have their usual meaning (eq. 4.8). This method is best performed when the decay time of the standard is precisely known. However, some groups vary the assumed decay time of the standard to obtain the best fit.

Figure 4.27 shows how the TCSPC data can be improved using a lifetime standard.[118] N-acetyl-L-tryptophanamide (NATA) is known to display a single exponential decay in water. Its intensity decay was measured with 295 nm excitation from a cavity-dumped frequency-doubled R6G dye laser.[39] The emission was detected with a Philips PM 2254 PMT, which is a linear-focused dynode PMT. When NATA was measured relative to scattered light the fit was fair. However, there were some non-random deviations, which are most easily seen in the autocorrelation trace (Figure 4.27, top left). Also, the goodness-of-fit parameter $\chi_R^2 = 1.2$ is somewhat elevated. The fit was improved when measured relative to a standard, p-terphenyl in ethanol, $\tau_R = 1.06$ ns at 20°C. One can see the contribution of the reference lifetime to the instrument response function as an increased intensity from 5 to 15 ns in the instrument response function (right). The use of the p-terphenyl reference resulted in more random deviations and a flatter autocorrelation plot (top right). Also, the value χ_R^2 was decreased to 1.1. Comparison of the two sides of Figure 4.27 illustrates the difficulties in judging the quality of the data from any single experiment. It would be difficult to know if the minor deviations seen on the left were due to NATA or to the instrument. Some of the earlier reports overestimated the extent of color effects due to low voltage between the photocathode and first dynode. At present, most PMTs for TCSPC use the highest practical voltage between the photocathode and first dynode to minimize these effects. Also, most programs for analysis of TCSPC allow for a time shift of the lamp function relative to the measured decay. This time shift serves to correct for any residual color effects in the PMT. While one needs to be aware of the possibility of color effects, the problem appears to be minor with MCP PMTs and compact PMTs.

Prior to performing any TCSPC measurements it is desirable to test the performance of the instrument. This is best accomplished using molecules known to display single exponential decays.[113] Assuming the sample is pure and decays are a single exponential, deviations from the expected decay can reveal the presence of systematic errors in the

measurements. A number of known single exponential lifetimes are summarized in Appendix II.

As described in Chapter 2, it is also important to test for background fluorescence from blank solutions. Autofluorescence from the sample can result in errors in the intensity decay, which results in confusion and/or erroneous conclusions. There is a tendency to collect the time-resolved data prior to measuring the steady-state spectra of the sample and controls. This is particularly dangerous for time-resolved measurements because the data are often collected through filters, without examining the emission spectra. Measurements may be performed on an impure sample, resulting in a corrupted data set. Since the emission spectra were not recorded the impurity may go undetected. Subsequent analysis of the data is then unsatisfactory, and the source of the problem is not known. In our experience, more time is wasted by not having the spectra than the time needed to record blank spectra prior to time-resolved data collection.

Background correction in TCSPC is straightforward. Data are collected from the blank sample at the same time and conditions as used for the sample. As a result, the background can then be subtracted from the sample data. The source intensity, repetition rate, and other conditions must be the same. Inner filter effects in the samples can attenuate the background signal. If the control samples have a lower optical density, the measured background can be an overestimation of the actual background. If the number of background counts is small, there is no need to consider the additional Poisson noise in the difference data file. However, if the background level is large, it is necessary to consider the increased Poisson noise level in the difference data file.

4.6.6. Timing Effects of Monochromators

As the time resolution of the instrumentation increases one needs to consider the effects of the various optical components. Monochromators can introduce wavelength-dependent time delays and/or broaden the light pulses.[125–126] This effect is shown in Figure 4.28, which shows the path length difference for an optical grating with N facets. Monochromators are usually designed to illuminate the entire grating. The maximum time delay is given by[127]

$$t_d = \frac{\overline{Nm\lambda}}{c} \tag{4.19}$$

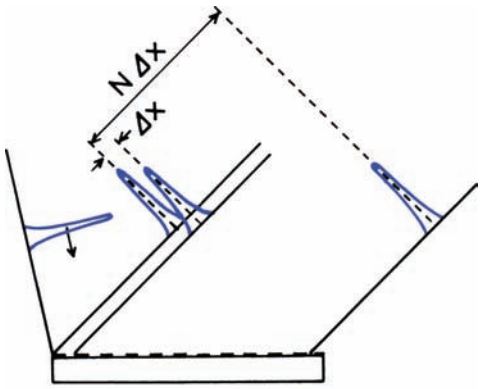

Figure 4.28. Path length difference across a monochromator grating. N is the total number of facets in the grating and Δx in the path length difference between adjacent reflections. From [126].

where N is the number of facets, m is the diffraction order (typically 1), λ is the wavelength, and c is the speed of light. A typical grating may have 1200 lines/mm and be 60 mm across. The maximum time delay at 350 nm is thus 84 ps. While ps and fs laser pulses are not usually passed through a monochromator, this can be expected to broaden the pulse. Alternatively, the apparent intensity decay of a short-lived fluorophore may be broadened by the use of a monochromator to isolate the emission. These effects can be avoided by the use of subtractive dispersion monochromators.[128–129]

4.7. MULTI-DETECTOR AND MULTI-DIMENSIONAL TCSPC

In all the preceding examples TCSPC was performed using a single detector. However, there are many instances where it would be useful to collect data simultaneously with more than one detector. This method is called multidimensional or multichannel TCSPC. These measurements can be accomplished in several ways. One approach is to use a number of completely separate electronics for each channel,[130] which unfortunately results in high complexity and costs. Another approach is to use a single TAC and MCA and to multiply the input from several detectors.[131–135] Recall that TCSPC is limited to detection of about 1 photon per 100 excitation pulses. By using several detectors the overall rate of photon counting can be increased several fold. The maximum counting rate does not increase in direct Using four detectors the
proportion to the number of detectors because of interference between simultaneously arriving signals, but

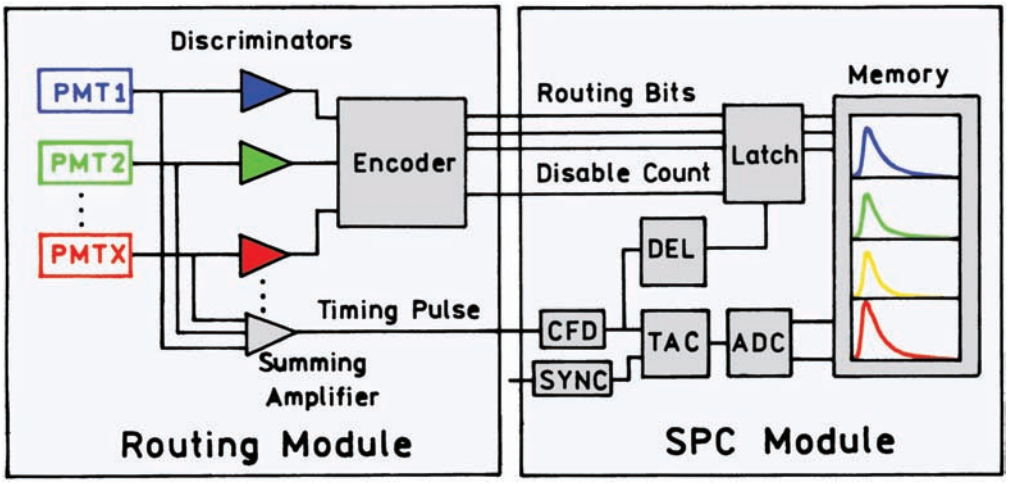

Figure 4.29. Electronic schematic for TCSPC with multiple detectors. Revised from [134].

this is a minor problem compared to the advantages of multidimensional measurements.

Advances in electronics for TCSPC have made multidimensional measurements rather simple, reliable, and relatively inexpensive. Multiple intensity decays can be collected simultaneously at different emission wavelengths or at different locations in a sample. There are numerous potential applications for such measurements in analytical chemistry and cellular imaging. In the future we can expect many if not most TCSPC experiments to be performed with multiple detectors.

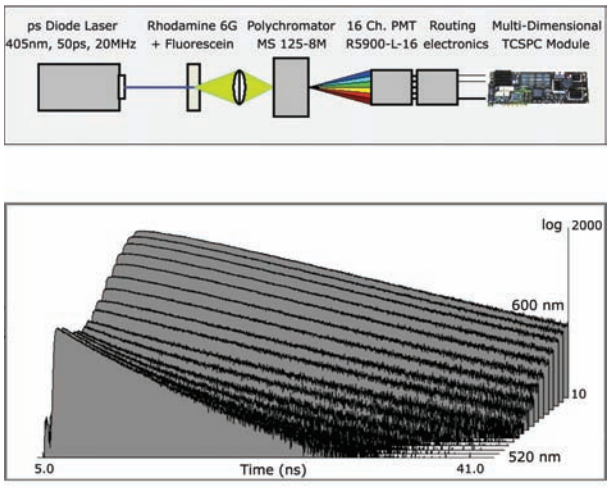

Figure 4.30. Multidimensional TCSPC of a mixture of fluorescein and rhodamine 6G. Excitation was a 405-ns pulse with a ps diode laser, 20 MHz repetition rate. The detector was an R5900-L16, which has 16 separate anodes in a linear geometry. Revised from [134].

Multidimensional capabilities are now easily accessible and are standard in some of the TCSPC electronics. A typical circuit is shown in Figure 4.29. The pulses from 4 to 16 separate detectors are sent to a rotating module that keeps track of their origins and sends them to the TAC and ADC. A single TAC and ADC are used because these are the most expensive, complex, and power-consuming parts of the electronics. After conversion the data are sent to separate blocks of memory as directed by the routing module. If two photons are detected in different channels at the same time, the routing module discards their pulses.

The power and simplicity of multidimensional TCSPC is shown in Figure 4.30 for a mixture of fluorescein and rhodamine 6G. The light source was a ps diode laser. The emission wavelengths were separated and focused onto a multi-anode PMT (Figure 4.31). Such PMTs have a single photocathode and dynodes that maintain the position of the electrons so they arrive at the appropriate anode. The transit time spreads of these PMTs are 0.3 to 0.6 ns, so that nanosecond decay times can be measured. The output from

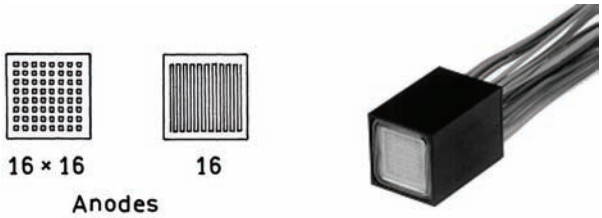

Figure 4.31. Multi-anode PMT for Hamamatsu, R5900. Reprinted with permission from [11,136].

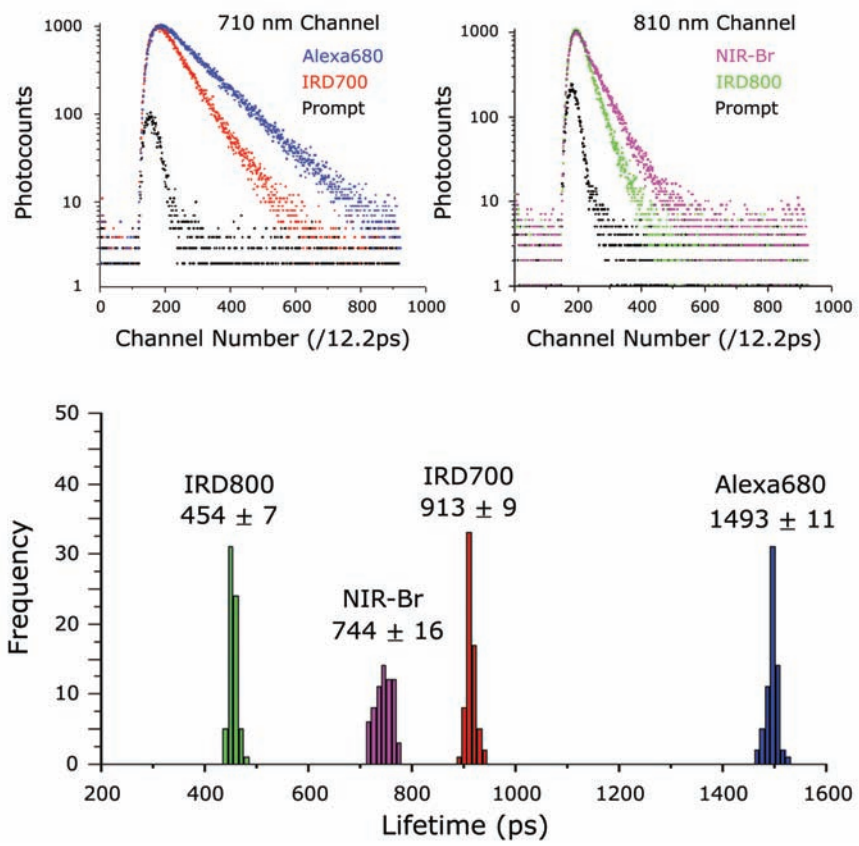

Figure 4.32. Intensity decays and recovered lifetimes of four labeled nucleotides used for DNA sequencing. Revised from [142].

the 16 anodes is sent to a multiplexing TCSPC board that measures the time delays between the start and stop pulses. The system keeps track of the anode that sent the signal, so the counts can be loaded into different regions of memory, which correspond to different wavelengths.

Sixteen decay curves were measured simultaneously for the fluorescein–rhodamine 6G mixture (Figure 4.30). The different decay times are seen from the slopes, which change with emission wavelength. In this case the lifetime of fluorescein was probably decreased by resonance energy transfer to R6G. It is easy to imagine such measurements being extended to time-dependent processes such as resonance energy transfer or solvent relaxation.

4.7.1. Multidimensional TCSPC and DNA Sequencing

An important application of multichannel detection will be DNA sequencing. Because of the large number of bases the sequencing must be performed as inexpensively as possible. Sequencing was initially done using four lanes, one for each base. It would be an advantage to identify the four bases in a single lane. Because of the limited range of available wavelengths and overlap of emission spectra, there is ongoing research to perform sequencing using the decay times of the labeled bases.[137–142] Using four detectors the intensity decays are at four different excitation, and/or emission wavelengths could be measured in a single lane of a sequencing gel. If the decay times of the labeled bases were different, the decay times could be used to identify the bases.

The possibility of DNA sequencing based on lifetime is shown in Figure 4.32. TCSPC data are shown for four probes attached to DNA. These dyes are typical of those used for sequencing. They can be excited with two NIR laser diodes, which can easily occur at different times by turning the laser diodes on and off. The four probes show different lifetimes, and can be identified based on the lifetimes recovered from a reasonable number of counts. Each of the decays in Figure 4.32 were collected in about 7.5 s.

It is easy to imagine how the four fluorophores in Figure 4.32 could be measured simultaneously using multi-detector TCSPC.

TCSPC data are usually analyzed using nonlinear least squares (NLLS) or the method of moments. Both these methods rely on a large number of photon counts, so that the uncertainties in the data have a Gaussian distribution. In applications such as DNA sequencing (Figure 4.32) the goal is not to resolve a multi-exponential decay, but rather to obtain an estimate of a single lifetime. When the number of counts is small the data have a Poissonian distribution rather than a Gaussian distribution. For such data NLLS does not provide the best estimate of the lifetime. The lifetime that is most likely the correct lifetime can be calculated from the maximum likelihood estimates (MLE):[143–144]

$$1 + (e^{T/t} - 1)^{-1} - m(e^{mT/t} - 1)^{-1} = N_t^{-1} \sum_{i=1}^{m} iN_i \qquad (4.20)$$

In this expression m is the number of time bins within the decay profile, N_t is the number of photocounts in the decay spectrum, N_i is the number of photocounts in time bin i, T is the width of each time bin, and τ is the lifetime. This expression allows rapid estimation of the lifetime, which is essential with the high throughput of DNA sequences.

4.7.2. Dead Times, Repetition Rates, and Photon Counting Rates

When examining the specifications for TCSPC electronics it is easy to become confused. The maximum count rates are determined by several factors that affect the rate in different ways depending upon the sample. It is easier to understand these limitations if they are considered separately.

The maximum pulse repetition rate is determined by the decay times of the sample. The time between the pulses is usually at least four times the longest decay time in the sample. If the longest decay time is 12.5 ns then the excitation pulses must be at least 50 ns apart, which corresponds to a repetition rate of 20 MHz. It will not matter if the laser can pulse at a higher frequency, or if the electronics can synchronize to a higher repetition rate laser. For this sample the pulse repetition rate should not exceed 20 MHz.

The maximum photon counting rate is determined by the repetition rate of the laser. For the 20-MHz rate the maximum photon counting rate is 200 kHz, using the 1% rule. The electronics may be able to count photons faster, but the 1% rule and the laser repetition rate limit the maximum photon count rate.

Depending upon the sample the maximum counting rate can be limited by either the sample or the electronics. Suppose the TCSPC electronics are modern with a 125 ns dead time. The maximum count rate is usually listed as the inverse of the dead time, or 8 MHz. However, photons cannot be counted at 8 MHz because the electronics would be busy most of the time and unable to accept start pulses. Detection becomes inefficient because photons arriving within the dead time are not counted. An upper effective count rate is when the counting efficiency decreases to 50% or 4 MHz. It is important to recognize that this is an electronic limitation that is independent of the sample. It would be difficult to obtain a 4-MHz count rate when using the 1% rule. This would require a pulse repetition rate of 400 MHz or 2.5 ns between pulses. This pulse rate could only be used if the lifetime were shorter than 0.625 ns.

The considerations in the previous paragraph indicate the usefulness of multi-detector TCSPC. The count rate of the electronics exceeds the count rate determined by the sample lifetime, so the electronics can process more photons. Input from the multiple detectors is sent to the electronics by the routing module. This module has its own dead time near 70 ns. Hence the saturated count rate from all the detectors is about 14 MHz, but for a 50% counting efficiency is limited to 7 MHz. The dead time of the electronics would not allow efficient photon counting at 7 MHz. The overall count rate can be increased by using multiple independent sets of TCSPC electronics.

In summary, the timing considerations of TCSPC can appear complex. It is easier to consider the problem from first principles than to work backwards from the specifications.

4.8. ALTERNATIVE METHODS FOR TIME-RESOLVED MEASUREMENTS Advanced Material

4.8.1. Transient Recording

While TCSPC and frequency-domain fluorometry are the dominant methods used by biochemists, there are alternative methods for measuring intensity decays. Prior to the introduction of TCSPC, intensity decays were measured using stroboscopic or pulse sampling methods. The basic idea is to repetitively sample the intensity decay during pulsed excitation (Figure 4.33). The detection gate is displaced across the intensity decay until the entire decay is

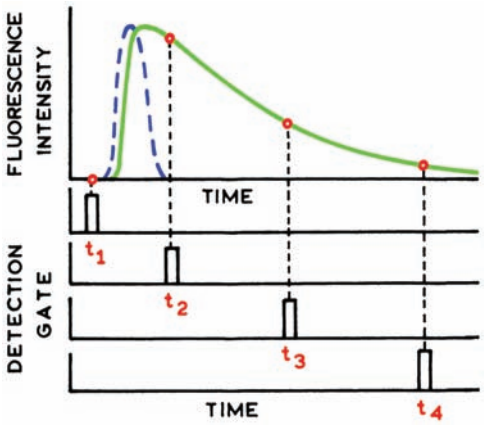

Figure 4.33. Decay time measurements using gated detection in the pulse sampling method. Revised from [10].

measured. In fact, the first time-domain lifetime instruments used gated detection to sample the intensity decay.[44]

Gated detection can be accomplished in two ways. One method is to turn on or gate the gain of the detector for a short period during the intensity decay.[145–146] Surprisingly, this can be accomplished on a timescale adequate for measurement of nanosecond lifetimes. Alternatively, the detector can be on during the entire decay, and the electrical pulse measured with a sampling oscilloscope.[147–148] Such devices can sample electrical signals with a resolution of tens of picoseconds.

While such methods seem direct, they have been mostly abandoned due to difficulties with systematic errors. The flashlamps and N_2 lasers generate RF signals that can be picked up by the detection electronics. This difficulty is avoided in TCSPC because low-amplitude noise pulses are rejected, and only the higher-amplitude pulses due to primary photoelectrons are counted. Also, in TCSPC the standard deviation of each channel can be estimated from Poisson statistics. There are no methods to directly estimate the uncertainties with stroboscopic measurements. Hence, TCSPC became the method of choice due to its high sensitivity and low degree of systematic errors, when the goal of the experiments was resolution of complex intensity decays.

Recent years have witnessed reintroduction of gated detection methods.[149–150] The time resolution can be good but not comparable to a laser source and an MCP PMT. Typical instrument response functions are close to 3 ns wide. An advantage of this method is that one can detect many photons per lamp pulse, which can be an advantage in clinical applications when the decays must be collected rapidly. Gated detection can be used with low-repetition-rate nitrogen lasers, which can also be used to pump dye lasers. An example of directly recorded intensity decay is shown in Figure 4.34. The instrument was designed for studies of skin and tissue using this autofluorescence, so the excitation light was delivered to the sample via an optical fiber.[150] The excitation source was a nitrogen laser excitation source with a repetition rate near 10 Hz. The emission was detected with an APD and digitized on a high-speed oscilloscope. The intensity decay of human skin was collected in about 1 s by averaging of several transients. The IRF is about 5 ns wide but the intensity decay of skin autofluorescence could be recorded. The wide IRF shows why TCSPC is used rather than direct transient recording. At this time it is not possible to directly record nanosecond decays with the accuracy needed for most biochemical studies.

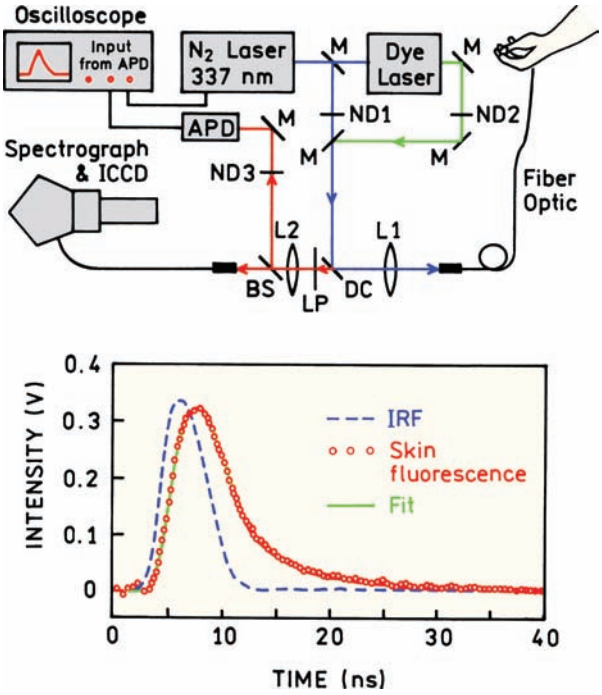

Figure 4.34. Time-resolved instrument using a high-speed oscilloscope for measuring of time-resolved decays of skin of human skin. Revised from [150].

4.8.2. Streak Cameras

Streak cameras can provide time resolution of several ps,[151–160] and some streak cameras have instrument response functions of 400 fs, considerably faster than TCSPC with an MCP PMT. Streak cameras operate by dispersing the photoelectrons across an imaging screen. This can be accom-

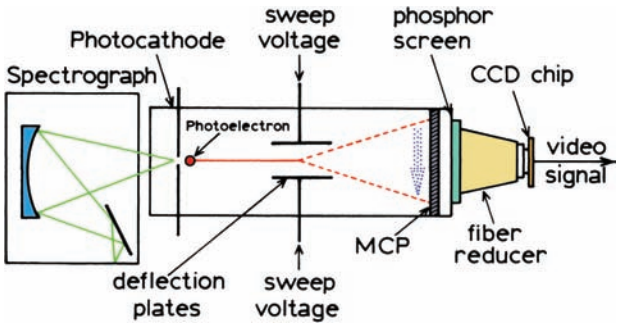

Figure 4.35. Schematic of a streak camera with wavelength resolution. From [152].

plished at high speed using deflection plates within the detector (Figure 4.35). In the example shown, the light is dispersed by wavelength in a line across the front of the photocathode. Hence, streak cameras can provide simultaneous measurements of both wavelength and time-resolved decays. Such data are valuable when studying time-dependent spectral relaxation or samples which contain fluorophores emitting at different wavelengths.

The time resolution obtainable with a steak camera is illustrated in Figure 4.36. The instrument response function is superior to that found with the fastest MCP PMTs. Earlier-generation streak camera were delicate, and difficult to use and synchronize with laser pulses. This situation has changed, and streak cameras have become more widely used, especially for simultaneous measurement of subnanosecond decays over a range of emission wavelength. One example is the decay of PyDMA (Figure 4.37), which decays rapidly due to exciplex formation and solvent relaxation around the charge-transfer (CT) complex.[161] Pyrene in

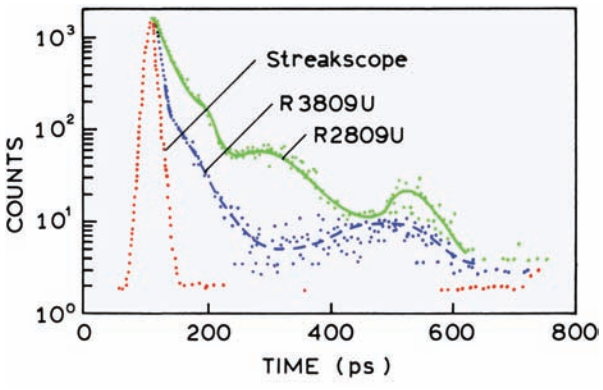

Figure 4.36. Comparison of the instrument response functions of a streak camera and two MCP PMTs (R3809U and R2809U). The 600 nm dye laser pulse width was 2 ps. Revised from [158].

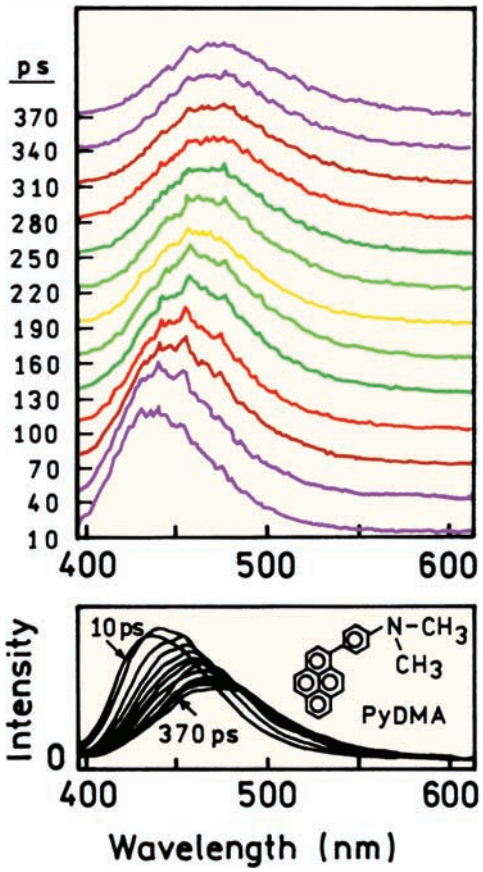

Figure 4.37. Time and wavelength-dependent intensity decays of dimethyl-(4-pyren-1-yl-phenyl)amine (PyDMA) measured with a streak camera. Revised from [161].

the excited state forms a charge-transfer complex, an exciplex, with the linked dimethylphenyl group. The charge-transfer complex is polar and shows a time-dependent spectral shift to longer wavelengths. This shift occurs rapidly and is complete in less than 500 ps. The time-dependent shift to longer wavelength is due to reorientation of the solvent around the CT state. The high temporal resolution of the streak camera allows recording of the complete emission spectra over intervals as short as 10 ps. The data can also be displayed in a format where the axes are time and wavelength and the color reveals the intensity (Figure 4.38).

An important development in streak camera technology is the introduction of the photon-counting streak camera (PCSC).[162] These devices provide single-photon detection with high time resolution (14 ps) and simultaneous wavelength resolution. The photon counts can be collected at high rates because pulse pileup and dead time are not problems with these instruments. A PCSC functions the same as

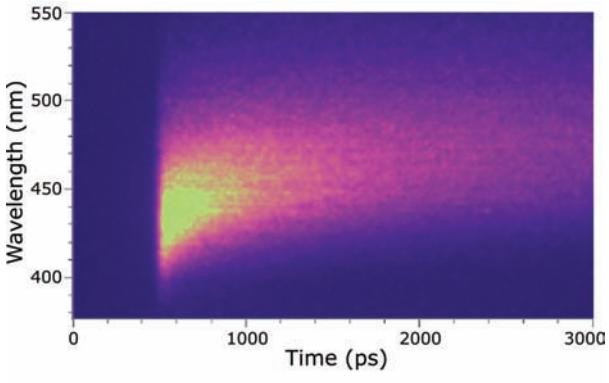

Figure 4.38. Time- and wavelength-dependent intensity decay of PyDMA. Figure courtesy of Professor Hubert Staerk, Max-Planck Institute for Biophysical Chemie, Göttingen, Germany.

the camera shown in Figure 4.35 except for the mode of detection. Instead of digitizing an analog signal, the PCSC counts the pulses on the phosphor screen due to single photoelectrons. The pulses are recorded with a CCD camera. The software examines the size of the pulse and only accepts pulses above a defined threshold, analogous to the discriminator in TCSPC (Figure 4.39). The instrument

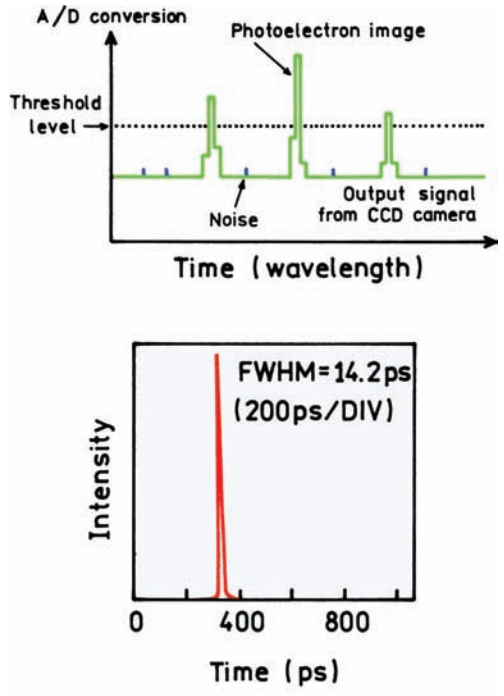

Figure 4.39. Single photoelectron detection and time resolution of a photon counting streak camera. Revised from [162].

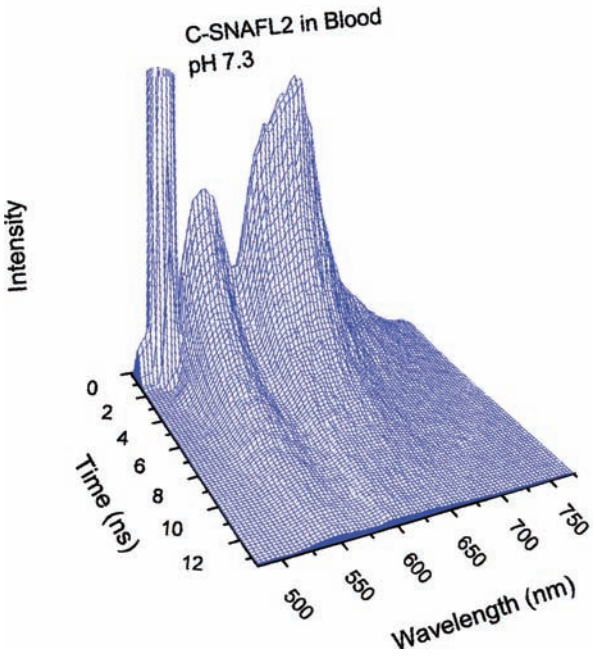

Figure 4.40. Intensity decay of C-Snafl 2 in blood at pH 7.3 measured with a photon counting streak camera. From [163].

response function is the width of a single photoelectron image, which is about 14 ps. There is no dead time because the photons are distributed in space across the photocathode, so more than a single photon can be collected at each wavelength for each laser pulse. Of course the photons cannot be accurately counted if they overlap in time and space on the phosphor screen. Data can be collected at all wavelengths simultaneously because the wavelengths are at different locations on the photocathode.

The high sensitivity of a PCSC allows measurements that would be difficult with more conventional instruments. Figure 4.40 shows intensity decays of a pH probe C-Snafl 2 in blood, which has high absorbance at the excitation wavelength. The decays at all wavelengths were obtained simultaneously. It was not possible to suppress all the scattered light using filters, but the scattered light appears at a different position (wavelength) on the photocathode that minimized its effect on emission of C-Snafl 2. The data from a PCSC can be presented as emission spectra or as intensity decays (Figure 4.41). By seeing the position and intensity of the scattered light it is possible to judge the contributions of the scatter at longer wavelengths. Hence, considerable information about a sample can be obtained in a single measurement.

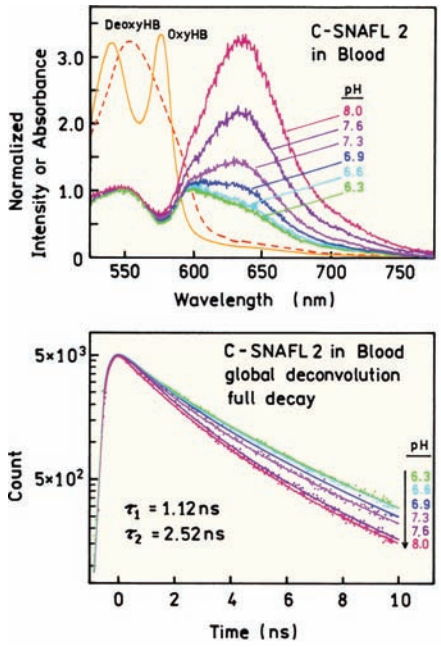

Figure 4.41. Emission spectra and intensity decays of C-Snafl 2 in blood measured with a photon counting streak camera. From [163].

4.8.3. Upconversion Methods

The ultimate time resolution is provided by methods that bypass the limited time-resolution of the detectors, and rely on the ps and fs pulse widths available with modern lasers.[164–166] The basic idea is to pass the fluorescence signal through an upconversion crystal, and to gate the crystal with another ps or fs light pulse (Figure 4.42). One observes the shorter wavelength harmonic generated by the combined effects of the laser pulse and the emission. In this schematic the sample is excited with the second harmonic of a Ti:sapphire laser. The emission is focused on the upconversion crystal. The fundamental output of the Ti:sapphire is focused on the crystal in the same region where the fluorescence is focused. An upconversion signal is generated that is proportional to the emission at the moment the gating pulse arrives. The time resolution is determined by the width of the laser pulse. The time-resolved decay is obtained by measuring the intensity of the upconverted signal as the optical delay time is varied. The signals are typically weak, so that an optical chopper and lock-in detectors sometimes are needed to measure the upconverted signal in the presence of considerable background.

Upconversion provides impressive time resolution; however, the instrumentation is rather complex. For instance, even a seemingly minor change of the emission wavelength can require a major readjustment of the apparatus since the orientation of the upconversion crystal has to be adjusted according to the wavelength. Decay times of more than 1–2 ns are difficult to measure because of the use of a delay line (≈1 ns/foot). Alignment of the delay line can be quite difficult to maintain as the time delay is altered.

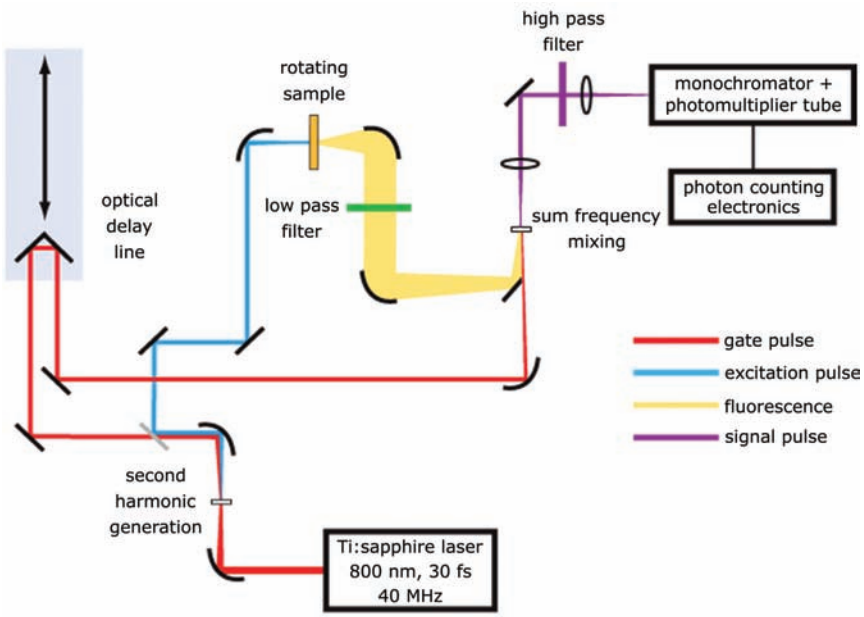

Figure 4.42. Schematic for fluorescence upconversion measurements. Courtesy of Professor Eric Vauthery, University of Geneva, Switzerland.

The high time resolution of upconversion measurements can be illustrated by quenching and exciplex formation of 3-cyanoperylene (PeCN) in neat diethylaniline (DEA).[167–168] The cyano group makes perylene a good electron acceptor, and DEA is a good electron donor. PeCN in the excited state undergoes photoinduced electron transfer (PET) with DEA (Chapter 9). This reaction is very rapid because in DEA the PeCN molecules are surrounded by potential electron donors. Emission spectra of PeCN show that it is highly quenched in DEA as compared to a non-electron-donating solvent (Figure 4.43). The lower panel shows the wavelength-dependent decays of PeCN. The time resolution is limited by the pulse width of the pump lasers, which is near 100 fs. The decay time is about 1 ps for the PeCN emission near 500 nm and about 20 ps for the exciplex emission.

4.8.4. Microsecond Luminescence Decays

For decay times that become longer than about 20 ns, the complexity of TCSPC is no longer necessary. In fact, TCSPC is slow and inefficient for long decay times because of the need to use a low pulse repetitive rate and to wait a long time to detect each photon. In the past such decays would be measured using a sampling oscilloscope. At present the preferred method is to use a multiscalar card. These devices function as photon-counting detectors that sum the number of photons occurring within a time interval. Figure 4.44 shows the operating principle. Following the excitation pulse, photons arriving within a defined time interval are counted. The arrival times within the interval are not recorded. The time intervals can be uniform, but this becomes inefficient at long times because many of the intervals will contain no counts. A more efficient approach is to use intervals that increase with time. The count rates for multiscalars can be high: up to about 1 GHz. At present the minimum width of a time interval is about 1 ns, with 5 ns being more typical. Hence, the multiscalars are not yet practical for measuring ns decays.

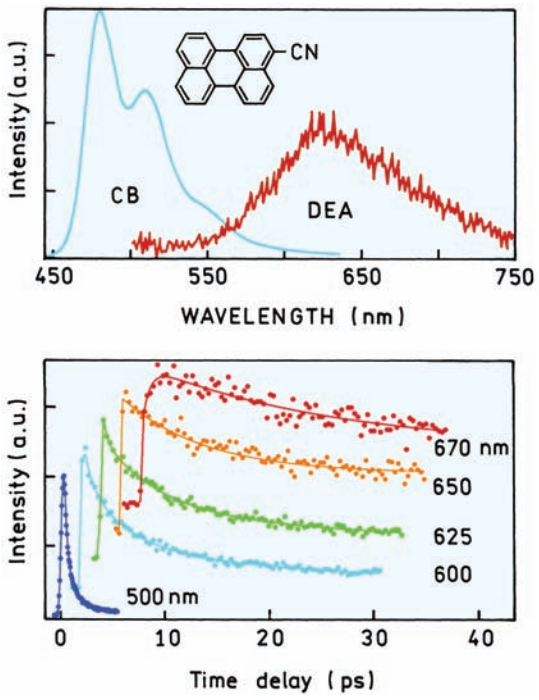

Figure 4.43. Emission spectra and time-resolved decays of 3-cyanoperylene in chlorobenzene (CB) and diethylaniline (DEA). Revised from [168].

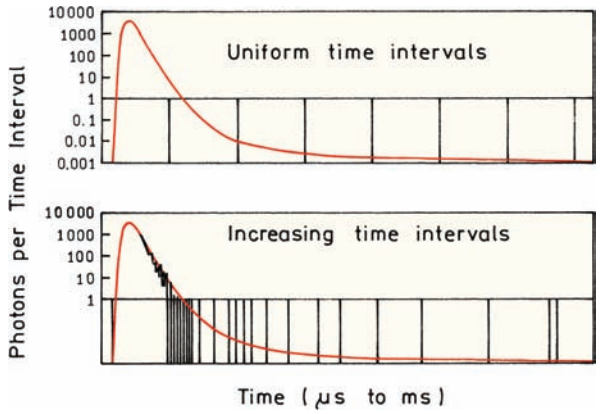

Figure 4.44. Time-resolved intensities measured with a photon counting multiscalar. Revised from [169].

An example of a decay measured with a multiscalar is shown in Figure 4.45. The fluorophore was $[Ru(bpy)_3]^{2+}$, which has a lifetime of several hundred nanoseconds. A large number of counts were obtained even with the long lifetimes. However, the count rate is not as high as one may expect: about 1 photon per 2 laser pulses. The data acquisition time would be much longer using traditional TCSPC with a 1% count rate (Problem 4.6).

4.9. DATA ANALYSIS: NONLINEAR LEAST SQUARES

Time-resolved fluorescence data are moderately complex, and in general cannot be analyzed using graphical methods. Since the mid-1970s many methods have been proposed for analysis of TCSPC data. These include nonlinear least squares (NLLS),[3,16,170] the method-of-moments,[171–173] Laplace transformation,[174–177] the maximum entropy

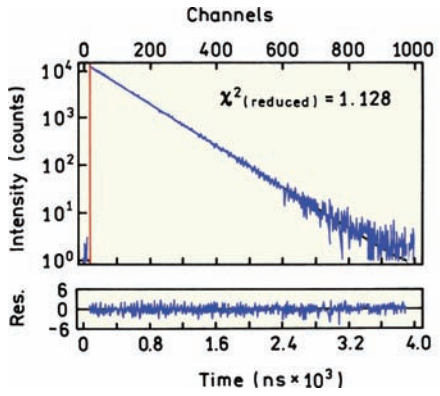

Figure 4.45. Intensity decay of $[Ru(bpy)_3]^{2+}$ measured with a photon counting multiscalar. Excitation was accomplished using a 440 nm laser diode with a repetition rate of 200 kHz. The lifetime was 373 ns. Revised from [169].

method,[178–179] Prony's method,[180] sine transforms,[181] and phase-plane methods.[182–183] These various techniques have been compared.[184] The method-of-moments (MEM) and the Laplace methods are not widely used at the current time. The maximum entropy method is newer, and is being used in a number of laboratories. The MEM is typically used to recover lifetime distributions since these can be recovered without assumptions about the shape of the distributions.

During the 1990s most studies using TCSPC made extensive use of NLLS and to a somewhat lesser extent the MEM. This emphasis was due to the biochemical and biophysical applications of TCSPC and the need to resolve complex decays. At present TCSPC is being used in analytical chemistry, cellular imaging, single molecule detection, and fluorescence correlation spectroscopy. In these applications the lifetimes are used to distinguish different fluorophores on different environments, and the number of observed photons is small. A rapid estimation of a mean lifetime is needed with the least possible observed photons. In these cases maximum likelihood methods are used (eq. 4.20). In the following sections we describe NLLS and the resolution of multi-exponential decay.

4.9.1. Assumptions of Nonlinear Least Squares

Prior to describing NLLS analysis, it is important to understand its principles and underlying assumptions. It is often stated that the goal of NLLS is to fit the data, which is only partially true. With a large enough number of variable parameters, any set of data can be fit using many different mathematical models. The goal of least squares is to test whether a given mathematical model is consistent with the data, and to determine the parameter values for that model which have the highest probability of being correct. Least squares provides the best estimate for parameter values if the data satisfy a reasonable set of assumptions, which are as follows:[185-186]

1. All the experimental uncertainty is in the dependent variable (y-axis).
2. The uncertainties in the dependent variable (measured values) have a Gaussian distribution, centered on the correct value.
3. There are no systematic errors in either the dependent (y-axis) or independent (x-axis) variables.
4. The assumed fitting function is the correct mathematical description of the system. Incorrect models yield incorrect parameters.
5. The datapoints are each independent observations.
6. There is a sufficient number of datapoints so that the parameters are overdetermined.

These assumptions are generally true for TCSPC, and least squares is an appropriate method of analysis. In many other instances the data are in a form that does not satisfy these assumptions, in which case least squares may not be the preferred method of analysis. This can occur when the variables are transformed to yield linear plots, the errors are no longer a Gaussian and/or there are also errors in the x-axis. NLLS may not be the best method of analysis when there is a small number of photon counts, such as TCSPC measurements on single molecules (Section 4.7.1). The data for TCSPC usually satisfy the assumptions of least-squares analysis.

4.9.2. Overview of Least-Squares Analysis

A least-squares analysis starts with a model that is assumed to describe the data. The goal is to test whether the model is consistent with the data and to obtain the parameter values for the model that provide the best match between the measured data, $N(t_k)$, and the calculated decay, $N_c(t_k)$, using assumed parameter values. This is accomplished by minimizing the goodness-of-fit parameter, which is given by

$$\chi^2 = \sum_{k=1}^{n} \frac{1}{\sigma_k^2} \left[N(t_k) - N_c(t_k)\right]^2$$

$$= \sum_{k=1}^{n} \frac{\left[N(t_k) - N_c(t_k)\right]^2}{N(t_k)} \qquad (4.21)$$

In this expression the sum extends over the number (n) of channels or datapoints used for a particular analysis and σ_k in the standard deviation of each datapoint.

In TCSPC it is straightforward to assign the standard deviations (σ_k). From Poisson statistics the standard deviation is known to be the square root of the number of photon counts: $\sigma_k = \sqrt{N(t_k)}$. Hence, for a channel with 10,000 counts, $\sigma_k = 100$, and for 10^6 counts, $\sigma_k = 1000$. This relationship between the standard deviation and the number of photons is only true if there are no systematic errors and counting statistics are the only source of uncertainty in the data. If the data contains only Poisson noise then the relative uncertainty in the data decreases as the number of photons increases. The value of χ^2 is the sum of the squares deviations between the measured $N(t_k)$ and expected values $N_c(t_k)$, each divided by squared deviations expected for the number of detected photons.

It is informative to compare the numerator and denominator in eq. 4.21 for a single datapoint. Assume a channel contains 10^4 counts. Then the expected deviation for this measurement is 100 counts. If the assumed model accounts for the data, then the numerator and denominator of eq. 4.21 are both $(10^2)^2$, and this datapoint contributes 1.0 to the value of χ^2. In TCSPC, and also for frequency-domain measurements, the number of datapoints is typically much larger than the number of parameters. For random errors and the correct model, χ^2 is expected to be approximately equal to the number of datapoints (channels).

Suppose the data are analyzed in terms of the multiexponential model (eq. 4.8). During NLLS analysis the values of α_i and τ_i are varied until χ^2 is a minimum, which occurs when $N(t_k)$ and $N_c(t_k)$ are most closely matched. Several mathematical methods are available for selecting how α_i and τ_i are changed after each iteration during NLLS fitting. Some procedures work more efficiently than others, but all seem to perform adequately.[185–186] These methods include the Gauss-Newton, modified Gauss-Newton, and Nelder-Mead algorithms. This procedure of fitting the data according to eq. 4.21 is frequently referred to as deconvolution, which is inaccurate. During analysis an assumed decay law $I(t)$ is convoluted with $L(t_k)$, and the results are compared with $N(t_k)$. This procedure is more correctly called iterative reconvolution.

It is not convenient to interpret the values of χ^2 because χ^2 depends on the number of datapoints.[1] The value of χ^2 will be larger for data sets with more datapoints. For this reason one uses the value of reduced χ^2:

$$\chi_R^2 = \frac{\chi^2}{n - p} = \frac{\chi^2}{\nu} \tag{4.22}$$

where n is the number of datapoints, p is the number of floating parameters, and $\nu = n - p$ is the number of degrees of freedom. For TCSPC the number of datapoints is typically much larger than the number of parameters so that $(n - p)$ is approximately equal to n. If only random errors contribute to χ_R^2, then this value is expected to be near unity. This is because the average χ^2 per datapoint should be about one, and typically the number of datapoints (n) is much larger than the number of parameters. If the model does not fit, the individual values of χ^2 and χ_R^2 are both larger than expected for random errors.

The value of χ_R^2 can be used to judge the goodness-of-fit. When the experimental uncertainties σ_k are known, then the value of χ_R^2 is expected to be close to unity. This is because each datapoint is expected to contribute σ_k^2 to χ^2, the value of which is in turn normalized by the $\Sigma\sigma_k^2$, so the ratio is expected to be near unity. If the model does not fit the data, then χ_R^2 will be significantly larger than unity. Even though the values of χ_R^2 are used to judge the fit, the first step should be a visual comparison of the data and the fitted function, and a visual examination of the residuals. The residuals are the differences between the measured data and the fitted function. If the data and fitted function are grossly mismatched there may be a flaw in the program, the program may be trapped in a local minimum far from the correct parameter values, or the model may be incorrect. When the data and fitted functions are closely but not perfectly matched, it is tempting to accept a more complex model when a simpler one is adequate. A small amount of systematic error in the data can give the appearance that the more complex model is needed. In this laboratory we rely heavily on visual comparisons. If we cannot visually see a fit is improved, then we are hesitant to accept the more complex model.

4.9.3. Meaning of the Goodness-of-Fit

During analysis of the TCSPC data there are frequently two or more fits to the data, each with a value of χ_R^2. The value of χ_R^2 will usually decrease for the model with more adjustable parameters. What elevation of χ_R^2 is adequate to reject a model? What decrease in χ_R^2 is adequate to justify accepting the model with more parameters? These questions can be answered in two ways, based on experience and based on mathematics. In mathematical terms one can

Table 4.2. χ_R^2 Distribution[a]

Probability (P)/ degrees of freedom	0.2	0.1	0.05	0.02	0.01	0.001
10	1.344	1.599	1.831	2.116	2.321	2.959
20	1.252	1.421	1.571	1.751	1.878	2.266
50	1.163	1.263	1.350	1.452	1.523	1.733
100	1.117	1.185	1.243	1.311	1.358	1.494
200	1.083[b]	1.131	1.170	1.216	1.247	1.338

[a]From [1, Table C-4].

[b]Mentioned in text.

predict the probability for obtaining a value of χ_R^2 because of random errors. These values can be found in standard mathematical tables of the χ_R^2 distribution. Selected values are shown in Table 4.2 for various probabilities and numbers of degrees of freedom. Suppose you have over 200 datapoints and the value of $\chi_R^2 = 1.25$. There is only a 1% chance ($P = 0.01$) that random errors could result in this value. Then the model yielding $\chi_R^2 = 1.25$ can be rejected, assuming the data are free of systematic errors. If the value of χ_R^2 is 1.08, then there is a 20% chance that this value is due to random deviations in the data. While this may seem like a small probability, it is not advisable to reject a model if the probability exceeds 5%, which corresponds to $\chi_R^2 = 1.17$ (Table 4.2). In our experience, systematic errors in the data can easily result in a 10–20% elevation in χ_R^2. For example, suppose the data does contain systematic errors and a two-component fit returns a value of $\chi_R^2 = 1.17$. The data are then fit to three components, which results in a decreased χ_R^2. If the three-component model is accepted as the correct model, then an incorrect conclusion is reached. The systematic errors in the data will have resulted in addition of a third component that does not exist in the experimental system.

While we stated that assumptions 1 through 6 (above) are generally true for TCSPC, we are not convinced that number 5 is true. Based on our experience we have the impression that the TCSPC data have fewer independent observations (degrees of freedom) in the TCSPC data than the number of actual observations (channels). This is not a criticism of NLLS analysis or TCSPC. However, if the effective number of independent datapoints is less than the number of datapoints, then small changes in χ_R^2 may not be as significant as understood from the mathematical tables.

Complete reliance on mathematical tables can lead to overinterpretation of the data. The absolute value of χ_R^2 is often of less significance than its relative values. Systematic errors in the data can easily result in χ_R^2 values in excess of 1.5. This small elevation in χ_R^2 does not mean the model is incorrect. We find that for systematic errors the χ_R^2 value is not significantly decreased using the next more complex model. Hence, if the value of χ_R^2 does not decrease significantly when the data are analyzed with a more complex model, the value of χ_R^2 probably reflects the poor quality of the data. In general we consider decreases in χ_R^2 significant if the ratio decreases by twofold or more. Smaller changes in χ_R^2 are interpreted with caution, typically based on some prior understanding of the system.

4.9.4. Autocorrelation Function **Advanced Topic**

Another diagnostic for the goodness of fit is the autocorrelation function.[3] For a correct model, and the absence of systematic errors, the deviations are expected to be randomly distributed around zero. The randomness of the deviations can be judged from the autocorrelation function. Calculation of the correlation function is moderately complex, and does not need to be understood in detail to interpret these plots. The autocorrelation function $C(t_j)$ is the extent of correlation between deviations in the k and $k+j$th channel. The values of $C(t_j)$ are calculated using

$$C(t_j) = \left(\frac{1}{m}\sum_{k=1}^{m} D_k D_{k+j}\right) \Big/ \left(\frac{1}{n}\sum_{k=1}^{n} D_k^2\right) \qquad (4.23)$$

where D_k is the deviation in the kth datapoint and D_{k+j} is the deviation in the $k+j$th datapoint (eq. 4.23). This function measures whether a deviation at one datapoint (time channel) predicts that the deviation in the jth higher channel will have the same or opposite sign. For example, the probability is higher that channels 50 and 51 have the same sign than channels 50 and 251. The calculation is usually extended to test for correlations across half of the data channels ($m = n/2$) because the order of multiplication in

the numerator does not matter. The autocorrelation plots have half as many datapoints as the original data set.

One example of an autocorrelation plot was seen in Figure 4.27, where data for NATA were presented for measurements versus scattered light and versus a lifetime reference. This instrument showed a minor color effect, which resulted in some systematic deviations between $N_c(t_k)$ and $N(t_k)$. The systematic differences are barely visible in the direct plot of the deviations (middle left). The autocorrelation plot (upper left) allowed the deviations to be visualized as positive and negative correlations in adjacent or distant channels, respectively. For closely spaced channels the deviations are likely to both be the same sign. For more distant channels the deviations are likely to be of opposite signs. These systematic errors were eliminated by the use of a lifetime reference, as seen by the flat autocorrelation plot (upper right panel).

4.10. ANALYSIS OF MULTI-EXPONENTIAL DECAYS

4.10.1. p-Terphenyl and Indole: Two Widely Spaced Lifetimes

An understanding of time-domain data analysis is facilitated by examination of representative data. As an example we chose a mixture of p-terphenyl and indole, which individually display single exponential decays of 0.93 and 3.58 ns, respectively. For the time-domain measurements a mixture of p-terphenyl and indole was observed at 330 nm, where both species emit (Figure 4.46). TCSPC data for this mixture are shown in Figure 4.47. The presence of two decay times is evident from curvature in the plot of log $N(t)$ versus time. The time-dependent data could not be fit to a single decay time, as seen by the mismatch of the calculated convolution integral (dashed) with the data (dots).

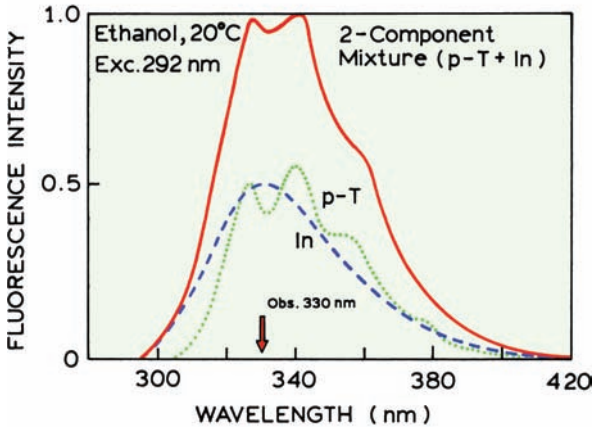

Figure 4.46. Emission spectra of p-terphenyl (p-T), indole (In) and of the mixture. Excitation was at 292 nm, from a frequency-doubled R6G dye laser. The emission at 330 nm was isolated with a monochromator. From [187].

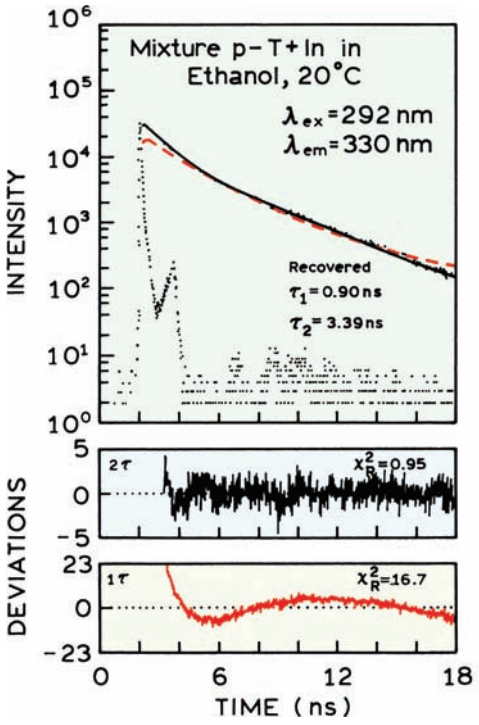

Figure 4.47. Time-domain intensity decay of a two-component mixture of indole and p-terphenyl. The dashed line shows the one-decay-time fit, and the solid line the two-decay-time fit. From [187].

The lower panels show the deviations (D_k) or differences between the measured and calculated data:

$$D_k = \frac{I(t_k) - I_c(t_k)}{\sqrt{I(t_k)}} \tag{4.24}$$

The weighted residual (W.Res.) or deviations plots are used because it is easier to see the differences between $I(t_k)$ and $I_c(t_k)$ in these plots than in a plot of log $I(t_k)$ versus t_k. Also, the residuals are weighted according to the standard deviation of each datapoint. For a good fit these values are expected to randomly distribute around zero, with a mean value near unity.

4.10.2. Comparison of χ_R^2 Values: *F* Statistic

How can one compare the values of χ_R^2 for two fits? This can be done using the *F* statistic, which is a ratio of χ_R^2 val-

Table 4.3. *F* Statistic for Comparison of χ_R^2 Values[a]

Degrees of freedom (ν)	Probability (*P*)					
	0.32	0.25	0.10	0.05	0.025	0.01
10	1.36	1.55	2.32	2.98	3.96	4.85
15	1.28	1.43	1.97	2.40	2.86	3.52
20	1.24	1.36	1.79	2.12	2.46	2.94
40	1.16	1.24	1.51	1.69	1.88	2.11
60	1.13	1.19	1.40	1.53	1.67	1.84
120	1.09	1.13	1.26	1.35	1.43	1.53
∞	1.00	1.00	1.00	1.00	1.00	1.00

[a]From [188, Table A-4]. In general, the *F* values are computed for different degrees of freedom for each χ_R^2 value. For TCSPC data and for FD data, the degrees of freedom are usually similar in the numerator and in the denominator. Hence, *F* values are listed for only one value of ν. Additional *F* values can be found in [1, Tables C-6 and C-7].

ues. This ratio depends on the number of degrees of freedom (ν) for each fit, and this number will depend on the model. The values of the χ_R^2 ratios that are statistically significant at various levels of probability are available in statistical tables, of which a few values are listed in Table 4.3. In practice, there are usually many more datapoints than parameters, so that ν is almost the same for both fits. For this reason we did not consider the slightly different number of degrees of freedom in the numerator and denominator.

For the mixture of p-terphenyl and indole the residuals of the single-decay-time fit oscillate across the time axis, which is characteristic of an incorrect model. The value of $\chi_R^2 = 16.7$ is obviously much greater than unity, and according to Table 4.2 there is a less than 0.1% chance that random error could result in such an elevated value of χ_R^2. Additionally, the χ_R^2 ratio of 17.6 is much larger than the values of the *F* statistic in Table 4.3. Hence, the single-decay-time model is easily rejected for this sample. There is a potential problem with the use of an *F* statistic to compare two χ_R^2 values originating from different mathematical models and the same data set.[189] The use of the *F* statistic requires that the residuals for each analysis be independent from each other. It is not clear if this assumption is correct when analyzing the same set of data with different mathematical models.

4.10.3. Parameter Uncertainty: Confidence Intervals

The NLLS analysis using the multi-exponential model returns a set of α_i and τ_i values. It is important to recognize that there can be considerable uncertainty in these values, particularly for closely spaced decay times. Estimation of the uncertainties in the recovered parameters is an important but often-ignored problem. With nonlinear least-squares analysis there are no general methods for estimating the range of parameter values that are consistent with the data. Uncertainties are reported by almost all the data analysis programs, but these estimates are invariably smaller than the actual uncertainties. Most software for nonlinear least-square analysis reports uncertainties that are based on the assumption of no correlation between parameters. These are called the asymptotic standard errors (ASEs).[185] As shown below for a mixture having more closely spaced lifetimes (Section 4.10.5), the errors in the recovered parameters often exceed the ASEs. The ASEs usually underestimate the actual uncertainties in the parameter values.

In our opinion the best way to determine the range of parameters consistent with the data is to examine the χ_R^2 surfaces, which is also called a support plane analysis.[186] The procedure is to change one parameter value from its value where χ_R^2 is a minimum, and then rerun the least-squares fit, keeping this parameter value constant at the selected value. By rerunning the fit, the other parameters can adjust to again minimize χ_R^2. If χ_R^2 can be reduced to an acceptable value, then the offset parameter value is said to be consistent with the data. The parameter value is changed again by a larger amount until the χ_R^2 value exceeds an acceptable value, as judged by the F_χ statistic (eq. 4.25) appropriate for *p* and ν degrees of freedom.[190] This procedure is then repeated for the other parameter values.

The range of parameter values consistent with the data can be obtained using $P = 0.32$, where *P* is the probability that the value of F_χ is due to random errors in the data. When the value of *P* exceeds 0.32 there is less than a 32%

chance that the parameter value is consistent with the data. When the value of P is less than 0.32 there is a 68% chance that the parameter value is consistent with the data, which is the usual definition of a standard deviation.

To determine the confidence interval, the value of χ_R^2 with a fixed parameter value, χ_R^2(par), is compared with the minimum value of χ_R^2 with all parameter variables, χ_R^2(min).[190–191] The range of parameter values is expanded until χ_R^2(par) exceeds the F_χ value for the number of parameters (p) and the degrees of freedom (ν) and the chosen probability, typically $P = 0.32$:

$$F_\chi = \frac{\chi_R^2(\text{par})}{\chi_R^2(\text{min})} = 1 + \frac{p}{\nu} F(p,\nu,P) \qquad (4.25)$$

In this expression[192] $F(p,\nu,P)$ is the F statistic with p parameters and ν degrees of freedom with a probability of P. The F statistics needed to calculate F_χ are listed in Table 4.4. It is important to realize that, in general, the uncertainty range will not be symmetrical around the best fit value of the parameter. For a two-decay-time model ($p = 4$) and 400 degrees of freedom ($\nu = 400$), the F_χ value is 1.012 for $p = 0.32$. Calculation of the χ_R^2 surfaces is a time-consuming process, and has not yet been automated within most data-analysis software. However, these calculations provide a realistic judgment of what one actually knows from the data.

There appears to be no general agreement that the procedure described above represents the correct method to estimate confidence intervals. This is a topic that requires further research. There is some disagreement in the statistics literature about the proper form of F_χ for estimating the parameter uncertainty.[189] Some reports[193] argue that, since one parameter is being varied, the number of degrees of freedom in the numerator should be one. In this case F_χ is calculated using

$$F_\chi = \frac{\chi^2(\text{par})}{\chi^2(\text{min})} = 1 + \frac{1}{\nu} F(p,\nu,P) \qquad (4.26)$$

Since we are varying p parameters to calculate the χ_R^2 surface, we chose to use eq. 4.25. Irrespective of whether the F_χ values accurately define the confidence interval, examination of the χ_R^2 surfaces provides valuable insight into the resolution of parameters provided by a given experiment. If the χ_R^2 surfaces do not show well-defined minima, then the data are not adequate to determine the parameters.

A confidence interval analysis is shown in Figure 4.48 for the mixture of p-terphenyl and indole. The confidence intervals are given by the intercept of the χ_R^2 surfaces (solid) with the appropriate F_χ values (dashed). For comparison we have also shown the ASEs as solid bars. The ASEs are about twofold smaller than the confidence intervals. This is a serious underestimation, but a factor of two is small compared to what is found for more closely spaced lifetimes. Also, in our opinion, the F_χ value near 1.005 for about 950 degrees of freedom is an underestimation because the time-resolved decay may not have completely independent datapoints. Suppose the actual number of independent datapoints was 200. In this case the F_χ value would be near 1.02, which may provide a more realistic range of the uncertainties. For instance, the confidence interval of α_2 would become 0.305 ± 0.015 instead of 0.305 ± 0.005. The uncertainty in the latter value appears to be unrealistically small.

Another way to estimate parameter uncertainty is by Monte Carlo simulations.[194] The basic idea is to simulate data based on the recovered decay law using the known level of random noise present in a given experiment. Newly generated random noise is added to each simulated data set, which is then analyzed as if it were actual data. New random noise is added and the process repeated. This results in a histogram of parameter values. These parameter values are examined for the range that results from the randomly added noise. It is important that the simulations use a model that correctly describes the system. The Monte Carlo method is time consuming and thus seldom used. However, with the rapid advances in computer speed, one can expect Monte Carlo simulations to become more widely utilized for estimation of confidence intervals.

4.10.4. Effect of the Number of Photon Counts

For a single-exponential decay, the decay time can usually be determined with adequate accuracy even for a small number of observed photons. However, for multi-exponential decays it is important to measure as many photons as possible to obtain the highest resolution of the parameter values. This is illustrated in Figure 4.49 for the same two-component mixture of p-terphenyl and indole. For these data the number of counts in the peak channel was tenfold less than in Figure 4.47, 3,000 counts versus 30,000 counts. The correct values for the two decay times were still recovered. However, the relative decrease in χ_R^2 for the two decay time models was only 1.9-fold, as compared to 17-

Table 4.4. *F* Statistic for Calculation of Confidence Intervals[a]

Degrees of freedom (ν)	Probability (*P*)					
	One parameter (*p*)[b]					
	0.32[d]	0.25	0.10	0.05	0.025	0.01
10	1.09	1.49	3.29	4.96	6.94	10.0
30	1.02	1.38	2.88	4.17	5.57	7.56
60	1.01	1.35	2.79	4.00	5.29	7.08
120	1.00	1.34	2.75	3.92	5.15	6.85
∞	1.00	1.32	2.71[c]	3.84	5.02	6.63
	Two Parameters[b]					
10	1.28	1.60	2.92	4.10	5.46	7.56
30	1.18	1.45	2.49	3.32	4.18	5.39
60	1.16	1.42	2.39	3.15	3.93	4.98
120	1.15	1.40	2.35	3.07	3.80	4.79
∞	1.14	1.39	2.30	3.00	3.69	4.61
	Three Parameters					
10	1.33	1.60	2.73	3.71	4.83	6.55
30	1.22	1.44	2.28	2.92	3.59	4.51
60	1.19	1.41	2.18	2.76	3.34	4.13
120	1.18	1.39	2.13	2.68	3.23	3.95
∞	1.17	1.37	2.08	2.60	3.12	3.78
	Four Parameters					
10	1.34	1.59	2.61	3.48	4.47	5.99
30	1.23	1.42	2.14	2.64	3.25	4.02
60	1.20	1.38	2.04	2.53	3.01	3.65
120	1.19	1.37	1.99	2.45	2.89	3.48
∞	1.18	1.35	1.94	2.37	2.79	3.32
	Five Parameters					
10	1.35	1.59	2.52	3.33	4.24	5.64
30	1.23	1.41	2.05	2.53	3.03	3.70
60	1.20	1.37	1.95	2.37	2.79	3.34
120	1.19	1.35	1.90	2.29	2.67	3.17
∞	1.17	1.33	1.85	2.21	2.57	3.02
	Eight Parameters					
10	1.36	1.56	2.34	3.07	3.85	5.06
30	1.22	1.37	1.88	2.27	2.65	3.17
60	1.19	1.32	1.77	2.10	2.41	2.82
120	1.17	1.30	1.72	2.02	2.30	2.66
∞	1.16	1.28	1.67	1.94	2.19	2.51
	Ten Parameters					
10	1.35	1.55	2.32	2.98	3.72	4.85
30	1.22	1.35	1.82	2.16	2.51	2.98
60	1.18	1.30	1.71	1.99	2.27	2.63
120	1.17	1.28	1.65	1.91	2.16	2.47
∞	1.15	1.25	1.59	1.83	2.05	2.32

[a]From [188]. In the ratio of χ_R^2 values, the degrees of freedom refer to that for the denominator. The degrees of freedom in the numerator are one, two, or three, for one, two or three additional parameters.

[b]These values refer to the degrees of freedom in the numerator (*p*).

[c]This value appears to be incorrect in [188], and was taken from [1].

[d]The values for 0.32 were calculated with a program (F-stat) provided by Dr. M. L. Johnson, University of Virginia.

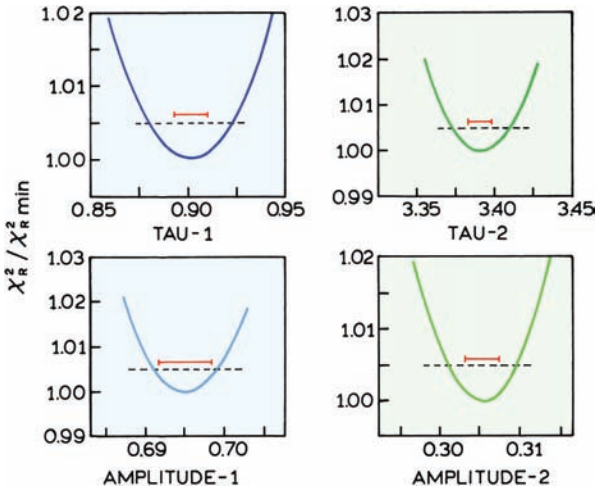

Figure 4.48. Confidence interval for the two component mixture of indole and p-terphenyl. The solid bars show the asymptotic standard errors. From [187].

fold for the higher number of counts. Also, the χ_R^2 surfaces rise more slowly as the lifetimes are varied (Figure 4.49, right), so that the lifetimes are determined with less precision.

4.10.5. Anthranilic Acid and 2-Aminopurine: Two Closely Spaced Lifetimes

The resolution of two decay times becomes more difficult if the decay times are more closely spaced. This is illustrated by a mixture of anthranilic acid (AA) and 2-amino purine

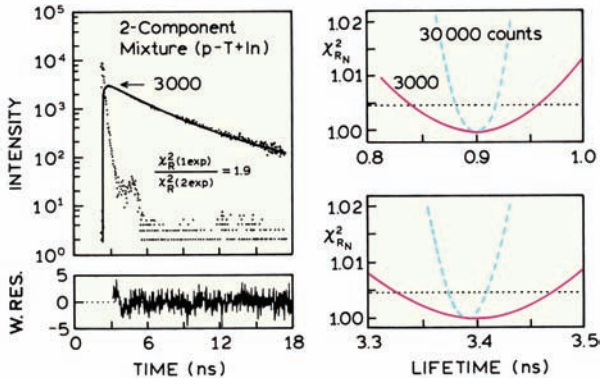

Figure 4.49. Effect of the number of photons counts on the resolution of the lifetimes for the mixture of p-terphenyl (p-T) and indole (In) in Figure 4.47. **Left**: Two-decay-time fit of the intensity decay measured with 3000 counts in the peak channel. The corresponding plot for the data obtained with 30,000 counts in the peak channel is shown in Figure 4.31. **Right**: Comparison of the χ_R^2 surfaces for the data obtained with 3000 (——) and 30,000 counts (dashed). From [187].

(2-AP), which individually display single exponential decays of 8.53 and 11.27 ns, respectively (shown in Figure 4.54 below). Emission spectra for the mixture are shown in Problem 4.5. The time-dependent data for the mixture of AA and 2-AP are shown in Figure 4.50. At 380 nm, where both fluorophores emit, it is difficult to visually detect the presence of two decay times. The single-decay-time model (dashes) shows only small differences from the data (dots). However, the residual plot shows systematic deviations (lower panel), which are easier to see on the linear scale used for the deviations than on the logarithmic plot. The 4.5-fold decrease in χ_R^2 for the two-decay-time model is adequate to reject the single-decay-time model.

While the data support acceptance of two decay times, these values of α_i and τ_i are not well determined. This is illustrated in Figure 4.51, which shows the χ_R^2 surfaces for the mixture of AA and 2-AP. This mixture was measured at five emission wavelengths. The data were analyzed individually at each wavelength. Each of the χ_R^2 surfaces shows distinct minima, which leads one to accept the recovered lifetimes. However, one should notice that different life-

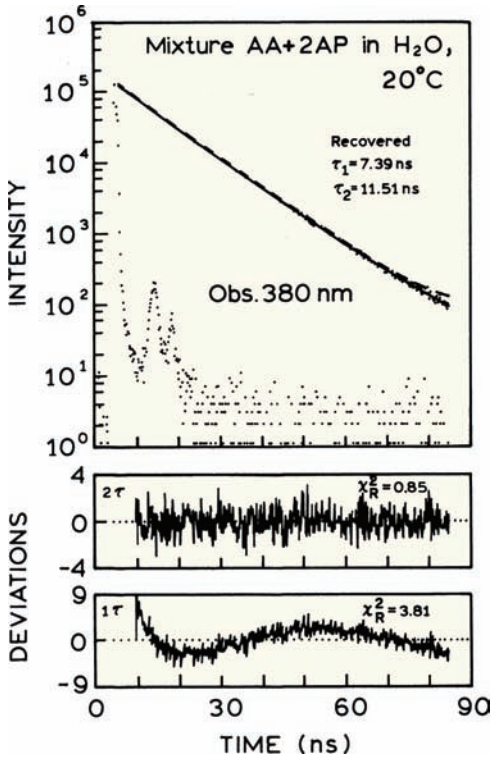

Figure 4.50. Time-dependent intensity decay of a two-component mixture of anthranilic acid (AA) and 2-amino-purine (2-AP). The dashed line shows the one-decay-time fit, and the solid line the two-decay-time fit to the data (dots). From [187].

Table 4.5. Resolution of a Two-Component Mixture of Anthranilic Acid and 2-Aminopurine, Observed at a Single Wavelength, Using Time-Domain Data

Observation wavelength (nm)	Lifetimes (ns)		Pre-exponential factors		Fractional intensities		χ_R^2 Number of decay times	
	τ_1	τ_2	α_1	α_2	f_1	f_2	2[a]	1[a]
360	6.72	11.58	0.223	0.777	0.143	0.857	1.01	2.77
380	7.51	11.51	0.404	0.596	0.306	0.694	0.85	3.81
400	7.22	11.08	0.448	0.552	0.347	0.653	0.91	4.51
420	7.99	11.22	0.595	0.405	0.511	0.489	0.93	2.95
440	8.38	11.91	0.763	0.237	0.692	0.308	0.89	2.72

[a]Refers to a two- or one-component fit.

times were recovered at each emission wavelength. This suggests that the actual uncertainties in the recovered lifetimes are larger than expected from the ASEs, and then seem to be even larger than calculated from the χ_R^2 surfaces. Furthermore, the differences in the lifetimes recovered at each emission wavelength seem to be larger than expected even from the χ_R^2 surfaces. This illustrates the difficulties in recovering accurate lifetimes if the values differ by less than twofold.

Another difficulty is that the recovered amplitudes do not follow the emission spectra expected for each component (Table 4.5 and Problem 4.5). As the lifetimes become closer together, the parameter values become more highly correlated, and it is difficult to know the true uncertainties. This is not intended to be a criticism of the TD measurements, but rather is meant to illustrate the difficulties inherent in the analysis of multi-exponential decays.

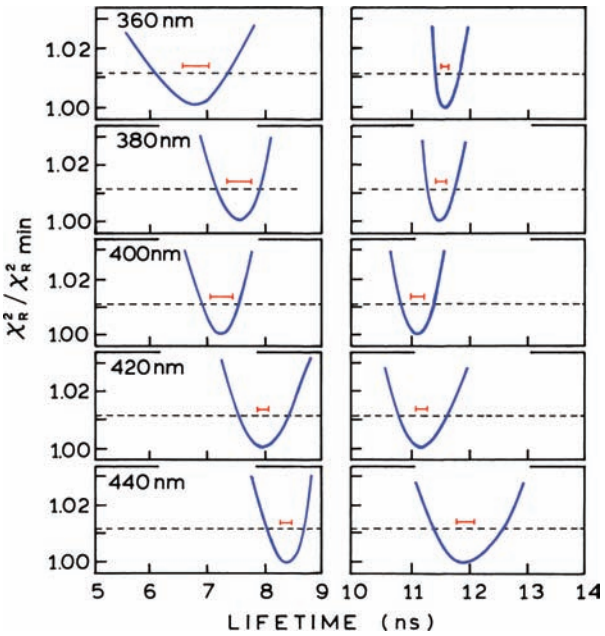

Figure 4.51. Lifetime χ_R^2 surfaces for the two-component mixture of AA and 2-AP (Figure 4.50). The horizontal bars show the asymptotic standard errors. From [187].

4.10.6. Global Analysis: Multi-Wavelength Measurements

One way to improve the resolution of closely spaced lifetimes is to perform measurements at additional wavelengths, and to do a global analysis (Section 4.12). The concept of global analysis is based on the assumption that decay times are independent of wavelength. The decay times are global parameters because they are the same in all data sets. The amplitudes are non-global because they are different in each data set. Global analysis of the multi-wavelength data results in much steeper χ_R^2 surfaces (Figure 4.52), and presumably a higher probability of recovery of the correct lifetimes. The lifetimes are determined with higher certainty from the global analysis because of the steeper χ_R^2 surfaces and the lower value of F_χ with more degrees of freedom (more data). As shown in Problem 4.5, the amplitudes (Table 4.6) recovered from the global analysis more closely reflect the individual emission spectra than the amplitudes recovered from the single wavelength data.

4.10.7. Resolution of Three Closely Spaced Lifetimes

The resolution of multi-exponential decays becomes more difficult as the number of decay times increases. This difficulty is illustrated by a mixture of indole (In), anthranilic acid (AA), and 2-amino purine (2-AP) (Figure 4.53). At 380 nm all three fluorophores emit, and the decay is expected to be a sum of three exponentials.

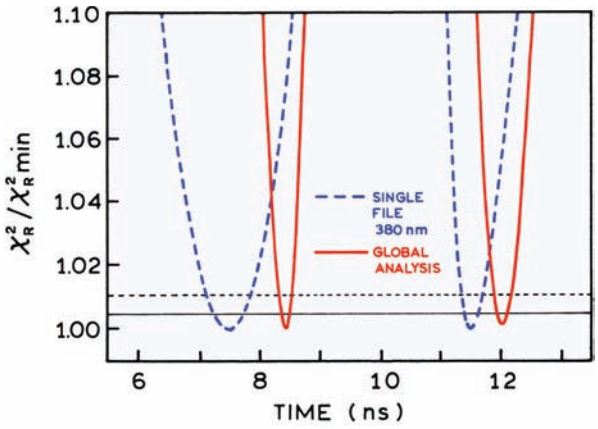

Figure 4.52. Lifetime χ_R^2 surface for the global analysis of the two component mixture of AA and 2-AP (——). Also shown for comparison is the χ_R^2 surface at 380 nm (dashed). The horizontal lines represent the F_χ values. From [187].

Table 4.6. Global Analysis of a Two-Component Mixture of Anthranilic Acid and 2-Aminopurine Measured at Five Emission Wavelengths: Time Domain Data

Observation wavelength (nm)	AA[a] τ_1 = 8.35 ns		2-AP τ_2 = 12.16 ns	
	α_1	f_1	α_2	f_2
360	0.117	0.089	0.883	0.911
380	0.431	0.357	0.569	0.643
400	0.604	0.528	0.396	0.472
420	0.708	0.640	0.292	0.360
440	0.810	0.758	0.190	0.242

[a]For the two-component fit χ_R^2 = 0.92, and for the one-component fit χ_R^2 = 22.3.

TCSPC data for the three individual fluorophores are shown in Figure 4.54. Excitation was with the frequency-doubled output of an R6G dye laser, and the emission detected with an R2809 MCP PMT. The excitation was polarized vertically and the emission detected 54.7° from vertical to avoid the effects of rotational diffusion on the measured intensity decays. The points represent the data $I(t_k)$ or number of counts measured at each time interval t_k. The solid lines are the fitted functions or calculated data $I_c(t_k)$ using a single decay time. $I(t_k)$ and $I_c(t_k)$ are well matched, which indicates that each individual fluorophore decays as a single exponential with decay times of 4.41, 8.53, and 11.27 ns, respectively. As expected for a good fit,

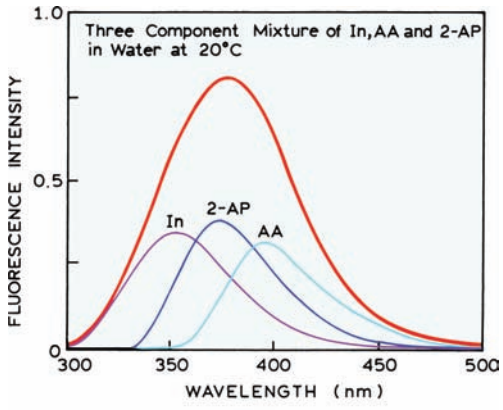

Figure 4.53. Emission spectra of Indole (In), 2-aminopurine (2-AP), and anthranilic acid (AA), and of the three-component mixture. From [187].

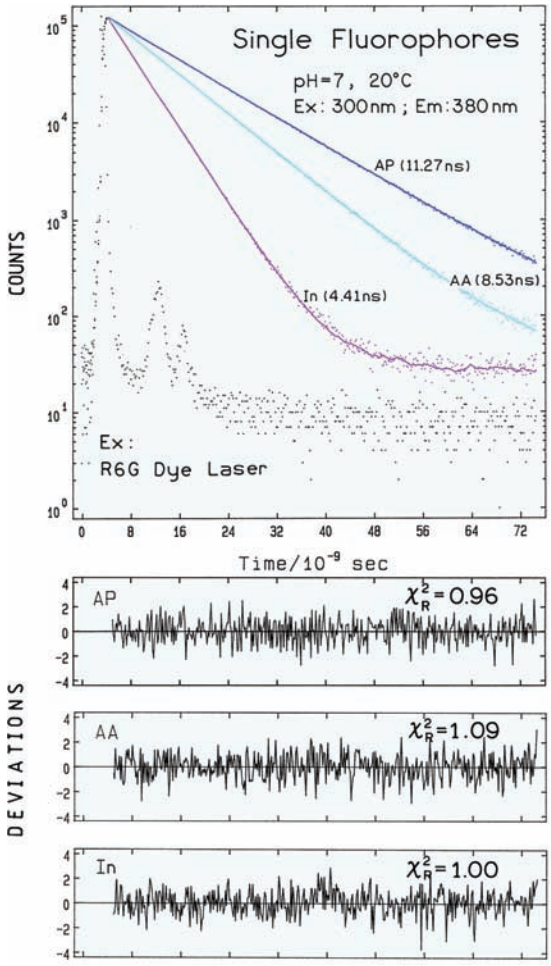

Figure 4.54. TCSPC data for indole (In), anthranilic acid (AA), and 2-aminopurine (AP). From [187].

the deviations are randomly distributed around zero and the values of χ_R^2 are near unity.

The intensity decay for indole in Figure 4.54 illustrates the need to consider the convolution integral when using an MCP PMT, even with a 4.41-ns decay time. At long times the plot of log $I(t_k)$ versus time becomes nonlinear even though there is only a single lifetime. This effect is most visible for indole, with the shortest lifetime of 4.41 ns. This long tail on the intensity decay is due to continued excitation from the tail of the impulse response function and possibly some background emission. If one did not consider convolution, and calculated the decay times only from the slopes, then one would reach the erroneous conclusion that the indole sample displayed a second long decay time.

Now consider similar data for a mixture of the three fluorophores. The decay times range threefold from 4 to 12 ns, but this is a difficult resolution. Examination of Figure 4.55 shows that the single exponential fit (dashes) appears to provide a reasonable fit to the data. However, the failure of this model is easily seen in the deviations, which are much larger than unity and not randomly distributed on the time axis (lowest panel). The failure of the single exponential model can also be seen from the value of $\chi_R^2 = 26.45$, which according to Table 4.2 allows the single exponential model to be rejected with high certainty. To be more specific, there is a less than a 0.1% chance ($P < 0.001$) that this value of χ_R^2 could be the result of random error in the data.

The situation is less clear with a double exponential fit. In this case the fitted curve overlaps the data (not shown), $\chi_R^2 = 1.22$, and the deviations are nearly random. According to the χ_R^2 data (Table 4.2), there is only a 2% chance that $\chi_R^2 = 1.22$ could result from statistical uncertainties in the data. In practice, such values of χ_R^2 are often encountered owing to systematic errors in the data. For comparison, the systematic errors in Figure 4.27 resulted in an elevation of χ_R^2 to a similar value. In an actual experiment we do not know beforehand if the decay is a double, triple, or non-exponential decay. One should always accept the simplest model that accounts for the data, so we would be tempted to accept the double exponential model because of the weak evidence for the third decay time.

An improved fit was obtained using the triple exponential model, $\chi_R^2 = 0.93$, and the deviations are slightly more random than the two-decay-time fit. It is important to understand that such a result indicates the data are consistent with three decay times, but does not prove the decay is a triple exponential. By least-squares analysis one cannot exclude other more complex models, and can only state that a particular model is adequate to explain the data. In this case, the data are consistent with the three-exponential model, but the analysis does not exclude the presence of a fourth decay time.

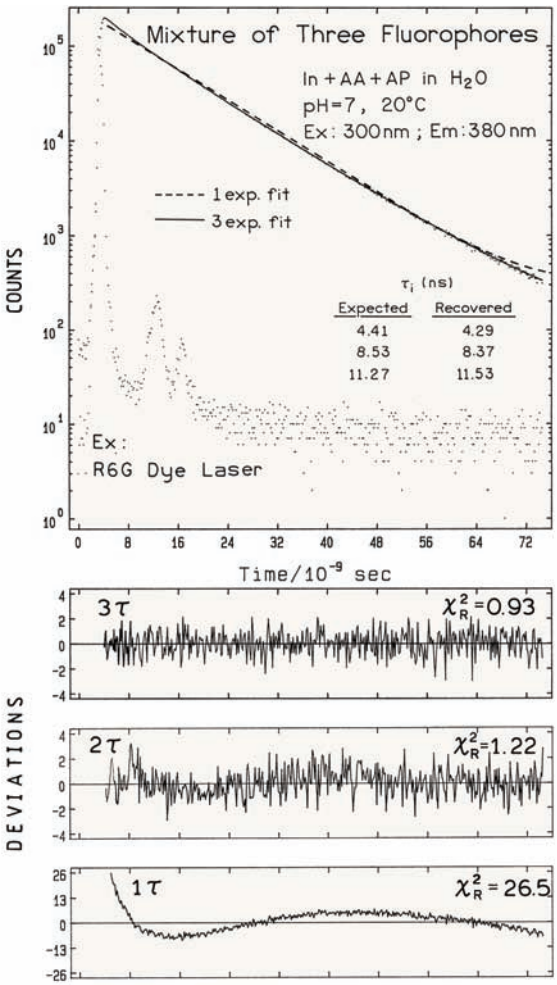

Figure 4.55. TCSPC data for a mixture of indole (In), anthranilic acid (AA), and 2-aminopurine (AP). From [187].

The two- and three-decay-time fits can also be compared using the ratio of χ_R^2 values. For this mixture the ratio of χ_R^2 values was 1.31. This value can be compared with the probability of this ratio occurring due to random deviations in the data, which is between 5 and 10% (Table 4.3). Hence, there is a relatively low probability of finding this reduction in χ_R^2 (1.22 to 0.93) unless the data actually contained three decay times, or was described by some model other than a two-decay-time model. Stated alternatively, there is a 90 to 95% probability that the two-decay-time model is not an adequate description of the sample.

Table 4.7. Multi-Exponential Analysis of the Three-Component Mixture of Indole, 2-Aminopurine, and Anthranilic Acid

Observation wavelength (nm)	Lifetimes (ns)			Pre-exponential factors			Fractional intensities[a]			χ_R^2, number of exponents		
	τ_1	τ_2	τ_3	α_1	α_2	α_3	f_1	f_2	f_3	3	2	1
360	4.79 (0.10)[b]	7.51 (1.66)	11.43 (0.02)	0.314	0.004	0.682	0.161 (0.001)	0.003 (0.001)	0.836	1.10	1.10	17.67
380	4.29 (0.33)	8.37 (0.05)	11.53 (0.02)	0.155	0.622	0.223	0.079 (0.001)	0.617 (0.001)	0.304	0.93	1.22	26.45
400	4.99 (0.16)	9.50 (0.13)	13.48 (0.25)	0.180	0.722	0.098	0.099 (0.001)	0.755 (0.001)	0.146	0.96	0.97	7.88
420	4.32 (0.47)	8.54 (0.25)	11.68 (0.09)	0.072	0.658	0.270	0.034 (0.001)	0.618 (0.001)	0.348	0.93	0.34	4.97
440	1.70 (0.61)	7.94 (0.24)	11.07 (0.06)	0.037	0.580	0.383	0.007 (0.001)	0.517 (0.001)	0.476	1.02	1.04	4.14

[a] $f_i = \alpha_i\tau_i/\Sigma\alpha_j\tau_j$.
[b] Asymptotic standard errors.

One may question why there are two tests for goodness of fit: based on χ_R^2 itself and based on the F statistic. The values of χ_R^2 are useful when the experimental errors can be accurately estimated, which is usually the case with TCSPC data. In this case the value of χ_R^2 provides a test of both the agreement of the measured and calculated $N(t_k)$ values, and whether the only source of noise is Poisson photon statistics. In contrast to χ_R^2, the F statistic can be used when the experimental uncertainties (σ_k values) are not precisely known. This is usually the case with stroboscopic, gated detection, and streak camera measurements, in which photon counting is not used. This situation also occurs in frequency-domain fluorometry, where the uncertainties in the phase and modulation values can only be estimated. The calculated values of χ_R^2 can be very different from unity even for a good fit, because the σ_k^2 values may not be equal to the values of $[N(t_k) - N_c(t_k)]^2$. This is not a problem as long as the relative values of χ_R^2 are known. In these cases one uses the F statistic, or relative decrease in χ_R^2, to determine the goodness of fit.

For closely spaced lifetimes, the ASEs will greatly underestimate the uncertainties in the parameters. This underestimation of errors is also illustrated in Table 4.7, which lists the analysis of the three-component mixture when measured at various emission wavelengths. It is clear from these analyses that the recovered lifetimes differ by amounts considerably larger than the asymptotic standard errors. This is particularly true for the fractional intensities, for which the asymptotic standard errors are ±0.001. Similar results can be expected for any decay with closely spaced lifetimes.

4.11. INTENSITY DECAY LAWS

So far we have considered methods to measure intensity decays, but we have not considered the forms that are possible. Many examples will be seen in the remainder of this book. A few examples are given here to illustrate the range of possibilities.

4.11.1. Multi-Exponential Decays

In the multi-exponential model the intensity is assumed to decay as the sum of individual single exponential decays:

$$I(t) = \sum_{i=1}^{n} \alpha_i \exp(-t/\tau_i) \tag{4.27}$$

In this expression τ_i are the decay times, α_i represent the amplitudes of the components at $t = 0$, and n is the number of decay times. This is the most commonly used model, but the meaning of the parameters (α_i and τ_i) depends on the system being studied. The most obvious application is to a mixture of fluorophores, each displaying one of the decay times τ_i. In a multi-tryptophan protein the decay times may be assigned to each of the tryptophan residue, but this usually requires examination of mutant protein with some of the tryptophan residues deleted. Many samples that contain

only a single fluorophore display decays more complex than a single exponential. These data are usually interpreted in terms of eq. 4.27, which then requires explanation of the multiple decay times. If the probe can exist in two environments, such as exposed and shielded from water, then a decay time can be assigned to each of these states. Hence, single-tryptophan proteins that exist in multiple conformational states may display a decay time for each state. Papers on protein fluorescence sometimes interpret the multi-exponential decays in terms of conformational distributions.[195–196]

The meaning of the pre-exponential factors α_i are different for a mixture of fluorophores and for one fluorophore displaying a complex decay. For the latter case, it is generally safe to assume that the fluorophore has the same radiative decay rate in each environment. In this case the α_i values represent the fraction of the molecules in each conformation at $t = 0$, which represents the ground-state equilibrium. However, the meaning of the α_i values is more complex for a mixture of fluorophores. In this case the relative α_i values depend on the concentrations, absorption, quantum yields, and intensities of each fluorophore at the observation wavelength.

Irrespective of whether the multi-exponential decay originates with a single fluorophore or multiple fluorophores, the value of α_i and τ_i can be used to determine the fractional contribution (f_i) of each decay time to the steady-state intensity. These values are given by

$$f_i = \frac{\alpha_i \tau_i}{\sum_j \alpha_j \tau_j} \tag{4.28}$$

The terms $\alpha_i\tau_i$ are proportional to the area under the decay curve for each decay time. In a steady-state measurement one measures all the emissions irrespective of when the photon is emitted. This is why the intensity is usually weaker for a short decay time and the $\alpha_i\tau_i$ product is smaller. For a mixture of fluorophores, the values of f_i represent the fractional intensity of each fluorophore at each observation wavelength (Tables 4.5 and 4.6). However, the recovered values of f_i may not correlate well with the expected intensities due to the difficulties of resolving a multi-exponential decay.

What are the variable parameters in a multi-exponential analysis? Typically these are the n lifetimes, and n or $n - 1$ amplitudes. In most intensity decay analyses the total intensity is not measured, and the $\Sigma\alpha_i$ is normalized to unity. Also, Σf_i is normalized to unity. Hence for a three-decay-time fit there are typically five independently variable parameters, three lifetimes, and two amplitudes. However, most programs require that all the amplitudes remain variable during the fitting procedure, and the α_i values are normalized at the end of the analysis. In these cases one is fitting to the total intensity, and there are three variable-amplitude parameters.

And, finally, it is important to remember that the multi-exponential model (eq. 4.27) is perhaps the most powerful model. Almost any intensity decay, irrespective of its complexity, can be fit using eq. 4.27. This means that one can say the data are consistent with eq. 4.27, but the data can also be consistent with many other decay laws.

When using the multi-exponential decay law it is often useful to determine the average lifetime ($\bar{\tau}$). The average lifetime is given by eq. 4.3. For a two-exponential decay it is given by

$$\bar{\tau} = \frac{\alpha_1\tau_1^2 + \alpha_2\tau_2^2}{\alpha_1\tau_1 + \alpha_2\tau_2} = f_1\tau_1 + f_2\tau_2 \tag{4.29}$$

Occasionally one finds the "average lifetime" given by

$$\langle\tau\rangle = \sum_i \alpha_i\tau_i \tag{4.30}$$

which is not correct. The value of $\langle\tau\rangle$ is proportional to the area under the decay curve, and for a double-exponential decay becomes

$$\int_0^\infty I(t)\,dt = \alpha_1\tau_1 + \alpha_2\tau_2 \tag{4.31}$$

This value should perhaps be called a lifetime-weighted quantum yield or an amplitude-weighted lifetime. There are occasions where the value of $\langle\tau\rangle$ is useful. For instance, the efficiency of energy transfer is given by

$$E = 1 - \frac{F_{DA}}{F_D} = 1 - \frac{\int I_{DA}(t)\,dt}{\int I_D(t)\,dt} \tag{4.32}$$

where $I_{DA}(t)$ and $I_D(t)$ are the intensity decays of the donor in the presence and absence of energy transfer, respectively. The integrals in eq. 4.32 are proportional to the steady-state intensities in the presence (F_{DA}) and absence (F_D) of

acceptor, which is given by eq. 4.31. When using the results of a multi-exponential analysis, the transfer efficiency should be calculated using <τ> values, since these are proportional to the steady-state intensity.

4.11.2. Lifetime Distributions

There are many situations where one does not expect a limited number of discrete decay times, but rather a distribution of decay times. Such behavior may be expected for a fluorophore in a mixture of solvents, so that a range of environments exists. One can imagine a fluorophore being surrounded by one, two, three, or more polar molecules, each resulting in a different intensity decay. Another possibility is a protein with many tryptophan residues, so that it is not practical to consider individual decay times.

In such cases the intensity decays are typically analyzed in terms of a lifetime distribution. In this case the α_i values are replaced by distribution functions $\alpha(\tau)$. The component with each individual τ value is given by

$$I(\tau,t) = \alpha(\tau)e^{-t/\tau} \tag{4.33}$$

However, one cannot observe these individual components with lifetime τ, but only the entire decay. The total decay law is the sum of the individual decays weighted by the amplitudes:

$$I(t) = \int_{\tau=0}^{\infty} \alpha(\tau)e^{-t/\tau}d\tau \tag{4.34}$$

where $\int\alpha(\tau)d\tau = 1.0$.

Lifetime distributions are usually used without a theoretical basis for the $\alpha(\tau)$ distribution. One typically uses arbitrarily selected Gaussian (G) and Lorentzian (L) lifetime distributions. For these functions the $\alpha(\tau)$ values are

$$\alpha_G(\tau) = \frac{1}{\sigma\sqrt{2\pi}} \exp\left\{-\frac{1}{2}\left(\frac{\tau - \bar{\tau}}{\sigma}\right)^2\right\} \tag{4.35}$$

$$\alpha_L(\tau) = \frac{1}{\pi} \frac{\Gamma/2}{(\tau - \bar{\tau})^2 + (\Gamma/2)^2} \tag{4.36}$$

where $(\bar{\tau})$ is the central value of the distribution, σ the standard deviation of the Gaussian, and Γ the full width at half maximum (FWHM) for the Lorentzian. For a Gaussian the full width at half maximum is given by 2.345σ. For ease of interpretation we prefer to describe both distributions by the full width at half maxima. An alternative approach would be to use $\alpha(\tau)$ distributions that are not described by any particular function. This approach may be superior in that it makes no assumptions about the shape of the distribution. However, the use of functional forms for $\alpha(\tau)$ minimizes the number of floating parameters in the fitting algorithms. Without an assumed function form it may be necessary to place restraints on the adjacent values of $\alpha(\tau)$.

By analogy with the multi-exponential model, it is possible that $\alpha(\tau)$ is multimodal. Then

$$\alpha(\tau) = \sum_i g_i \alpha_i^0(\tau) = \sum_i \alpha_i(\tau) \tag{4.37}$$

where *i* refers to the *i*th component of the distribution centered at α_i, and g_i represents the amplitude of this component. The g_i values are amplitude factors and $\alpha_i^0(\tau)$ the shape factors describing the distribution. If part of the distribution exists below $\tau = 0$, then the $\alpha_i(\tau)$ values need additional normalization. For any distribution, including those cut off at the origin, the amplitude associated with the *i*th mode of the distribution is given by

$$\alpha_i = \frac{\int_0^\infty \alpha_i(\tau)\, d\tau}{\int_0^\infty \sum_i \alpha_i(\tau) d\tau} \tag{4.38}$$

The fractional contribution of the *i*th component to the total emission is given by

$$f_i = \frac{\int_0^\infty \alpha_i(\tau)\tau d\tau}{\int_0^\infty \sum_i \alpha_i(\tau)\tau d\tau} \tag{4.39}$$

In the use of lifetime distributions each decay time component is associated with three variables, α_i, f_i and the half width (σ or Γ). Consequently, one can fit a complex decay with fewer exponential components. For instance, data that can be fit to three discrete decay times can typically be fit to a bimodal distribution model. In general, it is not possible to distinguish between the discrete multi-exponential model (eq. 4.27) or the lifetime distribution model (eq. 4.34), so the model selection must be based on one's knowledge of the system.[197–199]

4.11.3. Stretched Exponentials

A function similar to the lifetime distributions is the stretched exponential

$$I(t) = I_0 \exp[(-t/\tau)^{\beta}] \tag{4.40}$$

In this expression β is related to the distribution of decay times. The function is not used frequently in biophysics but is often found in studies of polymers when one expects a distribution of relaxation times. In a least-squares fit, β and τ would be the variable parameters.

4.11.4. Transient Effects

In many samples the intensity decay can be non-exponential due to phenomena which occur immediately following excitation. This occurs in collisional quenching and in resonance energy transfer. In the presence of a quencher, a fluorophore that displays an unquenched single-exponential lifetime will decay according to

$$I(t) = I_0 \exp(-t/\tau - 2bt^{1/2}) \tag{4.41}$$

In this expression b depends on the quencher concentration and diffusion coefficient. One can fit such decays to the multi-exponential model, but one would then erroneously conclude that there are two fluorophore populations. In this case a single fluorophore population gives a non-exponential decay due to rapid quenching of closely spaced fluorophore–quencher pairs.

Resonance energy transfer (RET) can also result in decays that have various powers of time in the exponent. Depending on whether RET occurs in one, two, or three dimensions, t can appear with powers of 1/6, 1/3, or 2 respectively. Hence we see that intensity decays can take a number of forms depending on the underlying molecular phenomenon. In our opinion it is essential to analyze each decay with the model that correctly describes the samples. Use of an incorrect model, such as the multi-exponential model, to describe transient effects, results in apparent parameter values (α_i and τ_i) that cannot be easily related to the quantities of interest (quencher concentration and diffusion coefficient).

4.12. GLOBAL ANALYSIS

In Section 4.10 we indicated the difficulties of resolving the decay times and amplitudes in a multi-exponential decay. The parameters in the various decay functions are correlated and difficult to resolve. The resolution of correlated parameters can be improved by the use of global analysis.[200–205] The procedure is to combine two or more experiments in which some of the parameters are the same in all measurements, and some are different. This can be illustrated by the emission spectra in Figure 4.53. A non-global experiment would be to recover the values of α_i and τ_i from the intensity decay collected at 380 nm, where all three fluorophores emit. A global experiment would be to measure the intensity decays at several wavelengths, say 360, 380, 400, and 420 nm. The multiple intensity decay curves are then analyzed simultaneously to recover the τ_i values and the $\alpha_i(\lambda)$ values. The τ_i values are assumed to be independent of emission wavelength. In the case of global analysis the calculation of χ_R^2 extends over several data sets. The global value of χ_R^2 is given by

$$\chi_R^2 = \frac{1}{\nu} \sum_{\lambda} \sum_{k=1}^{n} \frac{[I_c^{\lambda}(t_k) - I^{\lambda}(t_k)]^2}{I^{\lambda}(t_k)} \tag{4.42}$$

where the additional sum extends over the files measured at each wavelength (λ). For the fitted functions the α_i values are different at each wavelength $\alpha_i(\lambda)$ because of the different relative contributions of the three fluorophores. The values of τ_i are assumed to be independent of emission wavelength since each fluorophore is assumed to display a single exponential decay.

It is easy to see how global analysis can improve resolution. Suppose one of the intensity decays was measured at 320 nm. This decay would be almost completely due to indole (Figure 4.53), and thus would determine its lifetime without contribution from the other fluorophores. Since there is only one decay time, there would be no parameter correlation, and τ_1 would be determined with good certainty. The data at 320 nm will constrain the lifetime of indole in data measured at longer wavelengths and in effect decrease the number of variable parameters at this wavelength. Even if the choice of wavelengths only partially selects for a given fluorophore, the data serve to determine its decay time and reduce the uncertainty in the remaining parameters.

Global analysis was used to recover the lifetimes across the emission spectrum of the three-component mixture, using the decays measured from 360 to 440 nm. The lifetime χ_R^2 surface for the three decay times is shown in Figure 4.56. The expected decay time was recovered for each of the components. However, even with a multi-wave-

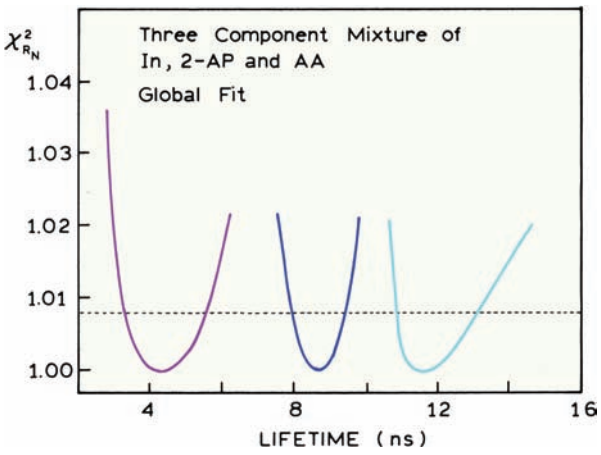

Figure 4.56. Global lifetime χ_R^2 surface for the three-component mixture of In, AA, and 2-AP. From [187].

length global analysis the uncertainties are significant. For instance, the value of the 4.1-ns lifetime can range from about 3.2 to 5.5 ns and still be consistent with the data.

4.13. APPLICATIONS OF TCSPC

The concepts described in the preceding sections can be made more understandable by examination of some specific examples.

4.13.1. Intensity Decay for a Single Tryptophan Protein

The tet repressor controls the gene in Gram-negative bacteria that provides resistance to the antibiotic tetracycline.[206] This protein usually contains two tryptophans, but a mutant protein was engineered that contains a single tryptophan residue at position 43. Intensity decays are shown in Figure 4.57. The light source was a frequency-doubled R6G dye laser at 590 nm, frequency doubled to 295 nm. The dye laser was cavity dumped at 80 kHz. The excitation was vertically polarized and the emission detected through a polarizer set 54.7° from the vertical. The use of magic-angle polarization conditions is essential in this case because the protein can be expected to rotate on a timescale comparable to the intensity decay. A Schott WG 320 filter was used in front of the monochromator to prevent scattered light from entering the monochromator, which was set at 360 nm.

The emission was detected with an XP-2020 PMT. This PMT shows a wavelength-dependent time response and an afterpulse. To avoid color effects the authors used a

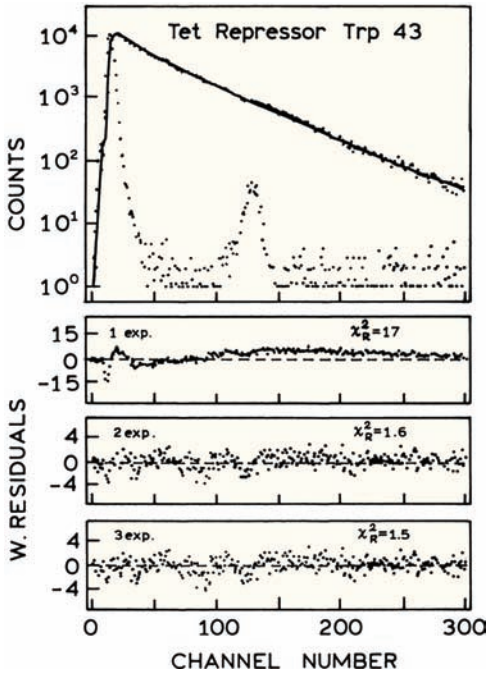

Figure 4.57. Intensity decay of trp-43 in the tet repressor protein F75 TetR at 360 nm. The calibration is 108 ps/channel. Revised and reprinted with permission from [206]. Copyright © 1992, American Chemical Society.

short-lifetime reference that shifted the wavelength to the measurement wavelength with minimal time delay.[112] This was accomplished with a solution of p-terphenyl highly quenched by CCl_4. The fact that the measurements were performed with a dynode PMT is evident from the width of the impulse response function, which appears to be near 500 ps. Some of this width may be contributed from the short lifetime standard.

The intensity decay was fit to the one, two, and three exponential models, resulting in χ_R^2 values of 17, 1.6, and 1.5, respectively. Rejection of the single-exponential model is clearly justified by the data. However, it is less clear that three decay times are needed. The ratio of the χ_R^2 values is 1.07, which is attributed to random error with a probability of over 20% (Table 4.3). The fractional amplitude of the third component was less than 1%, and the authors accepted the double exponential fit as descriptive of their protein.

4.13.2. Green Fluorescent Protein: Systematic Errors in the Data

Green fluorescent protein (GFP) spontaneously becomes fluorescent following synthesis of its amino-acid chain.

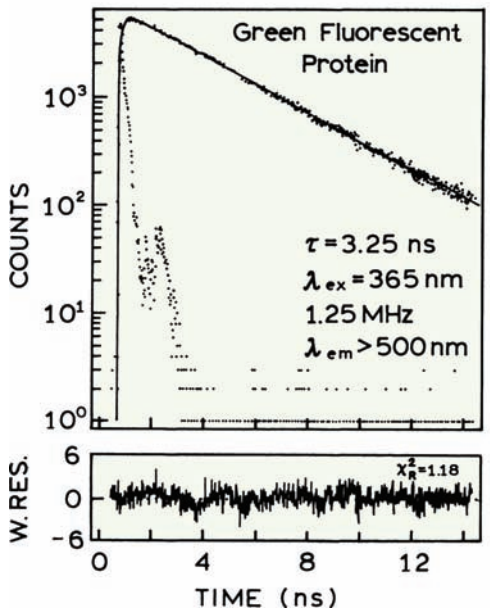

Figure 4.58. Intensity decay of green fluorescence protein. From [207].

GFPs are widely used as a tag to follow gene expression. The intensity decay of GFP was measured with 365-nm excitation, a 1.25-MHz repetition rate, and magic-angle polarizer conditions.[207] The emission was detected above 500 nm, using an MCP PMT.

The intensity decay of GFP could be well fit to a single exponential (Figure 4.58). The value of χ_R^2 is slightly elevated, and not consistent with a single exponential model. However, the value of χ_R^2 was not decreased by including a second decay time (χ_R^2 = 1.18). Examination of the deviations (lower panel) reveals the presence of systematic oscillations for which a second decay time does not improve the fit. The failure of χ_R^2 to decrease is typically an indication of systematic error as the origin of the elevated value of χ_R^2.

4.13.3. Picosecond Decay Time

The measurement of picosecond decay times remains challenging even with the most modern instruments for TCSPC. Figure 4.59 shows a schematic for a state-of-the-art instrument.[208] The primary source of excitation is a Ti:sapphire laser, which is pumped by a continuous argon ion laser. The repetition rate is decreased as needed by a pulse picker (PP). Additional excitation wavelengths are obtained using a harmonic generator (HG) for frequency doubling or tripling, or an optical parameter oscillator (OPO). The pulse

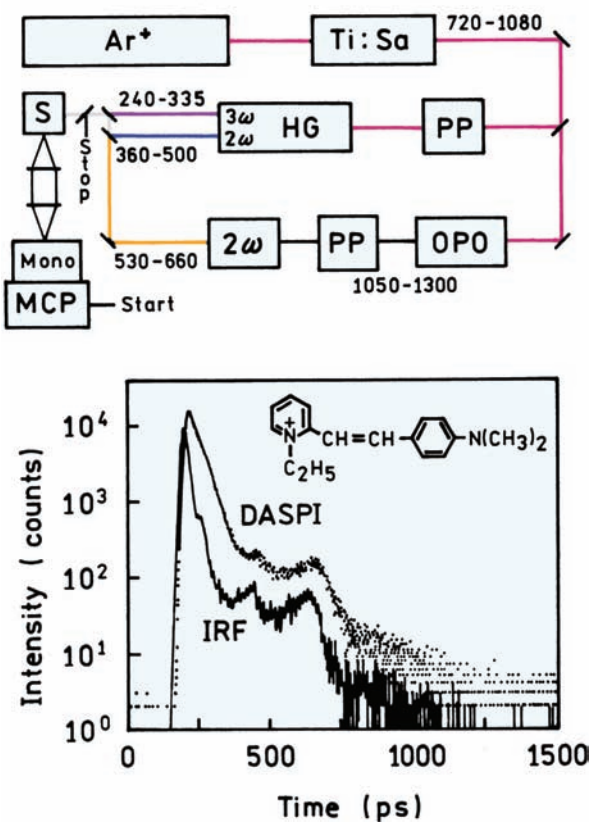

Figure 4.59. Intensity decay of DASPI in methanol. The upper panel shows a schematic of the instrument with a Ti:sapphire-OPO pump source at 543 nm and an R3809U MPC PMT. DASPI is 2-[2-[3-dimethylamino)phenyl]-ethyl]-N-methyl pyridinium iodide (DASPI). Revised from [208].

widths were near 1 ps. This instrument has an R3809U MCP PMT that has one of the smallest available transient time spreads.

The lower panel in Figure 4.59 shows the intensity decay of DASPI in methanol. DASPI has a very short decay time in this solvent. The intensity decay is not much wider than the IRF, which has an FWHM below 28 ps. The decay time recovered for DASPI is 27.5 ps. Comparison of the IRF and intensity decay of DASPI shows the need for deconvolution. In spite of the complex profile of these curves, they are consistent with a single-exponential decay of DASPI with a 27.5 ps lifetime.

4.13.4. Chlorophyll Aggregates in Hexane

The intensity decay for the tryptophan residues in the tet repressor was relatively close to a single exponential. Intensity decays can be much more heterogeneous. One example

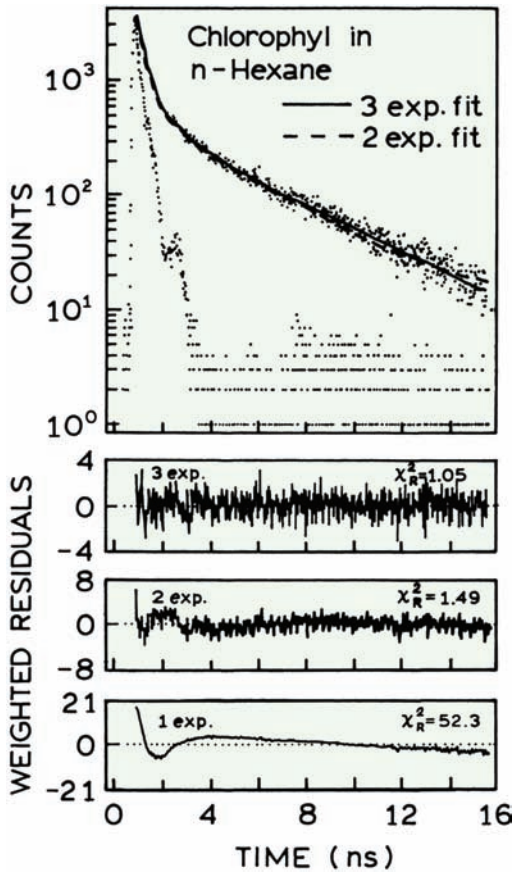

Figure 4.60. Intensity decay of chlorophyll in wet n-hexane [209].

is the intensity decay of chlorophyll in wet hexane solvents, in which chlorophyll exists in a variety of aggregated states.[209] Data were obtained using a Pyridine dye laser at 760 nm, which was cavity dumped at 1 MHz and frequency doubled to 380 nm. The emission was detected at 715 nm through an interference filter. The detector was an R2809 MCP PMT, with 6 micron channels. Even though the excitation and emission wavelengths were far apart (380 and 715 nm), color effect corrections did not seem necessary with this MCP PMT. Magic-angle polarizer conditions were used.

The intensity decay of chlorophyll was strongly heterogeneous (Figure 4.60). The decay could not even be approximated by a single decay time. The fit with two decay times was much improved, reducing χ_R^2 from 52.3 to 1.49. A further reduction of 40% in χ_R^2 occurred for the three-decay-time fit. The two-decay-time model can be rejected because this χ_R^2 ratio of 1.41 would only occur between 1 and 5% of the time due to statistical errors in the data (Table 4.3).

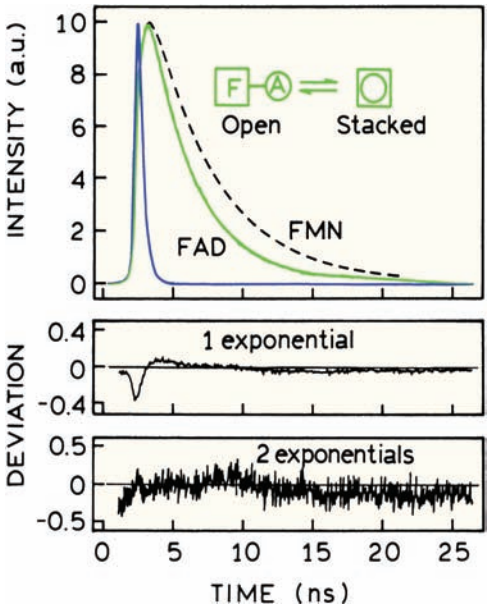

Figure 4.61. Intensity decays of FAD and FMN at pH 7.5, 3°C. Also shown is the laser pulse profile. The deviations are for fits to the FAD intensity decay. Data from [212].

Complex intensity decays with up to four lifetimes have been reported for photosynthetic systems.[210–211]

4.13.5. Intensity Decay of Flavin Adenine Dinucleotide (FAD)

Flavin adenine dinucleotide (FAD) is a cofactor in many enzymatic reactions. The fluorescent moiety is the flavin, which can be quenched on contact with the adenine. In solution FAD can exist in an open or stacked configuration. It is known that a significant amount of quenching occurs because cleavage of FAD with phosphodiesterase results in a several-fold increase in fluorescence intensity.

The nature of the flavin quenching by the adenine was studied by TCSPC.[212] Data were obtained using the output of a mode-locked argon ion laser at 457.9 nm. The detector was an XP 2020 linear-focused PMT, resulting in a relatively wide instrument response function (Figure 4.61). The intensity decay of the flavin alone (FMN) was found to be a single exponential with a decay time of 4.89 ns. FAD displayed a double-exponential decay with a component of 3.38 ns (α_i = 0.46) and of 0.12 ns (α_2 = 0.54). The short decay time component was assigned to the stacked forms, allowing calculation of the fraction of FAD present in the stacked and open conformations. The lifetime of 3.38 ns is thought to be due to dynamic quenching of the flavin by the adenine moiety.

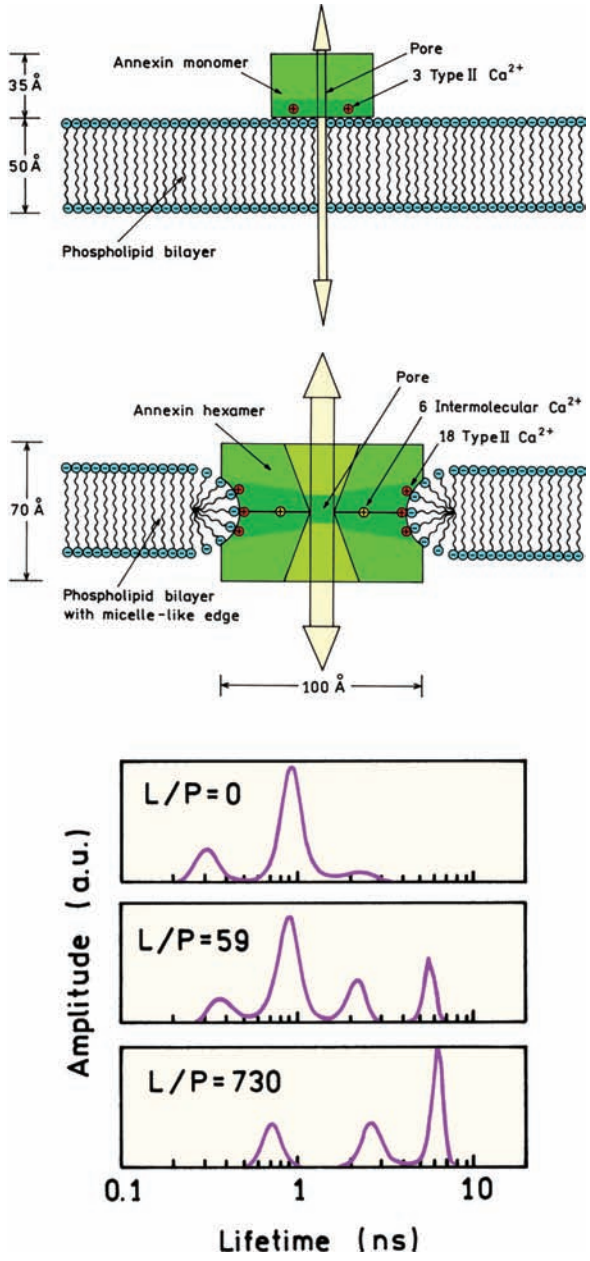

Figure 4.62. Lifetime distribution of Annexin V Domain III in the presence of phospholipid at various lipid-to-protein molar ratios (*L*/*P*). The lipid was an 80/20 molar ratio of DOPC and DOPS, where S indicates serine. Revised from [214]. The upper panel shows a schematic of Annexin insertion into membranes. Reprinted with permission from [218].

4.14. DATA ANALYSIS: MAXIMUM ENTROPY METHOD

Intensity decays of biomolecules are usually multi-exponential or non-exponential. The decays can be fitted using the multi-exponential model. However, it is difficult to obtain an intuitive understanding of the results by examining table of α_i and τ_i values. Analysis of the decays in terms of lifetime distribution (Section 4.11.2) is often useful for visualizing the decay. However, when using NLLS the lifetime distribution analysis is usually performed in terms of assumed shape functions (eqs. 4.35 and 4.36). Analysis using the maximum entropy method (MEM) allows recovery of lifetime distributions without assumptions about the shape of the components.

The MEM is mathematically complex[213–216] and the fitting criteria somewhat subjective. Most of the published analyses were performed using commercial algorithms which are not completely explained. Nonetheless, the MEM is now widely utilized and provides insight into complex intensity decays.

The MEM is based on maximizing a function called the Skilling-Jaynes entropy function:

$$S = \int_0^\infty \alpha(\tau) - m(\tau) - \alpha(\tau) \log \frac{\alpha(\tau)}{m(\tau)} d\tau \qquad (4.43)$$

In this expression $\alpha(\tau)$ is the recovered distribution and $m(\tau)$ is an assumed starting model that is flat in log τ space. The MEM method is not used alone, but the fits are performed while calculating χ_R^2 according to eq. 4.22 to ensure that the recovered distribution is consistent with the data. In contrast to NLLS there does not appear to be a well-defined stopping point for the MEM analysis. The analysis is stopped when χ_R^2 does not decrease more than 2% for 20 interactions. The MEM is advantageous because it provides smooth $\alpha(\tau)$ spectra that have enough detail to reveal the shape of the distribution. The MEM method is claimed to not introduce $\alpha(\tau)$ components unless they are needed to fit the data.

An example of an MEM analysis is shown in Figure 4.62 for domain III of Annexin V. Annexins are peripheral membrane proteins that interact with negatively charged phospholipids. Annexins can become inserted into membranes (Figure 4.62), so the tryptophan intensity decays are expected to be dependent on the presence of phospholipids. This domain of Annexin V contains a single tryptophan residue at position 187 (W187). The intensity decays of W187 were measured by TCSPC. The excitation source was synchrotron radiation that appeared as pulses at 13.6 MHz with a pulse width of 1.4 ns.[215] The maximum entropy analysis shows a shift from a dominant component near 0.9 ns in the absence of membrane to a longer-lived component

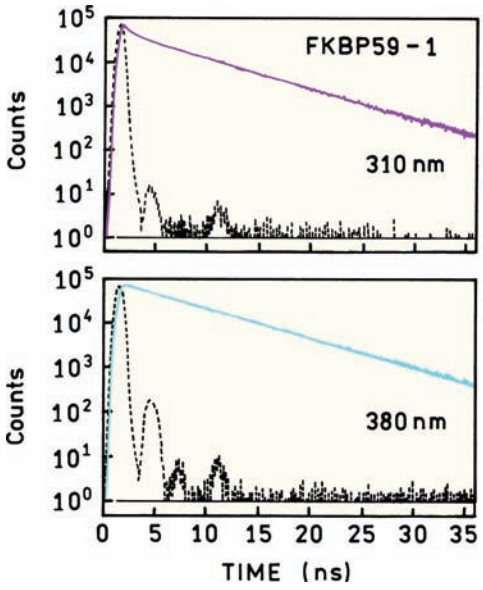

Figure 4.63. Tryptophan intensity decays of FKBP59-1 excited by synchrotron radiation at 295 nm and observed at 310 and 380 nm. Revised from [219].

near 6 ns in the presence of lipid. It is easier to visualize the effects of lipid from the distributions than from a table of parameter values.

Lifetime distributions and the MEM are also useful in visualizing the effects of observation wavelength on intensity decays.[219] The immunophilin FKBP59-1 contains two tryptophan residues, one buried and one exposed to the solvent (Chapter 16 and 17). The intensity decays are visually similar on the short (310 nm) and long (380 nm) sides of the emission spectrum (Figure 4.63). The difference between the decays are much more apparent in lifetime distributions recovered from the maximum entropy analysis (Figure 4.64). An excellent monograph has recently been published on TCSPC [220]. Readers are encouraged to see this book for additional details on TCSPC.

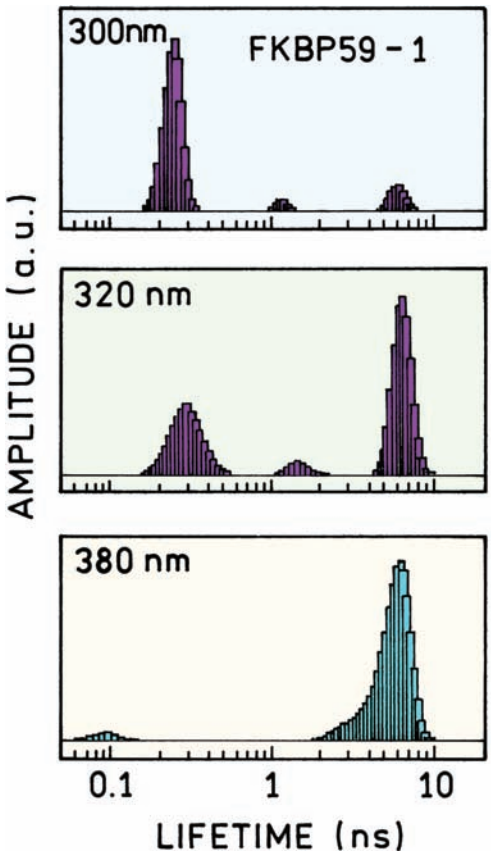

Figure 4.64. Lifetime distribution of the immunophilin FKBP59-1 recovered by the MEM. Revised from [219].

REFERENCES

1. Bevington PR, Robinson DK. 1992. *Data reduction and error analysis for the physical sciences*, 2nd ed. McGraw-Hill, New York.
2. Taylor JR. 1982. *An introduction to error analysis: the study of uncertainties in physical measurements*. University Science Books, Sausalito, CA.
3. Grinvald A, Steinberg IZ. 1974. On the analysis of fluorescence decay kinetics by the method of least-squares. *Anal Biochem* **59**:583–593.
4. Demas JN. 1983. *Excited state lifetime measurements*. Academic Press, New York.
5. Johnson ML. 1985. The analysis of ligand binding data with experimental uncertainties in the independent variables. *Anal Biochem* **148**:471–478.
6. Bard J. 1974. *Nonlinear parameter estimation*. Academic Press, New York.
7. Johnson ML. 1983. Evaluation and propagation of confidence intervals in nonlinear, asymmetrical variance spaces: analysis of ligand binding data. *Biophys J* **44**:101–106.
8. O'Connor DV, Phillips D. 1984. *Time-correlated single-photon counting*. Academic Press, New York.
9. Birch DJS, Imhof RE. 1991. Time-domain fluorescence spectroscopy using time-correlated single-photon counting. In *Topics in fluorescence spectroscopy*, Vol. 1: *Techniques*, pp. 1–95. Ed JR Lakowicz, Plenum Press, New York.
10. Ware WR. 1971. Transient luminescence measurements. In *Creation and detection of the excited state*, Vol. 1A, pp. 213–302. Ed AA Lamola. Marcel Dekker, New York.
11. Becker W, Bergmann A. 2005. Multidimensional time-correlated single-photon counting. In *Reviews in fluorescence*, Vol. 2, pp. 77–108. Ed CD Geddes, JR Lakowicz. Kluwer Academic/Plenum Publishers, New York.
12. Bassi A, Swartling J, D'Andrea C, Pifferi A, Torricelli A, Cubeddu R. 2004. Time-resolved spectrophotometer for a turbid media based on supercontinuum generation in a photonic crystal fiber. *Opt Lett* **29**(20):2405–2407.

13. Karolczak J, Komar D, Kubicki J, Wrozowa T, Dobek K, Ciesielska B, Maciejewski A. 2001. The measurements of picosecond fluorescence lifetimes with high accuracy and subpicosecond precision. *Chem Phys Lett* **344**:154–164.
14. Becker W, Hickl H, Zander C, Drexhage KH, Sauer M, Siebert S, Wolfrum J. 1999. Time-resolved detection and identification of single analyte molecules in microcapillaries by time-correlated single-photon counting (TCSPC). *Rev Sci Instrum* **70**(3):1835–1841.
15. Malak H. Unpublished observations.
16. Badea MG, Brand L. 1971. Time-resolved fluorescence measurements. *Methods Enzymol* **61**:378–425.
17. McGuinness CD, Sagoo K, McLoskey D, Birch DJS. 2004. A new sub-nanosecond LED at 280 nm: application to protein fluorescence. *Meas Sci Technol* **15**:L1–L4.
18. Pico Quant GmbH, Berlin, Germany http://www.picoquant.com/products_products.htm.
19. IBH Jobin Yvon, Glasgow, United Kingdom http://www.isainc.com/usadivisions/Fluorescence/IBH/nanoled.htm.
20. Becker and Hickl GmbH, Berlin, Germany, http://www.becker-heckl.de.
21. Hamamatsu Photonics, KK, Hamamatsu City, Japan, http://usa.hamamatsu.com.
22. http://www.picoquant.com/products/ledhead.htm.
23. O'Hagan WJ, McKenna M, Sherrington DC, Rolinski OJ, Birch DJS. 2002. MHz LED source for nanosecond fluorescence sensing. *Meas Sci Technol* **13**:84–91.
24. Svelto O. 1998. *Principles of lasers*, 4th ed. Transl DC Hanna. Plenum Press, New York.
25. Yariv A. 1989. *Quantum electronics*, 3rd ed. John Wiley & Sons, New York.
26. Iga, K. 1994. *Fundamentals of laser optics*. Plenum Press, New York.
27. Small EW. 1991. Laser sources and microchannel plate detectors for pulse fluorometry. In *Topics in fluorescence spectroscopy*, Vol. 1: *Techniques*, pp. 97–182. Ed JR Lakowicz. Plenum Press, New York.
28. Wilson J, Hawkes JFB. 1983. *Optoelectronics: an introduction*. Prentice Hall, Englewood Cliffs, NJ.
29. Berg NJ, Lee JN, eds. 1983. *Acoustooptic signal processing*. Marcel Dekker, Inc., New York.
30. Visser AJWG, Van Hoek A. 1979. The measurement of subnanosecond fluorescence decay of flavins using time-correlated photon counting and a mode-locked Ar ion laser. *J Biochem Biophys Methods* **1**:195–208.
31. Spears KG, Cramer LE, Hoffland LD. 1978. Subnanosecond time-correlated photon counting with tunable lasers. *Rev Sci Instrum* **49**:255–262.
32. Lytle E, Kelsey MS. 1974. Cavity-dumped argon-ion laser as an excitable source on time-resolved fluorimetry. *Anal Chem* **46**:855–860.
33. Wild UP, Holzwarth AR, Good HP. 1977. Measurement and analysis of fluorescence decay curves. *Rev Sci Instrum* **48**(12):1621–1627.
34. Turko BT, Nairn JA, Sauer K. 1983. Single photon timing system for picosecond fluorescence lifetime measurements. *Rev Sci Instrum* **54**(1):118–120.
35. Alfano AJ, Fong FK, Lytle FE. 1983. High repetition rate subnanosecond gated photon counting. *Rev Sci Instrum* **54**(8):967–972.
36. Kinoshita S, Ohta H, Kushida T. 1981. Subnanosecond fluorescence lifetime measuring system using single photon counting method with mode-locked laser excitation. *Rev Sci Instrum* **52**(4):572–575.
37. Koester VJ, Dowben RM. 1978. Subnanosecond single photon counting fluorescence spectroscopy using synchronously pumped tunable dye laser excitation. *Rev Sci Instrum* **49**(8):1186–1191.
38. Zimmerman HE, Penn JH, Carpenter CW. 1982. Evaluation of single-photon counting measurements of excited-state lifetimes. *Proc Natl Acad Sci USA* **79**:2128–2132.
39. van Hoek A, Vervoort J, Visser AJWG. 1983. A subnanosecond resolving spectrofluorimeter for the analysis of protein fluorescence kinetics. *J Biochem Biophys Methods* **7**:243–254.
40. Small EW, Libertini LJ, Isenberg I. 1984. Construction and tuning of a monophoton decay fluorometer with high-resolution capabilities. *Rev Sci Instrum* **55**(6):879–885.
41. Visser AJWG, van Hoek A. 1981. The fluorescence decay of reduced nicotinamides in aqueous solution after excitation with a UV-mode locked Ar Ion laser. *Photochem Photobiol* **33**:35–40.
42. Libertini LJ, Small EW. 1987. On the choice of laser dyes for use in exciting tyrosine fluorescence decays. *Anal Biochem* **163**:500–505.
43. Malmberg JH. 1957. Millimicrosecond duration of light source. *Rev Sci Instrum* **28**(12):1027–1029.
44. Bennett RG. 1960. Instrument to measure fluorescence lifetimes in the millimicrosecond region. *Rev Sci Instrum* **31**(12):1275–1279.
45. Yguerabide J. 1965. Generation and detection of subnanosecond light pulses: application to luminescence studies. *Rev Sci Instrum* **36**(12):1734–1742.
46. Birch DJS, Imhof RE. 1977. A single photon counting fluorescence decay-time spectrometer. *J Phys E: Sci Instrum* **10**:1044–1049.
47. Lewis C, Ware WR, Doemeny LJ, Nemzek TL. 1973. The measurement of short lived fluorescence decay using the single photon counting method. *Rev Sci Instrum* **44**:107–114.
48. Leskovar B, Lo CC, Hartig PR, Sauer K. 1976. Photon counting system for subnanosecond fluorescence lifetime measurements. *Rev Sci Instrum* **47**(9):1113–1121.
49. Bollinger LM, Thomas GE. 1961. Measurement of the time dependence of scintillation intensity by a delayed-coincidence method. *Rev Sci Instrum* **32**(9):1044–1050.
50. Hazan G, Grinvald A, Maytal M, Steinberg IZ. 1974. An improvement of nanosecond fluorimeters to overcome drift problems. *Rev Sci Instrum* **45**(12):1602–1604.
51. Dreeskamp H, Salthammer T, Laufer AGE. 1989. Time-correlated single-photon counting with alternate recording of excitation and emission. *J Lumin* **44**:161–165.
52. Birch DJS, Imhof RE. 1981. Coaxial nanosecond flashlamp. *Rev Sci Instrum* **52**:1206–1212.
53. Birch DJS, Hungerford G, Imhof RE. 1991. Near-infrared spark source excitation for fluorescence lifetime measurements. *Rev Sci Instrum* **62**(10):2405–2408.
54. Birch DJS, Hungerford G, Nadolski B, Imhof RE, Dutch A. 1988. Time-correlated single-photon counting fluorescence decay studies at 930 nm using spark source excitation. *J Phys E: Sci Instrum* **21**:857–862.
55. http://www.ibh.co.uk/products/lightsources/5000f.htm.
56. Laws WR, Sutherland JC. 1986. The time-resolved photon-counting fluorometer at the national synchrotron light source. *Photochem Photobiol* **44**(3):343–348.
57. Munro IH, Martin MM. 1991. Time-resolved fluorescence spectroscopy using synchrotron radiation. In *Topics in fluorescence spectroscopy*, Vol. 1: *Techniques*, pp. 261–291. Ed JR Lakowicz. Plenum Press, New York.
58. Munro IH, Schwentner N. 1983. Time-resolved spectroscopy using synchrotron radiation. *Nucl Instrum Methods* **208**:819–834.
59. Lopez-Delgado R. 1978. Comments on the application of synchrotron radiation to time-resolved spectrofluorometry. *Nucl Instrum Methods* **152**:247–253.
60. Rehn V. 1980. Time-resolved spectroscopy in synchrotron radiation. *Nucl Instrum Methods* **177**:193–205.

61. van Der Oord CJR, Gerritsen HC, Rommerts FFG, Shaw DA, Munro IH, Levine YK. 1995. Micro-volume time-resolved fluorescence spectroscopy using a confocal synchrotron radiation microscope. *Appl Spec* **49**(10):1469–1473.
62. Gedcke DA, McDonald WJ. 1967. A constant fraction of pulse height trigger for optimum time resolution. *Nucl Instrum Methods* **55**:377–380.
63. Gedcke DA, McDonald WJ. 1966. Design of the constant fraction of pulse height trigger for optimum time resolution. *Nucl Instrum Methods* **58**:253–260.
64. Arbel A, Klein I, Yarom A1974. Snap-off constant fraction timing discriminators. *IEEE Trans Nucl Sci* **NS–21**:3-8.
65. Becker & Hickl Gmbh, Berlin, Germany. *How (and why not) to amplify PMT signals*. http://www.becker-hickl.de.
66. Cova S, Ghioni M, Zappa F, Lacaita A. 1993. Constant-fraction circuits for picosecond photon timing with microchannel plate photomultipliers. *Rev Sci Instrum* **64**(1):118–124.
67. Cova S, Ripamonti G. 1990. Improving the performance of ultrafast microchannel plate photomultipliers in time-correlated photon counting by pulse pre-shaping. *Rev Sci Instrum* **61**(3):1072–1075.
68. Haugen GR, Wallin BW, Lytle FE. 1979. Optimization of data-acquisition rates in time-correlated single-photon fluorimetry. *Rev Sci Instrum* **50**(1):64–72.
69. Bowman LE, Berglund KA, Nocera DG. 1993. A single photon timing instrument that covers a broad temporal range in the reversed timing configuration. *Rev Sci Instrum* **64**(2):338–341.
70. Baumier W, Schmalzl AX, Göâl G, Penzkofer A. 1992. Fluorescence decay studies applying a cw femtosecond dye laser pumped ungated inverse time-correlated single photon counting system. *Meas Sci Technol* **3**:384–393.
71. Harris CM, Selinger BK. 1979. Single-photon decay spectroscopy, II: the pileup problem. *Aust J Chem* **32**:2111–2129.
72. Williamson JA, Kendall-Tobias MW, Buhl M, Seibert M. 1988. Statistical evaluation of dead time effects and pulse pileup in fast photon counting: introduction of the sequential model. *Anal Chem* **60**:2198–2203.
73. Candy BH. 1985. Photomultiplier characteristics and practice relevant to photon counting. *Rev Sci Instrum* **56**(2):183–193.
74. Hungerford G, Birch DJS. 1996. Single-photon timing detectors for fluorescence lifetime spectroscopy. *Meas Sci Technol* **7**:121–135.
75. Leskovar B. 1977. Microchannel plates. *Phys Today* **30**:42–49.
76. Boutot JP, Delmotte JC, Miehé JA, Sipp B. 1977. Impulse response of curved microchannel plate photomultipliers. *Rev Sci Instrum* **48**(11):1405–1407.
77. Timothy JG, Bybee RL. 1977. Preliminary results with microchannel array plates employing curved microchannels to inhibit ion feedback. *Rev Sci Instrum* **48**(3):292–299.
78. Lo CC, Leskovar B. 1981. Performance studies of high gain photomultiplier having z-configuration of microchannel plates. *IEEE Trans Nucl Sci* **NS–28**(1):698-704.
79. Ito M, Kume H, Oba K. 1984. Computer analysis of the timing properties in micro channel plate photomultiplier tubes. *IEEE Trans Nucl Sci* **NS–31**(1):408-412.
80. Bebelaar D. 1986. Time response of various types of photomultipliers and its wavelength dependence in time-correlated single photon counting with an ultimate resolution of 47 ps FWHM. *Rev Sci Instrum* **57**(6):1116–1125.
81. Yamazaki I, Tamai N, Kume H, Tsuchiya H, Oba K. 1985. Microchannel plate photomultiplier applicability to the time-correlated photon-counting method. *Rev Sci Instrum* **56**(6):1187–1194.
82. Uyttenhove J, Demuynck J, Deruytter A. 1978. Application of a microchannel plate photomultiplier in subnanosecond lifetime measurements. *IEEE Trans Nucl Sci* **NS–25**(1):566-567.
83. Murao T, Yamazaki I, Shindo Y, Yoshihara K. 1982. A subnanosecond time-resolved spectrophotometric system by using synchronously pumped, mode-locked dye laser. *J Spectrosc Soc Jpn*, pp. 96–103.
84. Murao T, Yamazaki I, Yoshihara K. 1982. Applicability of a microchannel plate photomultiplier to the time-correlated photon counting technique. *Appl Opt* **21**(13):2297–2298.
85. Hamamatsu Photonics KK. 1997. *Microchannel plate-photomultiplier tube (MCP-PMTs) R38097-50 series*.
86. Koyama K, Fatlowitz D. 1987. Application of MCP-PMTs to time correlated single photon counting and related procedures. *Hamamatsu Tech Inf* **ET-03**:1–18.
87. Kume H, Taguchi T, Nakatsugawa K, Ozawa K, Suzuki S, Samuel R, Nishimura Y, Yamazaki I. 1992. Compact ultrafast microchannel plate photomultiplier tube. *SPIE Proc* **1640**:440–447.
88. Boens N, Tamai N, Yamazaki I, Yamazaki T. 1990. Picosecond single photon timing measurements with a proximity type microchannel plate photomultiplier and global analysis with reference convolution. *Photochem Photobiol* **52**(4):911–917.
89. Lo CC, Leskovar B. 1979. Studies of prototype high-gain microchannel plate photomultipliers. *IEE Trans Nucl Sci* **NS–26**(1):388-394.
90. Becker & Hickl GmbH, Berlin, Germany. AMPTM1.doc.
91. Becker W, Bergmann A., Becker & Hickl GmbH. *Detectors for high-speed photon counting*.
92. Beck G. 1976. Operation of a 1P28 photomultiplier with subnanosecond response time. *Rev Sci Instrum* **47**:537–541.
93. Kinoshita S, Kushida T. 1982. High-performance, time-correlated single photon counting apparatus using a side-on type photomultiplier. *Rev Sci Instrum* **53**(4):469–472.
94. Canonica S, Forrer J, Wild UP. 1985. Improved timing resolution using small side-on photomultipliers in single photon counting. *Rev Sci Instrum* **56**(9):1754–1758.
95. Ware WR, Pratinidhi M, Bauer RK. 1983. Performance characteristics of a small side-window photomultiplier in laser single-photon fluorescence decay measurements. *Rev Sci Instrum* **54**:1148–1156.
96. Hamamatsu Photonics KK. 2001. *Metal package photomultiplier tube R7400U series*.
97. Hamamatsu Photonics KK. 2000. *Photosensor modules H5773/H5783/H6779/H6780/H5784 series*.
98. Cova S, Longoni A, Andreoni A, Cubeddu R. 1983. A semiconductor detector for measuring ultraweak fluorescence decays with 70ps FWHM resolution. *IEEE J Quantum Electron* **QE–19**:630-634.
99. Buller GS, Massa JS, Walker AC. 1992. All solid-state microscope-based system for picosecond time-resolved photoluminescence measurements on II-VI semiconductors. *Rev Sci Instrum* **63**(5):2994–2998.
100. Louis TA, Ripamonti G, Lacaita A. 1990. Photoluminescence lifetime microscope spectrometer based on time-correlated single-photon counting with an avalanche diode detector. *Rev Sci Instrum* **61**(1):11–22.
101. Cova S, Ripamonti G, Lacaita A. 1987. Avalanche semiconductor detector for single optical photons with a time resolution of 60 ps. *Nucl Instrum Methods Phys Res* **A253**:482–487.
102. Cova S, Lacaita A, Ghioni M, Ripamonti G, Louis TA. 1989. 20-ps timing resolution with single-photon avalanche diodes. *Rev Sci Instrum* **60**(6):1104–1110.
103. Cova S, Longoni A, Andreoni A. 1981. Towards picosecond resolution with single-photon avalanche diodes. *Rev Sci Instrum* **52**(3):408–412.
104. Louis T, Schatz GH, Klein-Bölting P, Holzwarth AR, Ripamonti G, Cova S. 1988. Performance comparison of a single-photon avalanche diode with a microchannel plate photomultiplier in time-correlated single-photon counting. *Rev Sci Instrum* **59**(7):1148–1152.

105. Lacaita A, Cova S, Ghioni M. 1988. Four-hundred picosecond single-photon timing with commerically available avalanche photodiodes. *Rev Sci Instrum* **59**(7):1115–1121.
106. Wahl P, Auchet JC, Donzel B. 1974. The wavelength dependence of the response of a pulse fluorometer using the single photoelectron counting method. *Rev Sci Instrum* **45**(1):28–32.
107. Sipp B, Miehe JA, Lopez-Delgado R. 1976. Wavelength dependence of the time resolution of high-speed photomultipliers used in single-photon timing experiments. *Opt Commun* **16**(1):202–204.
108. Rayner DM, McKinnon AF, Szabo AG. 1978. Confidence in fluorescence lifetime determinations: a ratio correction for the photomultiplier time response variation with wavelength. *Can J Chem* **54**:3246–3259.
109. Thompson RB, Gratton E. 1988. Phase fluorometric method for determination of standard lifetimes. *Anal Chem* **60**:670–674.
110. Meister EC, Wild UP, Klein-Bölting P, Holzwarth AR. 1988. Time response of small side-on photomultiplier tubes in time-correlated single-photon counting measurements. *Rev Sci Instrum* **59**(3): 499–501.
111. Bauer RK, Balter A. 1979. A method of avoiding wavelength-dependent errors in decay-time measurements. *Opt Commun* **28**(1):91–96.
112. Kolber ZS, Barkley MD. 1986. Comparison of approaches to the instrumental response function in fluorescence decay measurements. *Anal Biochem* **152**:6–21.
113. Vecer J, Kowalczyk AA, Davenport L, Dale RE. 1993. Reconvolution analysis in time-resolved fluorescence experiments, an alternative approach: reference-to-excitation-to-fluorescence reconvolution. *Rev Sci Instrum* **64**(12):3413–3424.
114. Van Den Zegel M, Boens N, Daems D, De Schryver FC. 1986. Possibilities and limitations of the time-correlated single photon counting technique: a comparative study of correction methods for the wavelength dependence of the instrument response function. *Chem Phys* **101**:311–335.
115. James DR, Demmer DRM, Verrall RE, Steer RP. 1983. Excitation pulse-shape mimic technique for improving picosecond-laser excited time-correlated single-photon counting deconvolutions. *Rev Sci Instrum* **54**(9):1121–1130.
116. Zuker M, Szabo AG, Bramall L, Krajcarski DT, Selinger B. 1985. Delta function convolution method (DFCM) for fluorescence decay experiments. *Rev Sci Instrum* **56**(1):14–22.
117. Castelli F. 1985. Determination of correct reference fluorescence lifetimes by self-consitent internal calibration. *Rev Sci Instrum* **56**(4):538–542.
118. Vos K, van Hoek A, Visser AJWG. 1987. Application of a reference convolution method to tryptophan fluorescence in proteins. *Eur J Biochem* **165**:55–63.
119. Martinho JMG, Egan LS, Winnik MA. 1987. Analysis of the scattered light component in distorted fluorescence decay profiles using a modified delta function convolution method. *Anal Chem* **59**:861–864.
120. Ricka J. 1981. Evaluation of nanosecond pulse-fluorometry measurements: no need for the excitation function. *Rev Sci Instrum* **52**(2):195–199.
121. Visser AJWG, Kulinski T, van Hoek A. 1988. Fluorescence lifetime measurements of pseudoazulenes using picosecond-resolved single photon counting. *J Mol Struct* **175**:111–116.
122. Holtom GR. 1990. Artifacts and diagnostics in fast fluorescence measurements. *SPIE Proc* **1204**:2–12.
123. Grinvald A. 1976. The use of standards in the analysis of fluorescence decay data. *Anal Biochem* **75**:260–280.
124. Lampert RA, Chewter LA, Phillips D, O'Connor DV, Roberts AJ, Meech SR. 1983. Standards for nanosecond fluorescence decay time measurements. *Anal Chem* **55**:68–73.
125. Schiller NH, Alfano RR. 1980. Picosecond characteristics of a spectrograph measured by a streak camera/video readout system. *Opt Commun* **35**(3):451–454.
126. Rubin B, Herman RM. 1981. Monochromators as light stretchers. *Am J Phys* **49**(9):868–871.
127. Imhof RE, Birch DJS. 1982. Distortion of gaussian pulses by a diffraction grating. *Opt Commun* **42**(2):83–86.
128. Saari P, Aaviksoo J, Freiberg A, Timpmann K. 1981. Elimination of excess pulse broadening at high spectral resolution of picosecond duration light emission. *Opt Commun* **39**(1,2):94–98.
129. Bebelaar D. 1986. Compensator for the time dispersion in a monochromator. *Rev Sci Instrum* **57**:1686–1687.
130. Beechem JM. 1992. Multi-emission wavelength picosecond time-resolved fluorescence decay data obtained on the millisecond time scale: application to protein: DNA interactions and protein folding reactions. *SPIE Proc* **1640**:676–680.
131. Birch DJS, McLoskey D, Sanderson A, Suhling K, Holmes AS. 1994. Multiplexed time-correlated single-photon counting. *J Fluoresc* **4**(1):91–102.
132. McLoskey D, Birch DJS, Sanderson A, Suhling K, Welch E, Hicks PJ. 1996. Multiplexed single-photon counting, I: a time-correlated fluorescence lifetime camera. *Rev Sci Instrum* **67**(6):2228–2237.
133. Suhling K, McLoskey D, Birch DJS. 1996. Multiplexed single-photon counting, II: the statistical theory of time-correlated measurements. *Rev Sci Instrum* **67**(6):2238–2246.
134. Becker W, Bergmann A, Giscotti G, Rück A. 2004. Advanced time-correlated photon counting technique for spectroscopy and imaging in biomedical systems. *Proc SPIE* **5340**:104–112.
135. Becker W, Bergmann A, Wabnitz H, Grosenick D, Liebert A. 2001. High count rate multichannel TCSPC for optical tomography. *Eur Conf Biomed Opt: Proc SPIE* **4431**:249–254.
136. Hamamatsu Photonics KK. Phototube Manual
137. Zhu L, Stryjewski WJ, Soper SA. 2004. Multiplexed fluorescence detection in microfabricated devices with both time-resolved and spectral-discrimination capabilities using near-infrared fluorescence. *Anal Biochem* **330**:206–218.
138. Lassiter SJ, Stryjewski W, Legendre BL, Erdmann R, Wahl M, Wurm J, Peterson R, Middendorf L, Soper SA. 2000. Time-resolved fluorescence imaging of slab gels for lifetime base-calling in DNA sequencing applications. *Anal Chem* **72**:5373–5382.
139. He H, McGown LB. 2000. DNA sequencing by capillary electrophoresis with four-decay fluorescence detection. *Anal Chem* **72**:5865–5873.
140. Sauer M, Arden-Jacob J, Drexhage KH, Gobel F, Lieberwirth U, Muhlegger K, Muller R, Wolfrum J, Zander C 1998. Time-resolved identification of individual mononucleotide molecules in aqueous solution with pulsed semiconductor lasers. *Bioimaging* **6**:14–24.
141. Waddell E, Wang Y, Stryjewski W, McWhorter S, Henry AC, Evans D, McCarley RL, Soper SA. 2000. High-resolution near-infrared imaging of DNA microarrays with time-resolved acquisition of fluorescence lifetimes. *Anal Chem* **72**:5907–5917.
142. Zhu L, Stryjewski W, Lassiter S, Soper SA. 2003. Fluorescence multiplexing with time-resolved and spectral discrimination using a near-IR detector. *Anal Chem* **75**:2280–2291.
143. Hall P, Sellinger B. 1981. Better estimates of exponential decay parameters. *J Phys Chem* **85**:2941–2946.
144. Tellinghuisen J, Wilkerson CW. 1993. Bias and precision in the estimation of exponential decay parameters from sparse data. *Anal Chem* **65**:1240–1246.

145. Bhaumik ML, Clark GL, Snell J, Ferder L. 1965. Stroboscopic time-resolved spectroscopy. *Rev Sci Instrum* **36**(1):37–40.
146. Barisas BG, Leuther MD. 1980. Grid-gated photomultiplier photometer with subnanosecond time response. *Rev Sci Instrum* **51**(1):74–78.
147. Steingraber OJ, Berlman IB. 1963. Versatile technique for measuring fluorescence decay times in the nanosecond region. *Rev Sci Instrum* **34**(5):524–529.
148. Hundley L, Coburn T, Garwin E, Stryer L. 1967. Nanosecond fluorimeter. *Rev Sci Instrum* **38**(4):488–492.
149. James DR, Siemiarczuk A, Ware WR. 1992. Stroboscopic optical boxcar technique for the determination of fluorescence lifetimes. *Rev Sci Instrum* **63**(2):1710–1716.
150. Pitts JD, Mycek M-A. 2001. Design and development of a rapid acquisition laser-based fluorometer with simultaneous spectral and temporal resolution. *Rev Sci Instrum* **72**(7):3061–3072.
151. Nordlund TM. 1991. Streak camera for time-domain fluorescence. In *Topics in fluorescence spectroscopy*, Vol. 1: *Techniques*, pp. 183–260. Ed JR Lakowicz. Plenum Press, New York.
152. Schiller NH. 1984. Picosecond streak camera photonics. In *Semiconductors probed by ultrafast laser spectroscopy*, Vol. 2, pp. 441–458. Academic Press, New York.
153. Campillo AJ, Shapiro SL. 1983. Picosecond streak camera fluorometry: a review. *IEEE J Quantum Electron* **QE-19**:585–603.
154. Knox W, Mourou G. 1981. A simple jitter-free picosecond streak camera. *Opt Commun* **37**(3):203–206.
155. Ho PP, Katz A, Alfano RR, Schiller NH. 1985. Time response of ultrafast streak camera system using femtosecond laser pulses. *Opt Commun* **54**(1):57–62.
156. Tsuchiya Y, Shinoda Y. 1985. Recent developments of streak cameras. *Proc SPIE* **533**:110–116.
157. Kinoshita K, Ito M, Suzuki Y. 1987. Femtosecond streak tube. *Rev Sci Instrum* **58**(6):932–938.
158. Watanabe M, Koishi M, Roehrenbeck PW. 1993. Development and characteristics of a new picosecond fluorescence lifetime system. *SPIE Proc* **1885**:155–164.
159. Wiessner A, Staerk H. 1993. Optical design considerations and performance of a spectro-streak apparatus for time-resolved fluorescence spectroscopy. *Rev Sci Instrum* **64**(12):3430–3439.
160. Graf U, Bühler C, Betz M, Zuber H, Anliker M. 1994. Optimized streak-camera system: Wide excitation range and extended time scale for fluorescence lifetime measurement. *SPIE Proc* **2137**:204–210.
161. Techert S, Wiessner A, Schmatz S, Staerk H. 2001. Time-resolved fluorescence and solvatochromy of directly linked pyrene-DMA derivatives in alcoholic solution. *J Phys Chem B* **105**:7579–7587.
162. Hamamatsu Photonics KK. *Picosecond fluorescence lifetime measurement system C4780*.
163. Herman P, Lakowicz JR. Unpublished observations.
164. Porter G, Reid ES, Tredwell CJ. 1974. Time-resolved fluorescence in the picosecond region. *Chem Phys Lett* **29**(3):469–472.
165. Beddard GS, Doust T, Porter G. 1981. Picosecond fluorescence depolarisation measured by frequency conversion. *Chem Phys* **61**:17–23.
166. Kahlow MA, Jarzeba W, DuBruil TP, Barbara PF. 1988. Ultrafast emission spectroscopy in the ultraviolet by time-gated upconversion. *Rev Sci Instrum* **59**(7):1098–1109.
167. Morandeira A, Fürstenberg A, Gumy J-C, Vauthey E. 2003. Fluorescence quenching in electron-donating solvents, 1: influence of the solute-solvent interactions on the dynamics. *J Phys Chem A* **107**:5375–5383.
168. Morandeira A, Fürstenberg A, Vauthey E. 2004. Fluorescence quenching in electron-donating solvents, 2: solvent dependence and product dynamics. *J Phys Chem A*. **108**:8190–8200.
169. PicoQuant GmbH, NanoHarp 250 Multiscaler Board, http://picoquant.com/products/spec_nanoharp.html.
170. Ware WR, Doemeny LJ, Nemzek TL. 1973. Deconvolution of fluorescence and phosphorescence decay curves: a least-squares method. *J Phys Chem* **77**(17):2038–2048.
171. Isenberg I, Dyson RD, Hanson R. 1973. Studies on the analysis of fluorescence decay data by the method of moments. *Biophys J* **13**:1090–1115.
172. Small EW, Isenberg I. 1977. On moment index displacement. *J Chem Physiol* **66**:3347–3351.
173. Small EW. 1992. Method of moments and treatment of nonrandom error. *Methods Enzymol* **210**:237–279.
174. Gafni A, Modlin RL, Brand L. 1975. Analysis of fluorescence decay curves by means of the Laplace transformation. *Biophys J* **15**:263–280.
175. Almgren M. 1973. Analysis of pulse fluorometry data of complex systems. *Chem Scr* **3**:145–148.
176. Ameloot M. 1992. Laplace deconvolution of fluorescence decay surfaces. *Methods Enzymol* **210**:237–279.
177. Ameloot M, Hendrickx H. 1983. Extension of the performance of laplace deconvolution in the analysis of fluorescence decay curves. *Biophys J* **44**:27–38.
178. Livesey AK, Brochon JC. 1987. Analyzing the distribution of decay constants in pulse-fluorimetry using the maximum entropy method. *Biophys J* **52**:693–706.
179. Brochon J-C. 1994. Maximum entropy method of data analysis in time-resolved spectroscopy. *Methods Enzymol* **240**:262–311.
180. Zhang Z, Grattan KTV, Hu Y, Palmer AW, Meggitt BT. 1996. Prony's method for exponential lifetime estimations in fluorescence based thermometers. *Rev Sci Instrum* **67**(7):2590–2594.
181. López RJ, González F, Moreno F. 1992. Application of a sine transform method to experiments of single-photon decay spectroscopy: single exponential decay signals. *Rev Sci Instrum* **63**(6):3268–3273.
182. Carraway ER, Hauenstein BL, Demas JN, DeGraff BA. 1985. Luminescence lifetime measurements: elimination of phototube time shifts with the phase plane method. *Anal Chem* **57**:2304–2308.
183. Novikov EG. 1998. Reference reconvolution analysis by phase plane method. *Rev Sci Instrum* **69**(7):2603–2610.
184. O'Connor DVO, Ware WR, Andre JC. 1979. Deconvolution of fluorescence decay curves: a critical comparison of techniques. *J Phys Chem* **83**:1333–1343.
185. Johnson ML. 1994. Use of least-squares techniques in biochemistry. *Methods Enzymol* **240**:1–22.
186. Straume M, Frasier-Cadoret SG, Johnson ML. 1991. Least-squares analysis of fluorescence data. In *Topics in fluorescence spectroscopy*, Vol. 2: *Principles*, pp. 177–239. Ed JR Lakowicz. Plenum Press, New York.
187. Gryczynski I. Unpublished observations.
188. Montgomery DC, Peck EA. 1982. *Introduction to linear regression analysis*. John Wiley & Sons, New York.
189. Johnson ML. Personal communication.
190. Johnson ML, Faunt LM. 1992. Parameter estimation by least-squares methods. *Methods Enzymol* **210**:1–37.
191. Johnson ML, Frasier SG. 1985. Nonlinear least-squares analysis. *Methods Enzymol* **117**:301–342.
192. Box GEP. 1960. Fitting empirical data. *Ann NY Acad Sci* **86**:792–816.
193. Bates DM, Watts DG. 1988. *Nonlinear regression analysis and its applications*. John Wiley. New York.
194. Straume M, Johnson ML. 1992. Monte Carlo method for determining complete confidence probability distributions of estimated model parameters. *Methods Enzymol* **210**:117–129.

195. Alcala JR. 1994. The effect of harmonic conformational trajectories on protein fluorescence and lifetime distributions. *J Chem Phys* **101**(6):4578–4584.
196. Alcala JR, Gratton E, Prendergast FG. 1987. Fluorescence lifetime distributions in proteins. *Biophys J* **51**:597–604.
197. James DR, Ware WR. 1985. A fallacy in the interpretation of fluorescence decay parameters. *Chem Phys Lett* **120**(4,5):455–459.
198. Vix A, Lami H. 1995. Protein fluorescence decay: discrete components or distribution of lifetimes? Really no way out of the dilemma? *Biophys J* **68**:1145–1151.
199. Lakowicz JR, Cherek H, Gryczynski I, Joshi N, Johnson ML. 1987. Analysis of fluorescence decay kinetics measured in the frequency-domain using distribution of decay times. *Biophys Chem* **28**: 35–50.
200. Beechem JM, Knutson JR, Ross JBA, Turner BW, Brand L. 1983. Global resolution of heterogeneous decay by phase/modulation fluorometry: mixtures and proteins. *Biochemistry* **22**:6054–6058.
201. Beechem JM, Ameloot M, Brand L. 1985. Global analysis of fluorescence decay surfaces: excited-state reactions. *Chem Phys Lett* **120**(4,5):466–472.
202. Knutson JR, Beechem JM, Brand L. 1983. Simultaneous analysis of multiple fluorescence decay curves: a global approach. *Chem Phys Lett* **102**(6):501–507.
203. Beechem JM. 1989. A second generation global analysis program for the recovery of complex inhomogeneous fluorescence decay kinetics. *Chem Phys Lipids* **50**:237–251.
204. Beechem JM, Gratton E, Ameloot M, Knutson JR, Brand L. 1991. The global analysis of fluorescence intensity and anisotropy decay data: second-generation theory and programs. In *Topics in fluorescence spectroscopy*, Vol. 2: *Principles*, pp. 241–305. Ed JR Lakowicz. Plenum Press, New York.
205. Beechem JM. 1992. Global analysis of biochemical and biophysical data. *Methods Enzymol* **210**:37–55.
206. Chabbert M, Hillen W, Hansen D, Takahashi M, Bousquet J-A. 1992. Structural analysis of the operator binding domain of Tn10-Encoded tet repressor: a time-resolved fluorescence and anisotropy study. *Biochemistry* **31**:1951–1960.
207. Dattelbaum JD, Castellano FN. Unpublished observations.
208. Maus M, Rousseau E, Cotlet M, Schweitzer G, Hofkens J, Van der Auweraer M, De Schryver FC, Krueger A. 2001. New picosecond laser system for easy tunability over the whole ultraviolet/visible/near infrared wavelength range based on flexible harmonic generation and optical parametric oscillation. *Rev Sci Instrum* **72**(1):36–40.
209. Frackowiak D, Zelent B, Malak H, Planner A, Cegielski R, Munger G, Leblanc RM. 1994. Fluorescence of aggregated forms of CHlα in various media. *J Photochem Photobiol A: Chem* **78**:49–55.
210. Werst M, Jia Y, Mets L, Fleming GR. 1992. Energy transfer and trapping in the photosystem I core antenna. *Biophys J* **61**:868–878.
211. Gulotty RJ, Mets L, Alberte RS, Fleming GR. 1986. Picosecond fluorescence studies of excitation dynamics in photosynthetic light-harvesting arrays. In *applications of fluorescence in the biomedical sciences*, pp. 91-104. Ed DL Taylor, AS Waggoner, F Lanni, RF Murphy, RR Birge. Alan R. Liss, New York.
212. Visser AJWG. 1984. Kinetics of stacking interactions in flavin adenine dinucleotide from time-resolved flavin fluorescence. *Photochem Photobiol* **40**(6):703–706.
213. Dudewicz EJ, Van Der Meulen EC. 1981. Entropy-based tests of uniformity. *J Am Stat Assoc* **76**(376):967–974.
214. Livesey AK, Brochon JC. 1987. Analyzing the distribution of decay constants in pulse-fluorimetry using the maximum entropy method. *Biophys J* **52**:693–706.
215. Vincent M, Brochon J-C, Merola F, Jordi W, Gallay J. 1988. Nanosecond dynamics of horse heart apocytochrome *c* in aqueous solution as studied by time-resolved fluorescence of the single tryptophan residue (Trp-59). *Biochemistry* **27**:8752–8761.
216. Merola F, Rigler R, Holmgren A, Brochon J-C. 1989. Picosecond tryptophan fluorescence of thioredoxin: Evidence for discrete species in slow exchange. *Biochemistry* **28**:3383–3398.
217. Sopkova J, Vincent M, Takahashi M, Lewit-Bentley A, Gallay J. 1999. Conformational flexibility of domain III of Annexin V at membrane/water interfaces. *Biochemistry* **38**:5447–5458.
218. Luecke H, Chang BT, Mailliard WS, Schlaepfer DD, Harry H. 1995. Crystal structure of the annexin XII hexamer and implications for bilayer insertion. *Nature* **378**(6556):512–515.
219. Rouvière N, Gallay J. 2000. Wavelength-resolved fluorescence emission of proteins using the synchrontron radiation as pulsed-light source: Cross-correlations between lifetimes, rotational correlation times and tryptophan heterogeneity in FKBP59 immunophilin. *Cell Mol Biol* **46**(5):1113–1131.
220. Becker W. 2005. *Advanced time-correlated single photon counting techniques*. Springer, New York.

PROBLEMS

P4.1. *Calculation of Lifetimes*: Use the data in Figures 4.1 and 4.2 to estimate the lifetime from the time-domain data, and from the phase and modulation.

P4.2. *Fractional Intensity of Components in the Tryptophan Intensity Decay*: At pH 7, tryptophan displays a double-exponential intensity decay. At 320 nm the intensity decay low is $I(t) = 0.19 \exp(-t/0.62 \text{ ns}) + 0.81 \exp(-t/3.33 \text{ ns})$. What is the fractional contribution of the 0.62-ns component to the steady-state intensity at 320 nm?

P4.3. *Stacking Equilibrium in Flavin Adenine Dinucleotide*: Use the intensity decays and lifetimes in Figure 4.61 to calculate the collisional rate between the flavin and adenine groups in FAD.

P4.4. *Average Lifetime*: Suppose that a protein contains two tryptophan residues with identical lifetimes ($\tau_1 = \tau_2 = 5$ ns) and pre-exponential factors ($\alpha_1 = \alpha_2 = 0.5$). Now suppose that a quencher is added such that the first tryptophan is quenched tenfold in both lifetime and steady-state intensity. What is the intensity decay law in the presence of quencher? What is the average lifetime ($\overline{\tau}$) and the lifetime-weighted quantum yield ($<\tau>$)? Explain the relative values.

P4.5. *Decay Associated Spectra*: Tables 4.5 and 4.6 list the results of the multi-exponential analysis of the two-component mixture of anthranilic acid (AA) and 2-aminopurine (2-AP). Use these data to construct the decay associated spectra. Explain the results for the DAS recovered from the non-global (Table 4.5) and global (Table 4.6) analysis.

P4.6. *Data Acquisition Times Using TCSPC With Microsecond Decay Times*: Calculate the time needed to acquire the data in Figure 4.45. Assume the lifetime of $[Ru(bpy)_3]^{2+}$ is 400 ns and that one photon is detected for each excitation pulse. Calculate the data acquisition time to obtain the same data using TCSPC with the same pulse repetition rate and a 1% count rate.

P4.7. *Data Acquisition Times Using TCSPC With Nanosecond Decay Times*: Suppose the lifetime of a fluorophore is 4 ns. Determine the conditions needed for TCSPC. Calculate the time required to count 4 x 10^6 photons with 1 photon counted per 100 excitation pulses. Consider dead times of 2 μs and 120 ns.

P4.8. *Calculation of Fractional Intensities and Pre-Exponential Factors*: Suppose two compounds have equal quantum yields but different lifetimes of $\tau_1 = 1$ μs and $\tau_2 = 1$ ns. If a solution contains an equimolar amount of both fluorophores, what is the fractional intensity of each fluorophore?